CLINICAL GRADE MEDICAL DEVICE TECHNOLOGIES FOR INTERVENTIONAL CARDIOVASCULAR MAGNETIC RESONANCE IMAGING PROCEDURES

by

Dursun Korel YILDIRIM

B.S., in Mechatronics Sciences, Marmara University, 2010

M.S., in Biomedical Engineering, Boğaziçi University, 2016

Submitted to the Institute of Biomedical Engineering
in partial fulfillment of the requirements
for the degree of
Doctor
of
Philosophy

Boğaziçi University

2021

ACKNOWLEDGMENTS

First and foremost, I would like to express my deep and sincere gratitude to Assoc. Prof. Dr. Özgür Kocatürk for his patience, motivation, enthusiasm and immense knowledge. His guidance and persistent help have been the brightest beacon on this toilsome road. His hard work and determination have always inspired me to discover my better self. I would also like to thank him for his friendship, empathy and great sense of humor.

I would like to thank my thesis committee members Prof. Dr. Cengizhan Öztürk, Assoc. Prof. Dr. Esin Öztürk Işık, Asst. Prof. Dr. Özlem İpek and Asst. Prof. Dr. Daniel A. Herzka for their insightful guidance and precious comments.

I also would like to thank Dr. Robert J. Lederman, Senior Investigator of Cardiovascular Intervention Program, (NHLBI, National Institutes of Health), and his team for sharing their facilities and for their invaluable contributions to the key issues during this thesis study.

My appreciation also extends to Gary Melvin and Dr. Dumitru Mazilu for their unparalleled mechanical expertise and assistance to tackle compelling design problems.

It is a privilege to have understanding and helpful people around, in troublesome times. I express my special thanks to Hale Gökçe Hatay for tirelessly answering my questions about the institutional procedures, every time, and being the trailblazer for all of us in the academic progress. I also have to mention how grateful I am for Doğangün Uzun for carrying the work load of ongoing projects during writing of this thesis. I owe a sincere thankfulness to my dearest friend Galip Doğan for always being only one phone call away, despite the time difference and helping me to see the brighter side of things.

Finally, I owe my greatest gratitude to my dear parents Şefika and Ali Yıldırım, and my biggest luck, my dear wife Rana Shenawi, whom this thesis is dedicated to, for their unconditional love, caring and support which made all these possible and always make the life easier.

ACADEMIC ETHICS AND INTEGRITY STATEMENT

I, Dursun Korel Yıldırım, hereby certify that I am aware of the Academic Ethics and Integrity Policy issued by the Council of Higher Education (YÖK) and I fully acknowledge all the consequences due to its violation by plagiarism or any other way.

Name :

Signature:

Date:

ABSTRACT

CLINICAL GRADE MEDICAL DEVICE TECHNOLOGIES FOR INTERVENTIONAL CARDIOVASCULAR MAGNETIC RESONANCE IMAGING PROCEDURES

Magnetic Resonance Imaging (MRI) is a promising candidate against X-ray fluoroscopy for the image-guidance of minimally invasive procedures thanks to its ionizing radiation-free, exquisite soft tissue contrast and ability of 3D real-time imaging in arbitrary planes. However, interventional MRI (iMRI) is hampered by the lack of clinical grade MRI-compatible interventional devices. In this thesis study, first, a low-profile iMRI device fabrication method was introduced by modifying the conductive ink printing method which was previously introduced by our group. Next, three most fundamental iMRI device designs including a 20 G active iMRI needle, a 0.035" outer diameter metallic active iMRI guidewire and a 6 FR, MRI-safe, metallic braided catheter were successfully introduced to expand interventional cardiovascular MRI applications. Electromagnetic simulation tools were employed to optimize the device radio frequency (RF) antenna geometry for optimal device visibility, and to assess RF-safety of iMRI devices. Proposed iMRI device designs were prototyped using biocompatible materials. In-vitro mechanical, RF-induced heating and MRI visibility performance of the prototypes were tested per international medical device test standards. In-vivo mechanical and MRI visibility tests were performed in swine per local animal study regulations. Test results were compared to commercially available equivalents. RF-induced temperature rise of all three prototypes remained within clinically acceptable limits. Active iMRI needle and active iMRI guidewire prototypes were clearly visible during in-vitro and in-vivo tests. All prototypes demonstrated comparable mechanical performance with commercially available equivalents. Proposed iMRI device designs will meet the most urgent need in the iMRI field enabling a broad range of iMRI applications.

Keywords: interventional MRI, active device design, active iMRI needle, active iMRI guidewire, CMR-safe metal braided catheter.

ÖZET

GİRİŞİMSEL KALP-DAMAR MANYETİK REZONANS GÖRÜNTÜLEME UYGULAMALARI İÇİN KLİNİK KULLANIMA UYGUN TIBBİ CİHAZ TEKNOLOJİLERİ

İyonlaşan radyasyondan bağımsız üstün yumuşak doku tezatı ve herhangi bir düzlemde 3 boyutlu gerçek zamanlı görüntüleme yeteneği ile Manyetik Rezonans Görüntüleme (MRG) girişimsel tıp için, X-Ray floroskopi karşısında güçlü bir aday haline gelmektedir. Fakat, klinik seviyede kullanılabilir cihazların azlığı nedeniyle girişimsel MRG (gMRG) uygulamaları sınırlı kalmıştır. Bu tez çalışması kapsamında ilk olarak, daha önce bizim tarafımızdan geliştirilen iletken mürekkep yazdırma yöntemi iyileştirilerek yeni bir, düşük profilli gMRG cihaz üretim yöntemi ortaya konmuştur. Sonrasında, bir adet 20G aktif gMRG iğnesi, bir adet 0.035" çaplı, metal aktif gMRG kılavuz teli ve bir adet, 6Fr, MRG açısından güvenli metal örgülü kateter tasarımı başarılı bir şekilde geliştirilmiştir. gMRG cihazlarının MRG görünürlüklerini iyileştirmek ve RF güvenliklerini değerlendirmek amacı ile elektromanyetik simülasyon araçları kullanılmıştır. Geliştirilen cihaz tasarımları, biyouyumlu malzemeler kullanılarak üreilmiştir. Üretilen örnekler mekanik, RF güvenliği ve MRG görünürlüğü açısından uluslararası tıbbi cihaz sınama standartlarına uygun olarak labaratuvar ortamında sınanmıştır. Daha sonra, mekanik özelliklerin ve MRG görünürlüğünün sınanması, etik kurallara uygun olarak canlı hayvan deneyleri ile gerçekleştirilmiştir. Sınama sonuçları ticari olarak elde edilebilen eşdeğer cihazlar ile karşılaştırılmıştır. Tüm cihaz örneklerinin RF kaynaklı sıcaklık artışı klinik olarak kabul edilebilir sınırlar içerisinde kalmıştır. Aktif gMRG iğnesi ve aktif gMRG kılavuz teli tüm deneyler sırasında MRG ile açık bir şekilde görüntülenebilmiştir. Tüm cihaz örneklerinin mekanik performansı ticari olarak elde edilebilen eşdeğer cihazlar ile kıyaslanabilir seviyededir. Geliştirilen cihaz tasarımları, alandaki en temel ihtiyacı karşılayarak çeşitli gMRG uygulamalarına imkan verecektir.

Anahtar Sözcükler: Girişimsel MRG, aktif cihaz tasarımı, aktif gMRG iğne, aktif gMRG kılavuz tel, MRG altında güvenli metal örgülü kateter

TABLE OF CONTENTS

ACKNOWLEDGMENTS iii
ACADEMIC ETHICS AND INTEGRITY STATEMENT iv
ABSTRACT v
ÖZET vi
LIST OF FIGURES x
LIST OF TABLES xxi
LIST OF SYMBOLS xxii
LIST OF ABBREVIATIONS xxv
1. INTRODUCTION 1
2. BACKGROUND 3
2.1 Image-guided cardiovascular interventions 4
2.2 Magnetic Resonance Imaging 5
2.3 Interventional Cardiovascular MRI (iCMR) 7
2.4 Interventional MRI Devices 8
2.4.1 Passive devices 9
2.4.2 Semi-active (inductively coupled) devices 11
2.4.3 Active devices 12
2.5 iMRI device development 15
2.6 MRI Safety 16
2.6.1 RF safety test methods for active iMRI devices 20
2.7 Electromagnetic computation and modelling in MRI 26
2.8 Specific aims 28
2.9 Thesis Outline 31
3. A 20 GAUGE ACTIVE NEEDLE DESIGN WITH THIN-FILM PRINTED CIRCUITRY FOR INTERVENTIONAL MRI AT 0.55T 32
3.1 Introduction 32
3.2 Methods 34
3.2.1 Conductive ink printing system design and characterization tests 34
3.2.2 MRI compatible active needle design and characterization tests 38

3.2.2.1 Electromagnetic field simulations 38
3.2.2.2 MRI Compatible Active Needle Design 40
3.2.2.3 In-vitro characterization tests 43
3.2.2.4 In-vivo characterization tests 46
3.3 Results 47
3.3.1 Conductive ink printing system characterization tests 47
3.3.2 Electromagnetic field simulations 48
3.3.3 MRI compatible active needle characterization tests 50
3.4 Discussion 56
3.5 Conclusion 60
4. A NOVEL ACTIVE GUIDEWIRE DESIGN WITH A CURVED TIP GEOMETRY FOR INTERVENTIONAL MRI APPLICATIONS UNDER 0.55T . . 61
4.1 Introduction 61
4.2 Methods 64
4.2.1 Electromagnetic field simulations 64
4.2.2 Active iMRI guidewire design 66
4.2.3 In-vitro characterization tests 68
4.2.4 In-vivo characterization tests 71
4.3 Results 72
4.3.1 Electromagnetic field simulations 72
4.3.2 In-vitro characterization tests 72
4.3.3 In-vivo characterization tests 78
4.4 Discussion 79
4.5 Conclusion 83
5. A CARDIOVASCULAR MAGNETIC RESONANCE (CMR) SAFE METAL BRAIDED CATHETER DESIGN FOR INTERVENTIONAL CMR AT 1.5 T. 84
5.1 Introduction 84
5.2 Methods 85
5.2.1 Electromagnetic field simulations 85
5.2.2 Prototype construction 89
5.2.3 In-vitro characterization tests 92
5.3 Results 95

5.3.1 Electromagnetic field simulations 95
5.3.2 In-vitro characterization tests 95
5.3.3 In-vivo characterization tests 103
5.4 Discussion 103
5.5 Conclusion 105
6. GENERAL CONCLUSION AND FUTURE WORK 107
7. APPENDIX A: Publications 111
8. APPENDIX B: Scientific awards and invited talks 115
REFERENCES 116

LIST OF FIGURES

Figure 2.1 In-vivo imaging of passive markers. (A) Passive non-braided balloon catheter filled with CO_2 in a right atrium [65]. (B) Nitinol guidewire (Glidewire 260 cm/0.035", Terumo, Japan) with a high-UTS stainless-steel marker affixed at its tip during left heart catheterization at 1.5 T. (C) 4% Gd-DTPA coated 4 Fr catheter in a canine aorta [63]. White arrows point to the passive marker locations. 10

Figure 2.2 Working principle of semi-active markers. Coupling between a surface coil and a catheter-mounted semi-active marker coil is described [66]. 11

Figure 2.3 (A) In-vitro image of a thin-film coated semi-active marker at the tip of a 5 Fr catheter subassembly 45° orthogonal to transverse plane. (B) In-vivo image of a semi-active marker consisting of a resonant solenoid stent [66]. 12

Figure 2.4 (A) In-vivo MRI of an active guiding catheter with a loopless antenna and three solenoid markers in the aorta [83]. (B) In-vivo MRI of a two-channel active guidewire consists of a loopless antenna for the shaft visibility and a solenoid coil at the tip, in brachiocephalic artery. White arrow indicates the active guidewire tip [69]. 14

Figure 2.5 Example Images of Electric Field and SAR Distributions in a Phantom at 1.5T (left) and 3T (right). Electric field distributions are shown in the XZ plane (top), while SAR distributions are shown in the XZ plane (middle) and in the XY plane (bottom), respectively. The dashed lines show the axial location where the XY cross-sectional planes are acquired [125]. 21

Figure 2.6 Example diagram of apparatus for testing of RF heating near an implant during MR imaging. Three temperature probes are placed on the test subject and another probe is placed on the reference rod [125]. 22

Figure 2.7 Application of a tangential E-field (E_{tan}) over a small length ($\Delta\tau$) at a location along the test subject results in a scattered E-field (E_s). τ is the distance of the field excitation point from the end of the test subject and P is the position vector where the scattered field is evaluated [102]. 23

Figure 2.8 (A) Local SAR distribution in a virtual human body at 1.5T based on electromagnetic simulation results [132]. (B) A virtual human body within the RF transmit volume coil in the electromagnetic simulation environment and arbitrary iMRI device trajectories where the tangential E-fields are extracted [130]. Blue sections indicate the device portion inserted into the body. Red sections indicate the device portion remains outside the body. 25

Figure 3.1 Closed-loop Proportional-Integral-Derivative (PID) control diagram of the ink dispenser unit where R(t) is the target pressure value (reference), e(t) is the calculated error between the reference value and the actual pressure, Kp is the proportional coefficient, Ki is the integral coefficient, Kd is the derivative coefficient, L(t) is the linear position of the actuator, M(t) is the linear to angular position conversion, S(t) is the step calculation and the p(t) is the actual pressure value from the sensor and q(t) is the calculated material flow. 35

Figure 3.2 Electronic schematic of the closed-loop PID control circuit consisting of a disposable inline blood pressure sensor, a low-noise amplifier and a microcontroller. 36

Figure 3.3 CNC-based four axis conductive ink printing system with a rotary axis for non-planar fabrication. The 3D printed automated conductive ink dispenser with the disposable inline pressure sensor is mounted on the Z axis. 37

Figure 3.4 (A) Simplified schematic representation of the active needle RF antenna and corresponding printed polymer layers (parasitic capacitance of the solenoid coils and the transmission line is ignored). (B) 3D drawing of the active needle prototype used for the electro-magnetic simulations, showing the individual component dimensions. Polymer layers are retracted on the drawing to expose the normally encapsulated components. (L1 is the OD of the nitinol hypotube. L2 is the OD after the first layer polyester tube only, L3 is the OD after conductive ink printing on the first layer polyester tube. L4 is the OD after the second layer polyester tube only, L5 is the OD after conductive in printing on the second layer polyester tube. L6 is the final OD of the active needle.). 39

Figure 3.5 Discretized 3D model of the active needle prototype using 5 µm voxel size. 40

Figure 3.6 (A) The first layer conductive ink printed polyester tube consisting only a straight line and (B) the second layer conductive ink printed polyester tube with solenoid coils of the RF antenna connected with straight lines. (C) Optical microscope measurements of the printed solenoid coils (L1 is the needle diameter after the second polyester layer, L2 is the printed conductor width, L3 is the distance between the adjacent windings, L4 is the needle diameter after the second printed layer and L5 is the solenoid coil length). Final profile measurements of the active needle prototypes (D) with the printed RF antenna and (E) with the insulated copper wire wound RF antenna. L1 is the final needle OD and L2 is the solenoid coil length. (F) The final assembly of the active needle prototype with the custom Luer-lock hub, micro coaxial cable and the tune and match circuit. (G) Tune and match circuit diagram of the RF antennas. (A)-(D) belong to the active needle prototype with the conductive ink printed antenna. (E) belongs to the active needle prototype with the 44 AWG insulated copper wire antenna. 42

Figure 3.7 Mechanical test setup for (A) the bending and (B) puncture tests. Same setup was used for both tests with small modifications. 44

Figure 3.8 Custom, 3D printed sliding and rotating needle holder used for in-vitro real-time MRI tests. (A) 45° rotated and (B) vertically fixed. Active needle prototype is mounted on the needle holder and slid and/or rotated in the field of view. 47

Figure 3.9 (A) PID controller response to the reference inputs including a step profile, a fast changing profile and a programmable profile with the corresponding controller error margins showing the ink dispenser unit control accuracy test. (B) Circumferential straight lines printed on a 5Fr Pebax hypotube with 1mm, 3mm, 5mm and 10mm separations for the mechanical accuracy test of the electromechanical system. (C) Fine printed lines with 100 µm and 300 µm line width. Line width can be changed on-the-fly. PID control eliminates residual ink globs at the needle tip. 48

Figure 3.10 Electro-magnetic simulation results of the active needle design. (A) B_1^+ distribution of the desired antenna geometry with 10 turns solenoid coils. (B) The B_1^+ magnitude alongside the active needle design showing the effects of the solenoid coil length, conductor thickness, normalized pitch (the ratio of the distance between the adjacent turns divided by the conductor diameter) and needle orientation with respect to B_0. B_1^+ profiles were extracted on the green line parallel to active needle models. 49

Figure 3.11 Magnetic field (B) vectors around the windings of 2 mm, 2.5 mm, 3 mm and 4 mm long, 10 turns solenoid coils with 1.5, 0.67 and 0.25 normalized pitch as the needle is oriented perpendicular to B_0. Rotated vectors from the longitudinal axis around the windings indicate the presence of transverse magnetic field (B_{Tr}) which is perpendicular to solenoid axis. 2.5 mm long solenoid coil with 0.67 normalized pitch shows sufficient marker visibility and minimizes the B_{Tr} coupling. 50

Figure 3.12 Test results of (A) the bending and (B) puncture tests. Each test was repeated three times per needle and the average of the results are plotted. The red dashed line on the graphs indicate the beginning of the retraction phase for each test. 51

Figure 3.13 In-vitro MR images of the active needle prototypes at 0.55T using a real-time bSSFP imaging sequence. Straight conductors, connecting solenoid coils in series, couple better with the transverse magnetic field when the needle is parallel to B_0 providing a bright signal between the solenoid markers. This coupling decreases when the needle is perpendicular to B_0 providing a more distinct marker signal. 52

Figure 3.14 In-vitro SNR maps of the active needle prototypes on sagittal and axial planes. Pixel intensity so that the SNR profiles are calculated on a straight line 1 mm away from and parallel to the active needle prototypes (the white dashed line). The major peaks at the pixel intensity profiles represent the solenoid coil locations. 52

Figure 3.15 In-vitro real-time MRI of active needle prototypes during insertion, rotation with respect to B_0 and exaggerated bending in sagittal plane. 53

Figure 3.16 RF-induced heating test results of the active needle prototypes parallel and perpendicular to B_0 for 90 seconds and 15 minutes, and the RF-induced heating measurement of a bare nitinol needle body parallel to B_0 for 90 seconds. The dash line indicates the start of the MRI scan and the solid line indicates the stop of the MRI scan. The RF-induced heating rise of the active needle prototype with the insulated copper wire antenna exceeds clinically acceptable limits ($>2^{\circ}C$) in every condition. 54

Figure 3.17 In-vivo real-time MRI of the active needle prototypes. The active needle signal is colorized after windowing with window width/window level = 16/16. The printed RF-antenna provides a more refined marker signal obscuring less anatomical information compared to the insulated copper wire RF-antenna. 55

Figure 4.1 (A) The component list and schematic representation of the AGW prototype. (B) Final assembly of the AGW prototype and the detachable handle. (C) Subassembly of the detachable handle showing the modified torquer device and the tune and match and leakage current blockage circuit. (D) Electrical diagram of the tune and match and the leakage current blockage circuit. 67

Figure 4.2 Mechanical test setups for (A) the stiffness, (B) torque transmission and (C) trackability tests of the AGW prototype. The AGW prototype is fixed on the custom apparatus forming an arch for the stiffness test. A paper indicator was attached to the proximal end of the AGW prototype for the torque transmission test and the tip cure itself was used as the distal end indicator. The AGW prototype was manipulated by the rubber coated actuators of the dedicated trackability test setup. 71

Figure 4.3 Electromagnetic simulation results of the AGW prototypes. B_1^+ field distribution shows that signal sensitivity towards the tip of the monopole antenna-based AGW can be recovered using a tip coil and configured adjusting the coil specifications. B-field vectors and the E-field distribution within and around the tip coil show the standing wave formation along the monopole antenna and its effects on the generated B-field direction so that the MRI artifact signature. 73

Figure 4.4 RF-induced heating results of the AGW prototype alone and in tandem with a MRI compatible metal braided catheter (Infiniti, Cordis, FL). Maximum temperature rise is observed when the tip of the metal braided catheter is aligned with the junction of the AGW prototype. Green dashed line indicates the start of the MRI scan. Red dotted line indicates the end of the MRI scan. 74

Figure 4.5 In-vitro MR images of the AGW prototypes. Artifact signature of the straight guidewire prototypes match with the electromagnetic simulation results. Use of a relatively loose pitch tip coil (MP35N coil wire) results in a distinct tip signal which causes the loss of the curve information for the curved tip geometry. The tight pitch tip coil (35N LT coil wire) provides a full shaft and continuous curve visibility which also gives information about the wire rotation. 75

Figure 4.6 In-vitro MRI of the AGW prototype in tandem with commercially available clinical catheters. Circular dark artifacts on images are signal voids caused by mounting pegs and/or air filled balloons of the catheters. Since the tested catheters have curved geometries, it is not always possible to align the whole AGW prototype parallel to one plane which explains the SNR fluctuations along the AGW prototype. 76

Figure 4.7 In-vitro MR images of the AGW prototype alone in a 3D-printed heart model and in tandem with a Supertorque, Cordis catheter. White arrows indicate the actual tip curvature. As the AGW tip pushes against the model wall the tip curve is pushed out of imaging plane resulting a signal loss. Curve signal recovers as the AGW tip is free in the model. The dark susceptibility artifact on the top right image is caused by the metallic braiding of the pigtail catheter. AGW prototype can straighten out the pigtail catheter without any alteration on the device signal. 77

Figure 4.8 Figure 4.8. Mechanical test results of the AGW prototype compared to commercially available equivalents. All results show that the AGW prototype has clinically acceptable mechanical performance comparable to the commercially available equivalents. 78

Figure 4.9 Figure 4.9. In tandem stiffness test result. AGW prototype has a comparable stiffness with the commercially available guidewire and can completely straighten out a metal braided pigtail catheter. 78

Figure 4.10 In-vivo MR images of the AGW prototype (A) alone, rotated parallel to the imaging plane in the aortic arch and (B) in tandem with the balloon catheter, rotated perpendicular to the imaging plane in inferior vena cava. The black dot on the image represents the air filled balloon. The full shaft and continuous shaft visibility provides exact tip location and rotation information in both cases. 79

Figure 5.1 3D model of the (A) non-segmented and (B) segmented full load braiding pattern (two over, two under). Braiding wires are colored for the ease of visual tracking. Same color wire pairs are laser-cut in-situ at each segmentation step. 86

Figure 5.2 Embedded braiding layer between two Pebax layers after reflowing process. 90

Figure 5.3 Schematic of a full-cycle braiding segmentation pattern. Breaks on the braid pattern can be seen by following the red and yellow lines. The pattern is shown in 2D, representing the unwrapped form of the catheter shaft. 91

Figure 5.4 (A) Test sample position in the ASTM 2182 gel phantom, (B) in the ASTM 2119 copper sulfate phantom and (C) phantom and sample positions in the scanner. 93

Figure 5.5 (A and B) Flexibility, (C) push-ability and (D) and (E) torque response test setups. 94

Figure 5.6 (A) 21 cm long dissected segmented braided catheter subassembly part and (B) detached and scraped braiding wires. 95

Figure 5.7 Electromagnetic simulation results of the non-segmented and segmented braiding models. E-field concentration at braiding ends is mitigated by electrically interrupting long conductive wires. Maximum E-field concentration occurs at the ends of individual short segments. 96

Figure 5.8 (A) Braiding uniformity and the node to node distance were confirmed under light microscope. (B) The segmented braid catheter constructed in-house. The segmentation points on the braiding layer are shown with white arrows (Blue insulation is discolored (red arrow) but not interrupted by the laser in-situ segmentation process). 97

Figure 5.9 RF induced temperature rise of the segmented catheter subassembly after (A) 60 seconds bSSFP, (C) 60 seconds GRE, (E) 20 minutes bSSFP and (G) 20 minutes GRE scans. RF induced temperature rise of the non-segmented catheter subassembly after (B) 60 seconds bSSFP, (D) 60 seconds GRE, (F) 20 minutes bSSFP and (H) 20 minutes GRE scans. 98

Figure 5.10 In-vitro MR images and susceptibility artifact measurements. Segmentation of metallic braiding wires mitigates the E-field amplification so that the local flip angle amplification using Spin Echo pulse sequences. However, segmentation does not alter the material properties so that the signal void artifact does not change after segmentation. 99

Figure 5.11 Torque transmission test results of (A) segmented, (B) non-segmented braid and (C) commercial catheters. 100

Figure 5.12 Bending stiffness test result of (A) segmented, (B) non-segmented braided and (C) commercial catheters and (D) the test results averages. 101

Figure 5.13 Push-ability test results of (A) the segmented catheter sample, (B) the non-segmented catheter sample and (C) the commercial catheter. (D) Comparison of all catheter samples (averaging test results). 102

Figure 5.14 (A) Bending stiffness, (B) push-ability and (C) torque response test results of the segmented catheter after the deteriorating mechanical test. 102

Figure 5.15 In-vivo MR images. Segmented braided and non-segmented braided catheter subassemblies were advanced through the superior vena cava with a custom, iron-oxide coated guidewire in tandem during real-time bSSFP CMR (Red arrows indicate the tip of the custom, iron-oxide coated guidewire prototype, white arrows indicate the segmented and non-segmented catheter subassemblies). 103

LIST OF TABLES

Table 4.1	Commercially available catheters with which the active guidewire prototype was tested in tandem.	70
Table 5.1	RF-induced temperature rise at the distal tip.	97
Table 5.2	Torque requirement for a 360-degree rotation.	100

LIST OF SYMBOLS

T	Tesla
B	Magnetic field
B_0	Main magnetic field
B_1	Radio frequency magnetic field
B_1^+	Forward polarization radio frequency magnetic field
B_1^-	Reverse polarization radio frequency magnetic field
B_{TR}	Transverse magnetic field
E	Electric field
E_{Tan}	Tangential electric field
E_S	Scattered electric field
P	Position vector where the scattered field is evaluated
E_{1r}	Radial component of the scattered E-field
τ	Distance of the field excitation point from the end of the test subject
$\Delta\tau$	Geometric difference between two excitation points
S_1	Transfer function
R	Target pressure value
e	Calculated error between the reference value and the actual pressure
k_p	Proportional coefficient
k_i	Integral coefficient
k_d	Derivative coefficient
L	Linear position of the actuator
M	linear to angular position conversion
S	Step calculation
$p(t)$	Actual pressure value from the sensor
q	Calculated material flow
L	Length

μ	Viscosity
μm	Micrometer
m	Meter
s	Second
ms	Milli second
FR	French
$^{\circ}$	Degree
℃	Degree Celsius
G	Gauge
Hz	Hertz
MHz	Mega Hertz
GHz	Giga Hertz
mL	Milli Liter
TE	Echo time
TR	Repetition time
T_1	Longitudinal relaxation time
T_2	Transverse relaxation time
T_2^*	Effective transverse relaxation time
^{19}F	Fluorine 19 isotope
^{13}C	Carbon 13 isotope
W	Watt
g	Gram
kg	Kilo gram
ΔT	Temperature change
Δt	Time difference
J	Joule
c	Specific heat capacity
S	Siemens
σ	Electrical conductivity
ρ	Mass density
Ω	Ohm

λ	Electrical wavelength
Q	Coil quality factor
$R_{Antenna}$	Antenna resistance
R_{Cable}	Cable resistance
A	Ampere
p	Length of the crossover region in the crimp path
p'	Length of the undulation region in the crimp path
a	Minor diameter of the yarn cross-section
k_1	Coefficient between p and p'
r_0	Radius of the braid
$r(\theta)$	Crimp of braiding wire as a sine wave
β	Shift angle between the braiding wires
α	braiding angle with the horizontal axes
n	Number of the braiding yarns
i	Counter defining the actual braiding yarn
θ	Wrapping angle
LL	Linear length
LD	Distance on horizontal axis after a 360-degree rotation
PC	Perimeter of the catheter tube
NN	Node-to-node horizental distance

LIST OF ABBREVIATIONS

CO_2	Carbon Dioxide
Gd	Gadolinium
DTPA	Diethylenetriamine pentaacetate
PID	Proportional-integral-derivative
CNC	Computer numeric control
2D	Two dimension
3D	Three dimension
RF	Radio frequency
mm	Millimeter
cm	Centimeter
bSSFP	Balanced steady state free precession
GRE	Gradient recalled echo
TrueFISP	True fast imaging steady-state precession
FIESTA	Fast imaging employing steady-state acquisition
MR	Magnetic resonance
MRI	Magnetic resonance imaging
iMRI	Interventional magnetic resonance imaging
CMR	Cardiac magnetic resonance
iCMR	Interventioanl cardiac magnetic resonance
US	Ultrasound
TEE	Transesophageal cchocardiography
AGW	Active guidewire
ASTM	American Society for testing and standards
ISO	International organization for standardization
FDA	Food and drug administration
TS	Technical specification
MEMS	Micro electro-mechanical systems
DNA	Deoxyribonucleic acid

LAA	Left Atrium Appendage
SNR	Signal-to-noise ratio
CNR	Contrast-to-noise ratio
SAR	Specific absorption rate
fps	Frames per second
LCE	Late gadolinium enhancement
EM	Electromagnetic
CFD	Computational fluid dynamics
CBM	Computational biomechanics
FEM	Finite elements method
FDTD	Finite difference time domain
SIE	Surface integral equation
VIE	Volume integral equation
RAM	Random access memory
CPU	Central processor unit
GPU	Graphical processor unit
AWG	American wire gauge
FoV	Field of view
FA	Flip angle
Px	Pixel
ST	Slice thickness
ID	Inner diameter
OD	Outer diameter
VNA	Vector network analyzer
DICOM	Digital imaging and communications in medicine
PIN	Positive-intrinsic-negative
dB	Decibel

1. INTRODUCTION

Minimally-invasive cardiovascular procedures are targeting increasingly complex pathologies as attractive alternatives to surgical methods thanks to the reduced operational risks and morbidity rates. However, such procedures are mainly limited by the X-ray guidance, specifically in treatments for structural heart diseases, electrophysiologic disorders, and inaccessible or occluded vasculature due to the poor soft tissue contrast afforded by X-Ray fluoroscopy. Ionizing radiation employed by X-Ray fluoroscopy, on the other hand, brings serious safety concerns including increased long term cancer development risk and occupational injuries.

With the developing technology, real-time Magnetic Resonance Imaging (MRI) has become a strong candidate to replace the X-Ray fluoroscopy for image-guided interventions with its superior soft tissue contrast, ionizing radiation free mechanism, intra-operational tissue characterization capabilities and temporal resolutions comparable to alternative imaging modalities. However, despite the advancements in MRI, interventional MRI (iMRI) field still lacks clinical grade safe and conspicuous devices. Materials used for iMRI device fabrication are limited due to strong static magnetic fields and the RF energy deposition employed by MRI systems. Non-metallic iMRI device designs suffer from the inferior mechanical performance. Commercially available electronic components, on the other hand are rigid and bulky, and utilization of such components risks bystander tissue injury. Various micro electromechanical systems (MEMS) based methods have been introduced to enable low-profile iMRI device fabrication. Introduced methods are generally modified planar fabrication engineering approaches and have limitations for multilayer non-planar device fabrication. As a result, devices developed using these methods either remained a proof of concept or could not be translated to the clinic after animal experiments because of the insufficient conspicuity, inadequate mechanical performance or clinically unacceptable RF heating risks.

It has been almost two decades since the first clinical interventional cardiovascular MRI (iCMR) catheterization was performed using MRI-conditional devices. The number of clinical centers performing diagnostic iCMR has increased in the last five years and it is anticipated to increase more in the next five years. Hence, the need for dedicated, safe and conspicuous iMRI devices with clinically acceptable mechanical characteristics to bring iCMR towards the clinical realm is still valid [1–4].

2. BACKGROUND

Imaging of human body and internal organs with accurate and non-invasive methods has a great importance for medical diagnosis, treatment and follow-up. Incremental developments in cardiovascular imaging have significantly improved care for patients with heart disease [2]. Despite non-invasive imaging has dramatically reduced the need for cardiac catheterization for most diagnostic procedures, diagnostic cardiac catheterization is still performed routinely for anatomical and physiological assessment and planning subsequent interventions [4].

Minimally invasive therapies aim to reduce the morbidity and mortality risks related to surgical access and exposure, yet provide comparable results to surgical interventions. In the past, complex conditions including aortic aneurysm, valvular disease and other congenital and structural cardiac abnormalities were treated via surgical procedures [5, 6]. Catheterization method refers to insertion of a small diameter catheter device into the cardiovascular system and steering it into various blood vessels and cardiac chambers with the assistance of an imaging system for diagnostic or therapeutic purposes. Institutional cardiovascular catheterization started in the mid-1960s with percutaneous transluminal coronary angioplasty as the only application. However, over the years, interventional cardiology has targeted increasingly more complex conditions including congenital and structural heart disease, and pediatric applications. Lately, interventional approaches including transcatheter aortic valve repair and replacement, electrophysiology procedures, septal defect closure, appendage closure, and many others have been preferred against surgical procedures due to reduced operation time, patient discomfort, hospitalization time and long term morbidity and mortality rates [7]. Consequently, interventional cardiovascular applications have become the first option for most therapeutic cardiovascular procedures formerly required surgical interventions and are determined to put surgical tools in glass containers to be exhibited in medical museums [8].

Catheterization method requires image guidance which shows the position of the interventional tools (i.e. guidewires and catheters) relative to the background anatomy during procedure. Currently, X-Ray fluoroscopy, computed tomography (CT), ultrasound, electroanatomic mapping and MRI are the main imaging modalities for the image-guidance of minimally invasive interventions. Each interventional imaging modality has its own advantages and disadvantages in terms of dedicated device design, visualization of both device and anatomy at the same time and potential side effects.

2.1 Image-guided cardiovascular interventions

Image guidance for cardiovascular procedures began with the use of X-Ray to acquire anatomical and physiological data for the confirmation and guidance of diagnostic cardiac catheterization [9]. Ever since, X-Ray fluoroscopy has been the flagship modality for the guidance of minimally invasive procedures. Since, this modality works on the principle of imaging attenuated X-Ray emissions, it suffers from poor soft tissue contrast. X-Ray imaging technology provides superimposed images of the anatomy as projections which cannot provide accurate 3D anatomical data, so delineation of target tissues including leaflets, myocardium and vessels is not enough to carry out safe procedures without additional assistance [1]. Hence, even though it visualizes the interventional devices completely within the body, it requires additional assumptions based on anatomical landmarks, operator's experience and use of nephrotoxic contrast agents to determine the exact device location [10, 11]. Furthermore, as the most important concern, X-Ray exposure to both patients and operators consists of ionizing radiation which has enough energy to potentially cause DNA damage and may increase a person's lifetime risk of cancer development [12]. This risk improves with the repeat procedures and/or follow up exams. On the other hand, occupational X-Ray exposure risks malignancy and cataract for medical staff. Using X-ray protective lead aprons increases the operator discomfort and staff musculoskeletal injury risk [13].

Ultrasound, Transesophageal Echocardiography (TEE), electro-anatomical mapping and catheter navigation systems are used as additional supporting modalities to

overcome the drawbacks of fluoroscopy and to decrease the ionizing radiation exposure [14, 15]. TEE is the most sensitive and specific technique to detect Left Atrium Appendage (LAA) thrombus which is a contraindication to atrial catheterization. [16] Despite the high temporal resolution, TEE generally underestimates chamber volumes by 15 to 30 mL because of the reduced image quality. Moreover, TEE has an interobserver variability twice as high than CT and MRI [14, 15]. Also, TEE carries procedural risks including bleeding and perforation which can extend the length of hospital stays [16]. The advent of catheter navigation and electro-anatomical mapping systems has improved the catheterization and ablation efficacy [17–20]. These systems rely on pre-acquired 3D anatomical images using CT or MRI. However, the cardiac chamber morphology may change due to the variations in the heart rate and rhythm or catheter manipulations. So, the registered 3D images may not correspond to the actual anatomy during the catheterization procedure. As a result, registration errors may cause misleading of the procedure [21]. Additionally, there still is a conflict in the literature for the definition of the electrical activity of acute and chronic ablation injury, which limits the reliability of electro-anatomical mapping systems [22].

2.2 Magnetic Resonance Imaging

Magnetic resonance imaging works on a completely different physical principal compared to X-Ray fluoroscopy and ultrasound. Instead of using ionizing radiation or reflected high frequency sound waves, MRI exploits proton precessions of hydrogen atoms within the body to generate anatomical images. For this purpose, a high strength static magnetic field (B_0), generally produced by a superconducting electromagnet in the orders of 1.5 Tesla (T) (1T=10000 Gauss), is employed to generate a net magnetic moment and to align proton spins parallel to the longitudinal axis of the magnet. Permanent magnets are utilized to generate lower field strengths (<0.5T). Aligned protons precess at a specific frequency which is known as "Larmor Frequency" (63.66 MHz at 1.5T) regarding the static magnetic field strength. Those proton spins act as dipoles in the static magnetic field and can be excited with radiofrequency (RF) power depositions at the Larmor frequency. RF transmit coils are used to generate a RF

magnetic field (B_1) perpendicular to B_0 and to excite the precessing protons. Excited proton spins tend to tip towards the transverse plane and keep spinning. At this point, spinning dipoles can induce alternating currents on conductors due to Lenz law. Same RF antennas used for generating B_1 or additional RF receive antennas can be used to pick up the MRI signal. Due to the inhomogeneities of B_0 and spin-spin interactions, precessing protons start to loose phase coherence which leads to the reduction of the net magnetization. This is referred as free induction decay (FID) and the loss of signal is typically described by T_2 or T_2^* decay time constants. Also, the proton precessions start to recover to their initial position, which is parallel to B_0, as soon as the RF excitation stops. This process is known as relaxation and measured by T_1 time constant or recovery longitudinal magnetization. However, one drawback of the whole process is that all proton spins exposed to the RF excitation within B_0 exhibit the same behavior and a spatial encoding becomes a necessity. For this purpose controlled alterations are induced on B_0, with gradient coils, along the in-plane and slice selection orientations. B_0 is altered linearly in the longitudinal direction of the magnet (Z axis) to specifically select the excitation slice. Slice selection is generally performed during RF excitation. In-plane localization is provided by frequency and phase encoding in transverse plane. Following the RF excitation, another magnetic field gradient is applied to force some protons to spin faster. When the gradient is turned off, all protons again precess at the same frequency but with larger shifts in phase coherence. Spin phase vary linearly in the phase-encoding direction. Frequency encoding gradient is applied following and perpendicular to the phase encoding gradient which causes proton spins to rotate at different frequencies. With this excitation order, the acquired MRI signal is spatially encoded so that can be stored in frequency domain via Fourier transformation. This domain is known as k-space and each data point consists of signal from the entire image field under the given gradient conditions. k-space data can be converted to image domain via inverse Fourier transformation to produce the final MR image [23].

Over the last two decades, MRI has become a dominant diagnostic imaging modality thanks to its ionizing radiation free mechanism, close to surgical grade excellent soft tissue contrast and 3D anatomical imaging ability in arbitrary planes [24]. Diagnostic MRI utilizes longer image acquisition times, segmented image acquisitions

to eliminate motion artifacts (i.e. ECG gated or respiratory gated imaging) and offline image reconstruction for higher image signal-to-noise ratio (SNR) [25]. Real-time MRI combines tailored acquisition, reconstruction and display strategies to provide images with minimum latency and temporal resolution comparable to X-Ray fluoroscopy. For this purpose, the size of the imaging matrix is generally reduced to support real-time imaging speed. In addition to the generic cartesian sampling strategies [26], under sampled rectilinear acquisition methods and non-linear sampling strategies including spiral and radial trajectories are also well-suited for real-time imaging [27, 28]. Image acquisition speed can also be accelerated utilizing multiple imaging coils and partial and/or parallel acquisition strategies [29, 30]. Currently, balanced steady-state free precession (bSSFP, also known as TrueFISP or FIESTA) is used as the work horse pulse sequence for real-time MRI due to its high SNR and short repetition times [31]. Even though fast spin echo techniques yield excellent image quality, they are less attractive for real-time MRI due to longer acquisition times and high specific absorption rates (SAR). Advancements in MRI technology coupled with high-performance multi-processor computers and graphic processor units (GPU) have eventually enabled real-time MRI with frame rates up to 10 frames per second with functional anatomical assessment [32, 33]. With these technical advances, MRI gained a growing interest also as a therapeutic tool and became a strong candidate to replace fluoroscopy for image-guided interventional procedures [1, 34].

2.3 Interventional Cardiovascular MRI (iCMR)

iCMR combines advanced real-time soft-tissue imaging in arbitrary planes, hemodynamics and potential intervention in a single radiation-free modality. Image-guided intervention and patient handling capabilities of MRI has been demonstrated and it was shown that the most common interventional procedures can be performed under MRI within the same time required for fluoroscopy [35–37]. Diagnostic cardiac catheterization has been the most common iCMR application so far [38]. Advantages of MRI for intravascular imaging of atherosclerotic plaques were shown [39]. Majority of the cases was right heart catheterization in children [3] and adults [40]. Antegrade

and retrograde left heart catheterization have also been performed under CMR guidance [41]. T_1 [42] and T_2 mapping [43], MR Thermometry [44] and Late Gadolinium Enhancement (LCE) MRI [45] techniques have been adapted to pre, intra and post procedural assessment of interventions. MRI has been used for personalizing ablation procedures and for real-time lesion monitoring. The feasibility of CMR-guided diagnostic electrophysiology studies [46], atrial RF ablation [35] and left ventricular chemoablation [47] have been demonstrated. Pre-clinical studies showed that real-time CMR guidance increases diagnostic biopsy efficiency [48]. Ventricular septal defect closure was performed through chest wall [49]. Early detection of bleeding using CMR prior the hemodynamic instability which is difficult with X-Ray fluoroscopy was shown during pre-clinical studies [50]. Additionally recanalization of chronic total occlusion [51], balloon angioplasty [52] and aortic valve replacement [53] were performed with CMR guidance.

However, all these mentioned procedures were performed using either MRI-safe conventional or limited non-metallic interventional X-ray tools. Alternatively, custom, experimental MRI compatible devices were used during pre-clinical studies. Consequently, clinical iMRI procedures are still hampered by the lack of clinical grade available MRI compatible devices (e.g. guidewires and catheters) for safe and effective interventions in patients [54].

2.4 Interventional MRI Devices

X-Ray fluoroscopy works on the principal of capturing unattenuated ionizing radiation to produce anatomical images. While this fact yields to inferior soft tissue contrast, it makes the interventional device design a relatively easy task for X-Ray guided catheterization. Metallic cores and braiding components are commonly used in interventional device designs to provide required mechanical characteristics including torque transmission, stiffness and pushability. These metals absorb the incident X-Ray photons which results in a noticeable contrast on the fluoroscopic image and provides device visibility under X-Ray. Additional radiopaque materials such as gold or tungsten

marker bands, can be used to provide more distinct contrast features. Practically, material biocompatibility is the only limitation for the interventional X-Ray device fabrication, in terms of material selection. However, most interventional X-Ray devices are either incompatible in the MRI environment are inconspicuous on the MR images.

MRI benefits from a strong magnetic field and RF energy deposition to obtain anatomical images. Ferromagnetic materials used for conventional interventional X-Ray devices are attracted by the strong magnetic field which prevents the use of such metals for iMRI device construction [55]. Some non-ferromagnetic metals may interfere with the local magnetic field and may ruin the image acquisition by disturbing local magnetic field homogeneity [56]. Long metallic wires, on the other hand, has the potential of RF-induced heating during the MRI RF excitation, due to standing waves on the wire and resistive mismatch at wire ends [57] which may cause serious burns. These limitations make the design of MRI compatible devices with clinically acceptable mechanical performance, quite a challenging task [25]. Since MRI works on a completely different principle than the fluoroscopy, additional attempts including an interaction with the main magnetic field and proton spins, are required to provide device visibility under MRI. iMRI devices are classified as passive, semi-active and active devices, in terms of device visualization and the need for connection to the MRI receiver chain.

2.4.1 Passive devices

Passive devices are visualized by the intrinsic material properties. They are attractive because of their simplicity and safety but they provide poor conspicuity. They appear as bright [58] or dark spots [59] on the image but navigation of passive devices is challenging due to the inferior device contrast (Figure 2.1). Positive contrast can be achieved using T1 shortening agents such as gadolinium [60] or more sophisticated agents such as ^{19}F and ^{13}C [61, 62] within the device body or on device surface [63]. Hence, such markers are visualized best using T_1-weighted pulse sequences. T_1 shortening agents used for positive contrast can be excited without the excitation of water

or fat proton spins by properly choosing excitation frequency and bandwidth. This method is known as off-resonance imaging [64]. Off-resonance imaging techniques enhance the device conspicuity but anatomic imaging may be limited. The main drawback of positive contrast passive devices is that the agents used on the device surface are unstable and device lumen requires to be filled with the contrast agent.

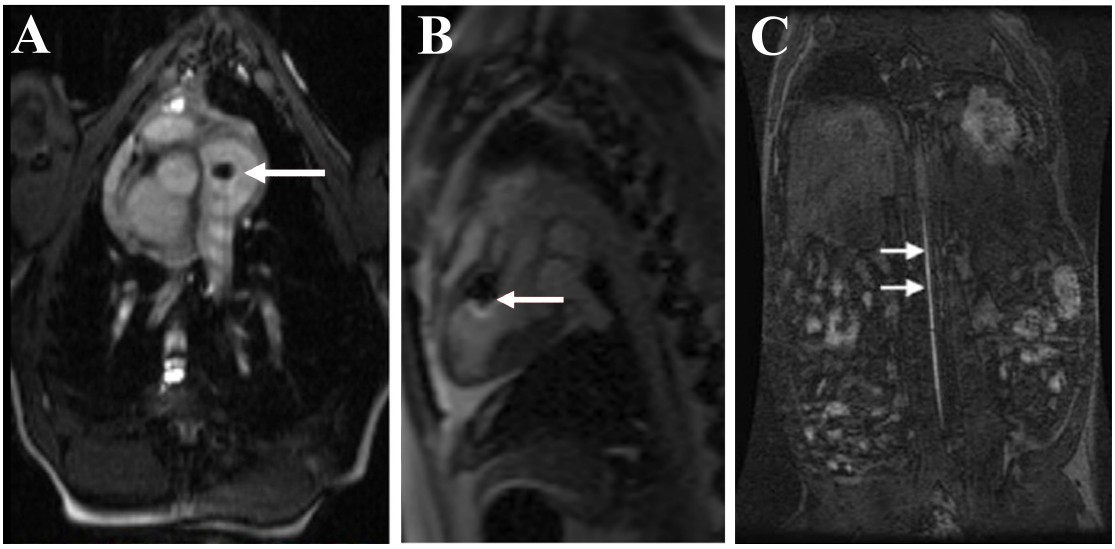


Figure 2.1 In-vivo imaging of passive markers. (A) Passive non-braided balloon catheter filled with CO_2 in a right atrium [65]. (B) Nitinol guidewire (Glidewire 260 cm/0.035", Terumo, Japan) with a high-UTS stainless-steel marker affixed at its tip during left heart catheterization at 1.5 T. (C) 4% Gd-DTPA coated 4 Fr catheter in a canine aorta [63]. White arrows point to the passive marker locations.

Negative contrast is achieved using marker materials that cause local magnetic field inhomogeneities which in turn result in dephasing of the surrounding proton spins. Such markers are visualized as signal voids (CO_2 filled balloon) or susceptibility artifacts. Negative contrast marker materials can be ferromagnetic (e.g. stainless steel), ferrimagnetic (e.g. copper zinc ferrite) or strongly paramagnetic (e.g. dysprosium oxide). Negative contrast markers are best visualized using T_2^*-weighted pulse sequences. As for intrinsic contrast properties, artifact shape and size of the passive devices depend of the pulse sequence and device orientation with respect to B_0. The artifact size of passive devices may obscure the surrounding anatomy or the signal signature can be confused with tissue margins. One distinct feature of passive devices is that marker signal cannot be turned off since the marker material is embedded in device

body. As an advantage, passive approach enables untethered iMRI device design and avoids many of the RF-related safety concerns.

2.4.2 Semi-active (inductively coupled) devices

Semi-active markers consist of fundamental circuit elements such as inductors and capacitors which together form an inductively coupled LC resonant tank circuit [66]. During MRI RF transmission, transmitted RF energy induces high currents on the inductor element of the semi-active marker (Figure 2.2).

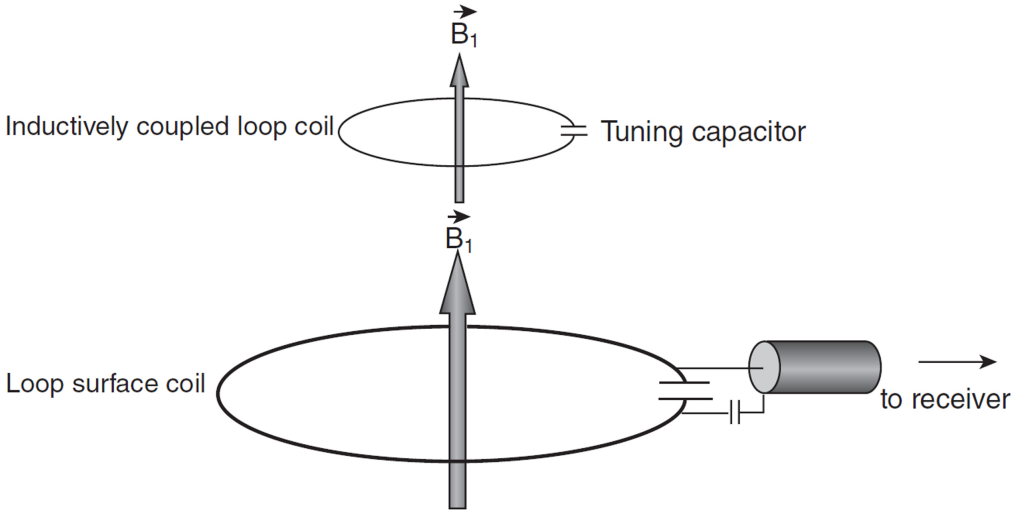


Figure 2.2 Working principle of semi-active markers. Coupling between a surface coil and a catheter-mounted semi-active marker coil is described [66].

Induced high currents generate a stronger local magnetic field around the inductor element exciting the close vicinity protons with a higher flip angle. This way, semi-active markers can be visualized as bright spots (Figure 2.3). These markers provide better contrast then passive markers. However, the local flip angle amplification so that the distinct device conspicuity diminishes as the flip angle so that the overall tissue excitation is increased. Reverse polarization imaging methods which utilizes forward and reverse polarization images separately, were introduced successfully to solve this problem [67,68]. The biggest advantage of semi-active markers is that they do not

require a direct connection to MRI scanner and in addition to the amplification effect, their signal can couple to the receive coils through mutual inductance. Semi-active marker visibility is limited with the marker coil geometry and varies significantly with the marker orientation with respect to B_0. Even though common practice is to place semi-active markers at the tip of the interventional tool, also multiple markers can be placed along the interventional device to provide multiple artifacts.

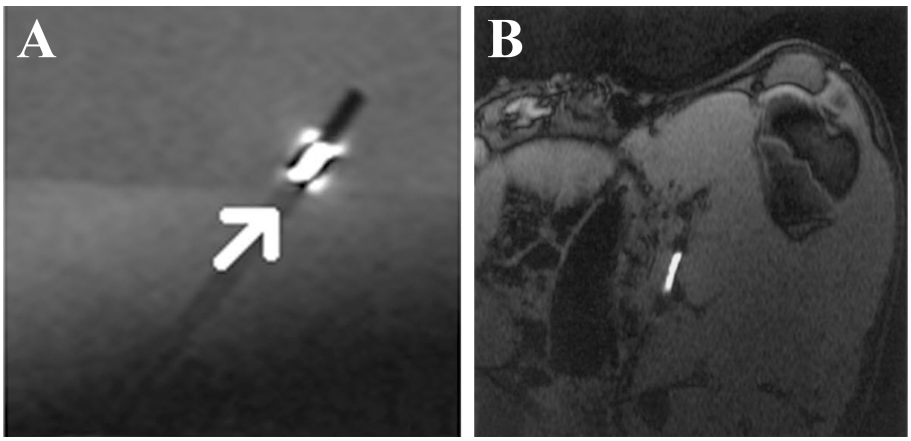


Figure 2.3 (A) In-vitro image of a thin-film coated semi-active marker at the tip of a 5 Fr catheter subassembly 45° orthogonal to transverse plane. (B) In-vivo image of a semi-active marker consisting of a resonant solenoid stent [66].

2.4.3 Active devices

Active devices incorporate RF antenna and transmission line components embedded in the device body and directly connected to the MRI RF chain to accomplish MRI visibility. RF-receiver coils integrated to the device body can detect nearby hyperintense MRI signal and theoretically exhibit high SNR, allowing unambiguous visualization (profiling) for safe and effective navigation and therapy delivery [69, 70]. Such RF-receiver coils can also be used for real-time device localization and automatic imaging plane adjustment (active tracking) [71, 72]. Their signal can be colorized and overlaid onto the anatomic image for enhanced device visibility, using dedicated real-time MRI interfaces [73] (Figure 2.4). Elongated or solenoid loop coils, or loopless RF antennas are commonly used for active iMRI device designs. Loop coils are well understood RF components in the MRI field since they are heavily used as surface receive

coils. A catheter loop coil can be easily formed by electrically shorting one end of a parallel transmission line [74]. Alternatively, the saddle coil geometry connected to a coaxial transmission line can be used as a catheter antenna [75]. Tuning and decoupling of the loop coil can be performed at the coil terminal, however, iMRI device size limitations have to be considered. Alternatively tuning and decoupling can be done remotely at the proximal end of the transmission line [76]. SNR of a loop coil increases with the insulation thickness, hence use of dielectric materials has an important role in the loop coil SNR. Wire separation is another factor affecting the loop coil SNR [74]. However, wire separation is limited with the size of the interventional device. Loop coil sensitivity changes with coil orientation with respect to B_0. As the coil is oriented parallel to B_0, it has a uniform radial sensitivity. However, as the coil orientation approaches perpendicular to B_0, radial uniformity may disperse. Loop coil sensitivity map can be calculated and the image pixel values can be multiplied with the inverse of the sensitivity map to acquire an image with a homogenous SNR. Solenoid coils are also used as an alternative to loop coils. Common practice is to use very short solenoid coils as distinct MRI markers or to determine the position of the interventional device (tracking). Solenoid coils can be used without tuning elements for tracking purposes since the radial SNR is not the main concern for such applications, so the coil signal can be carried using twisted pair or coaxial transmission lines. Multiple solenoids in series [37] or as separate channels [77] can be used to provide multiple MRI markers. Solenoid coil sensitivity also depends on the coil orientation with respect to B_0, however, using multiple coils 45° orthogonal to longitudinal axis of the device significantly improves coil sensitivity [78]. Unbalanced currents must be taken in to account while tuning and matching loop or solenoid coils since the electrical balance must be maintained in the matching and tuning networks [74]. Monopole [79] or dipole [69] loopless antennas also have been used for active iMRI device designs. The loopless antenna structure is attractive for iMRI device design thanks to its simplicity, miniaturization and high near-field SNR. A monopole loopless antenna can be easily constructed by extending the inner conductor of a coaxial cable. Very small diameter (0.014 inch) active guidewire designs were proposed using the monopole loopless antenna concept [80]. Loopless antenna does not require parallel capacitors to tune the antenna at Larmor frequency. Instead, the length of the extended inner conductor (whip) determines the

antenna resonance characterisitcs. A dipole antenna performs best when the lengths of poles are equal and total pole length is equal to the half wavelength of the Larmor frequency under specific loading conditions [81]. This length translates to quarter wavelength (∼12cm in human body at 1.5T) for monopole antennas since the whip is the dominant antenna pole and virtually whole outer conductor is the second pole [79]. The loopless antenna has a uniform radial sensitivity which decreases in radial direction with a function of distance. Sensitivity of the loopless antenna maximizes at the distal end of the outer conductor (junction) and decreases to zero towards the tip of the whip. Solutions for recovering this sensitivity loss is discussed in detail in the following chapters. Decoupling a loopless antenna can be performed via impedance transformation using a shunt PIN diode. The biggest advantage of loopless antenna-based active iMRI devices is that they provide full shaft visibility since the coaxial shield is a part of the antenna. A balun (balanced-to-unbalanced) circuit is generally required to suppress the common mode currents on the shield of loopless antennas.

One disadvantage of the active devices is that the electrical connection between the iMRI device and MRI system limits the operational flexibility. Additionally, by virtue of incorporating long conductive wires, active devices are generally prone to RF induced heating [82].

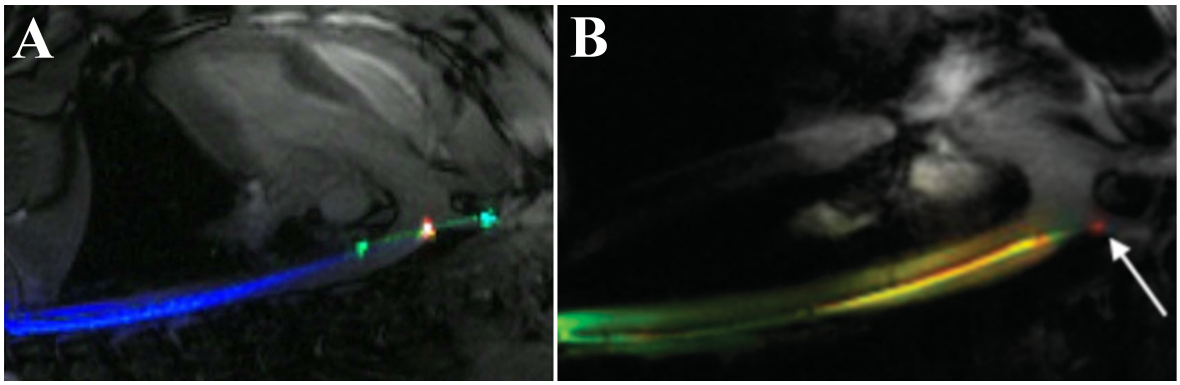


Figure 2.4 (A) In-vivo MRI of an active guiding catheter with a loopless antenna and three solenoid markers in the aorta [83]. (B) In-vivo MRI of a two-channel active guidewire consists of a loopless antenna for the shaft visibility and a solenoid coil at the tip, in brachiocephalic artery. White arrow indicates the active guidewire tip [69].

2.5 iMRI device development

Most commercially available devices for limited iMRI procedures are visualized passively. Such devices either rely on signal voids thanks to air filled balloons or magnetic susceptibility artifacts induced by the metallic components embedded in device body, for MRI visibility. Such devices can be difficult to identify on the anatomical background image due to poor contrast. Otherwise, device MRI signature can be confused with complex anatomical boundaries or the artifact size may obscure the surrounding anatomy.

Active devices are more attractive for clinical iMRI procedures compared to passive and semi-active devices because of their unique signal signature and high SNR device artifact. Due to limitations of MRI mentioned so far, metal parts such as braiding and pull wires of conventional interventional devices need to be replaced with non-metallic components or MRI safe metals for the iMRI device fabrication. Then, RF resonator or antenna parts are integrated to device body for a distinguishable MRI visibility [77]. Using copper wires and off-the-shelf electronic components for this purpose is not always acceptable because of intolerable device profiles, mechanical performance and magnetic susceptibilities. Additionally, insulation of conductive components needs to be taken into account since each insulation layer may alter the device profile and mechanical characteristics. These parts, at first, were produced using hand wound coils and commercially available rigid and bulky electronic components which are clinically unacceptable. Then, micro electro mechanical systems (MEMS) based production methods including lithography [84], aerosol deposition [85], hot embossing [86] and thin film technology [87] were quickly implemented to low profile, flexible iMRI device fabrication. Although the performance of these methods is sufficient for planar productions, they do not perform well enough on non-planar surfaces. Therefore, 3D fabrication methods including 3D laser lithography [88], conductive ink printing [89], wrapping flexible circuit sheet [90] and the use of focused ion beam sputtering [91] were introduced to overcome the drawbacks of MEMS based planar fabrication methods.

Proposed MEMS based methods in the literature are generally modified planar fabrication techniques which are good engineering approaches but not suitable for multi-layer non-planar fabrications. Thin film based coating methods use thermal evaporator or sputtering systems and require long vacuum times. Special shadowing masks are required to form desired patterns and misalignment errors may occur for multi-layer fabrications. Nanometer scale ultrathin layers can be obtained using thin film coating method. However, for the 1.5T MRI system, at least 9.8 μm skin depth is required to carry the MRI signal without a major loss [92]. Layer thickness is generally increased by copper electroplating. Adding a relatively thick copper layer reduces the device flexibility due to the fragile intrinsic property of the copper layer after electroplating. Besides, thin film production method is not applicable for long interventional devices because of the very limited space of the vacuum chambers. 3D lithography techniques, on the other hand, uses chemical etching or laser ablation to obtain desired patterns. In both processes, control of the ablation depth is very difficult and multilayer fabrication is not so feasible. Furthermore, chemicals used for etching are not bio-compatible and limit the clinical grade device fabrication. The need for copper electroplating also presents for 3D lithography technique. Aerosol deposition can be implemented for non-planar multilayer fabrication successfully, however, the adhesion of conductive mixture used in aerosol deposition is not sufficiently strong on polymer surfaces commonly used for iMRI device construction. Primers used to enhance the adhesion, on the other hand, are not biocompatible. As a result, iMRI devices fabricated using these techniques so far remained as a proof of concept and could not be translated to the clinic due to insufficient mechanical and electrical performances.

2.6 MRI Safety

This section focuses mostly on the iMRI device safety. Thorough patient screening and safety of patient care equipment are discussed briefly. MRI employs a high strength static magnetic field and rapidly changing electromagnetic fields to generate anatomic images. Each of these fields has to be taken into account to avoid potential safety risks for procedures and medical devices utilized for interventional MRI. The high

strength main magnetic field (B_0) can apply a significant displacement force and/or torque on ferromagnetic materials such as conventional metals used for interventional X-Ray device designs, attracting them towards the scanner bore. All medical equipment in the MRI environment, used for diagnostic or therapeutic purposes, patient care or procedure monitoring must be non-magnetic or labeled properly to avoid any safety hazards. Similarly, patients with metallic implants need to be screened properly. Magnetically-induced displacement force and torque test methods to ensure iMRI device safety, and corresponding safety margins are defined by regulatory institutions and described in detail by American Society for Testing and Materials (ASTM) International within ASTM F2052-15 [93] and ASTM F2213-17 [94] standards, respectively.

Magnetic field gradients used for spatial encoding of proton spins and the pulsed RF electromagnetic field (B_1) used for the spin excitation generate rapidly changing electromagnetic fields which may have a heating effect. Alternating currents can be induced on conductive loop structures when the loop is positioned perpendicular to an electromagnetic field according to Faraday Law [95]. Induced alternating currents can cause resistive or Joule heating in the vicinity of the loop. The rate of change and strength of the magnetic field, number of loops and the loop area directly affect the voltage induced on the loop due to the changing magnetic field [96]. A resonant loop can increase the heating. In addition to the inductive heating, eddy current formation may also occur on non-circular conductors which generates opposing magnetic fields due to Lenz Law [97]. The induced current increases with the increasing rate of change and strength of the magnetic field and conductivity of the material.

Patient nerve stimulation is the most common physiological adverse effect of rapidly changing magnetic fields and limits the slew rate (the rate at which the field reaches its final value) of the magnetic field gradients [98]. Additionally, high RF power deposition during transmission, may cause tissue heating because of eddy currents induced in the body [99]. The RF energy is mostly absorbed around transition boundaries such as the transition from air to body during MRI exams. This is because of the changing electrical conductivity and relative permittivity between mediums which results in reflection of the RF energy and resistive losses. As a result, maximum poten-

tial tissue heating most likely occurs in skin tissue and decreases towards the center of the body. However, the wavelength in the body in higher field strengths may change this pattern [100]. Even though there is not a consensus in the literature about the definition of safe upper limits in terms of tissue heating, general view agrees that tissue temperature rises above 41°C for a long period of time (>20 minutes) may cause tissue damage [101]. Specific Absorption Rate (SAR) is defined as a measure of RF power deposition. Clinical MRI exams are limited with 2 W/kg and 4 W/kg whole body SAR in the "normal" and "first level" modes, respectively, and monitored continuously to ensure that tissue temperature remains under 41°C.

Presence of coiled or elongated conductors within the body, in forms of implants or interventional devices (such as guidewires or metal braided catheters) increases the risk of RF-induced heating. Especially, RF antenna components used for iMRI device designs are specifically tuned at Larmor frequencies and efficiently couple with the high RF energy deposition unless preventive measures are taken. On the other hand, conductive elements used for iMRI device designs such as pull wires, metal braids or metallic cores/scaffolds couple with the nearby tangential electric field (E-Field) [102]. Coupled E-fields along the metallic component adds up constructively and concentrates at the ends or sharp edges of metallic implants. For the partially inserted interventional devices, such concentrations occur at the device tip within the body and the body entry point [103]. In addition to the amplified E-fields at conductor ends due to induced currents, standing waves also form over the implants and interventional devices, causing additional heating because of the reflections at conductor ends and resistive mismatch at the transition boundaries (conductor-to-tissue) [82]. These focal, high E-field points are referred as "hot spots" and maximum RF-induced heating is expected in these sections of iMRI devices. Coupling of a conductive element with the transmitted RF field maximizes when the device length approximates to half wavelength of the Larmor frequency causing resonance effects [104]. In this case, the conductor element acts as a linear antenna and this length is referred as the "resonance length". Maximum RF-induced heating can be expected at resonance lengths due to high induced potentials so that voltage dissipation at device ends or transition boundaries. The E-field concentration leads to amplified local SAR which can be calculated using Eq 2.1 in units

of Watt/kg [103].

$$SAR = \frac{\sigma E^2}{2\rho} \tag{2.1}$$

where σ is the electrical conductivity (S/m), E is the amplitude of the E-field (V/m) and ρ is the mass density of the medium (kg/m^3). Local SAR values can be used to estimate the local RF-induced heating via bioheat transfer using Eq 2.2 [105]

$$SAR = \lim_{t \to 0} c \frac{\Delta T}{\Delta t} \tag{2.2}$$

where c is the specific heat capacity (J/kg℃, 4150 for the ASTM gel phantom), T is the temperature (℃) and t is time (s).

Various methods have been introduced to limit or minimize the RF induced heating so that to enhance RF safety of active iMRI devices and elongated metallic iMRI tools. The most fundamental approach is to use a shunt PIN (positive-intrinsic-negative) diode to actively detune the coil element or introduce high impedance to the loopless antenna junction to minimize RF coupling during transmission [79]. Similarly, a balun is commonly used within the tune and match network to induce high impedance selectively to common mode shield currents without attenuating differential mode currents [81]. Integrating quarter wavelength coaxial chokes (Bazooka balun) [106], floating RF chokes [107] or miniaturized baluns [108] onto the transmission line have been alternative means of common mode current suppression.

High impedance cables were used as transmission lines [109] to minimize current induction. Transmission lines have been segmented shorter than the resonance length and RF signal was inductively coupled between segments [110] to minimize standing wave formation on transmission lines. Also, a metallic guidewire design was introduced with electrically interrupted yet mechanically coupled segments to mitigate RF-induced heating [111]. Alternatively, optical fibers were used to replace metallic transmission lines and to detune coil elements to completely eliminate E-field coupling [112, 113]. Recently, opto-acoustic sensors were used in combination with optical transmission lines to mitigate RF-induced heating [114].

Closed loop control methods were implemented by actively changing matching network characteristics [115] and the shield impedance of a pacemaker [116] to again minimize standing wave formation over the active iMRI devices. Another approach was to monitor and actively control the induced currents over a guidewire using a toroidal trans-receiver sensor [117]. Parallel transmission methods have been successfully implemented to reduce RF-induced heating without making adjustments on the iMRI device design [118, 119]. Alternatively, low-SAR custom imaging pulse sequences helped to reduce the RF-induced heating of iMRI devices [120].

Recently, the biggest development for the iMRI device safety has been the introduction of the 0.55T high-performance low-field MRI technology [121]. The reduced RF power deposition (9-fold compared to 1.5T systems) [122, 123] and increased electrical wavelength (3-fold compared to 1.5T systems) [103, 124] afforded by contemporary high-performance low-field systems inherently enhance iMRI device electrical safety.

Despite all the advantages of the high-performance low-field MRI systems in combination with the RF safety enhancement techniques mentioned so far, complete elimination of the RF-induced heating is not possible in practice. Hence, RF safety of iMRI devices needs to be tested and verified according to regulatory standards.

2.6.1 RF safety test methods for active iMRI devices

RF safety of metallic implants and iMRI devices are tested per ASTM 2182-19 [125] and ISO/TS10974 [126] standards.

ASTM 2182-19 test method is performed in a gel phantom with electrical conductivity of 0.47 S/m and relative permittivity of 80±20 which mimics average human body loading conditions. Phantom liquid is prepared in a gel form to increase consistency and minimize convectional heat losses. Next, the SAR distribution in the gel phantom is mapped either using MRI compatible E-field/SAR probes or measuring gel temperature in discrete spatial locations and calculating the local SAR values using

Eq. 2.2 Alternatively, the estimate SAR distributions given in the standard can be referred. Once the local SAR values within the gel phantom is mapped, the implant or the interventional device under test is positioned in the maximum SAR area. For the given phantom dimensions in the standard, the highest SAR values can be measured near the upper right and lower left edge of the phantom (on the axial plane and from Z- standpoint) for the commonly used 1.5T and 3T clinical MRI scanners (Figure 2.5). The asymmetry of the E-field so that the SAR distribution is a result of the circularly polarized electromagnetic field within the 22.5° rotated birdcage coil used for RF excitation. Three temperature probes are placed on the test subject where the maximum RF-induced heating is expected (Figure 2.6). The base line temperature is recorded for at least 30 s to record the gel temperature. Next, MRI scan is performed for 15 minutes. Once the MRI scan stops, cooling of the test subject is recorded at least for another additional 3 minutes. Maximum RF-induced temperature rise (ΔT) can be calculated by subtracting the baseline temperature from the maximum recorded temperature during the test.

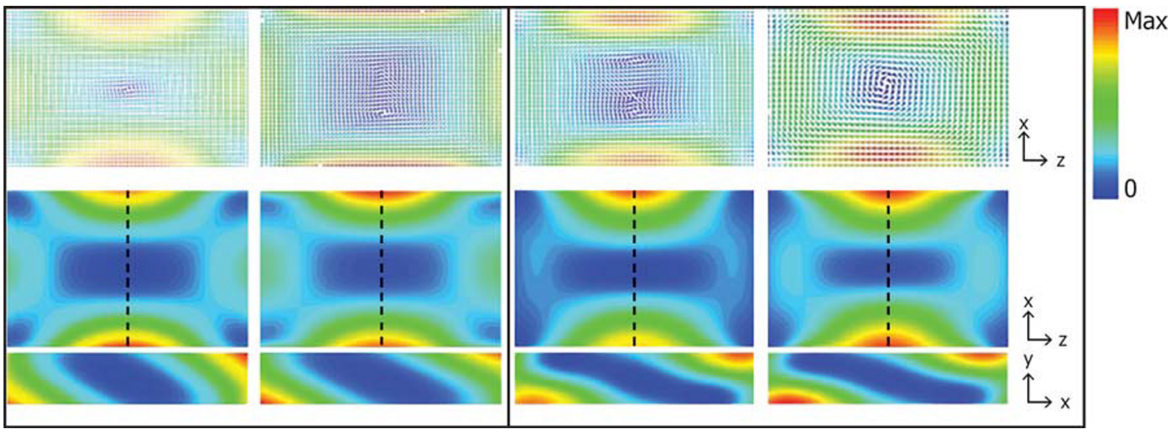


Figure 2.5 Example Images of Electric Field and SAR Distributions in a Phantom at 1.5T (left) and 3T (right). Electric field distributions are shown in the XZ plane (top), while SAR distributions are shown in the XZ plane (middle) and in the XY plane (bottom), respectively. The dashed lines show the axial location where the XY cross-sectional planes are acquired [125].

The recorded temperature rise needs to be normalized for 1 W/kg background SAR to standardize the test results independently from pulse sequence parameters. Aside from dedicated MRI compatible E-field/SAR probes, a 10 cm long titanium

reference rod placed at an identical SAR location (symmetrically with the test subject) can be used for this purpose. In this case, a fourth temperature probe is placed on the titanium rod (Figure 2.6). The RF-induced temperature rise of the reference rod is divided by the temperature values given in the standard (resulting from a 1W/kg background SAR) to calculate the background SAR and normalize the test results. However, the reference temperature rise is provided only for 1.5T and 3T systems and other field strengths are not covered.

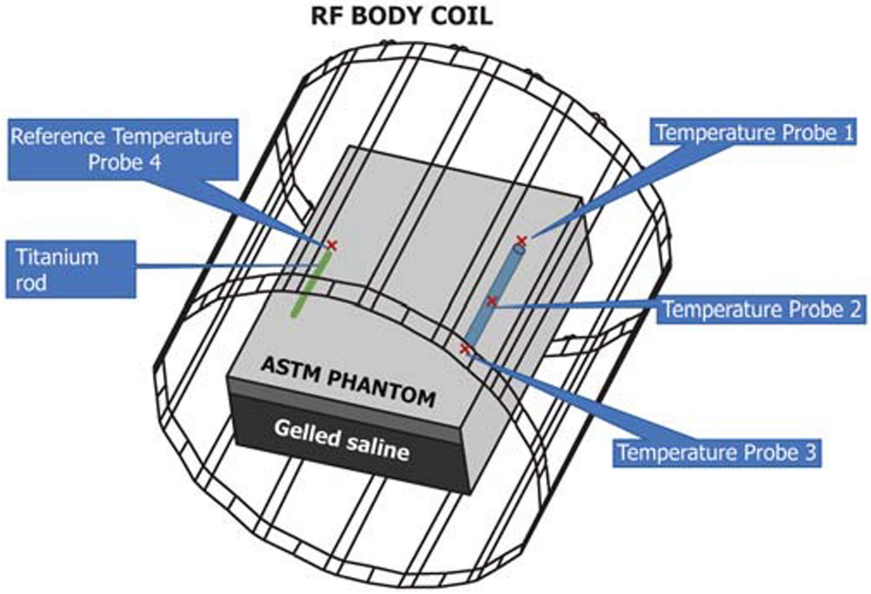


Figure 2.6 Example diagram of apparatus for testing of RF heating near an implant during MR imaging. Three temperature probes are placed on the test subject and another probe is placed on the reference rod [125].

Even though ASTM 2182-19 is widely used among researchers to assess the RF safety of iMRI devices, the most important limitation of this standard is that it is originally designed for RF safety assessment of completely inserted metallic implants. It assumes the test subject is completely inserted into the body and exposed to a homogenous E-field. However, this is never the case for partially inserted iMRI tools. Moreover, the RF-induced heating performance of an iMRI device dramatically changes depending on the insertion length and the phase distribution of the E-field around the device [103, 127, 128]. As a result, testing of the partially inserted iMRI devices is limited with the span of the insertion length and device positioning within the phantom

during tests. Recently, ISO/TS 10974 standard [126] has been introduced based on the "transfer function" approach to take the heterogenous field distribution into account and investigate the RF safety of iMRI devices for any given arbitrary insertion length and device trajectory within the body which cannot be tested experimentally.

Transfer function method aims to calculate the E-field so that the SAR amplification at the ends of an interventional device using the transmission line theory [102]. It assumes that the conductor under test couples only with the tangential E-field. The coupled E-field is transferred along the transmission line by being attenuated and phase-shifted, resulting in a constructive or destructive contribution to the E-field/SAR amplification at the hotspot(s) Figure 2.7. ISO/TS 10974 divides iMRI devices in four tiers based on the complexity of the device design, application type and the feasibility of comprehensive experimental measurements. Most of the contemporary iMRI devices fall into tier 3 or tier 4. In this section, implementation of only tier 3 is described. However, the only difference between tier 3 and 4 is that tier 4 requires inclusion of the actual device model into simulations of RF-induced heating tests for any given scenario while tier 3 accepts mathematical calculations validated by in-vitro tests.

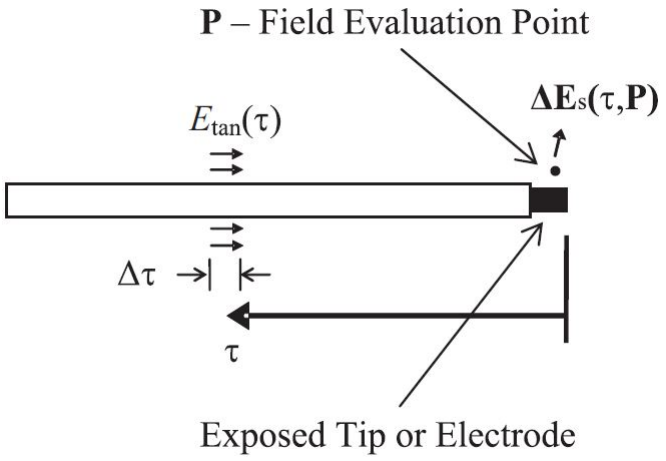


Figure 2.7 Application of a tangential E-field (E_{tan}) over a small length ($\Delta\tau$) at a location along the test subject results in a scattered E-field (E_s). τ is the distance of the field excitation point from the end of the test subject and P is the position vector where the scattered field is evaluated [102].

Transfer function measurements can be divided into two steps. First step includes the benchtop measurement of the actual transfer function. For this purpose, the device under test is immersed in a liquid phantom with similar electrical characteristics to the human body. ASTM gel phantom can be used for this purpose. Next, a local tangential field is applied onto the test subject, and the amplitude and phase of the scattered E-field at the previously detected hotspot is measured (Figure 2.7).

The local E-field source is moved along the test subject in short steps and the scatter E-field is measured for each excitation point. This task can be performed via piecewise excitation using a 1V/m tangential E-field source moving on the test subject and a stationary E-field sensor at the hotspot [129]. Alternatively, reciprocity principle can be exploited and the test subject can be excited with a 1A sinusoidal current source either directly soldered [130] or inductively coupled via a short monopole antenna [131] to the test subject at the hotspot. In this case, the scattered E-field along the test subject is measured using a RF current probe. The transfer function ($S_1(\tau)$) can be calculated using Eq 2.3.

$$S_1(\tau) = \frac{1}{E_{tan}(\tau)} \frac{\Delta E_{1r}(P)}{\Delta \tau} \tag{2.3}$$

Where $E_{1r}(P)$ is the radial component of the scattered E-field at point P. The scattered E-field as a result of discrete tangential E-field excitations can be calculated using Eq 2.4 [102].

$$E_S(P) \approx \ E_1(P) \int_0^L S_1(\tau) E_{tan}(\tau) d\tau \tag{2.4}$$

Where $E_1(P)$ is the scattered E-field due to a unit E_{tan} along the test subject and S_1 is a normalized transfer function which is a complex scalar (amplitude and phase) and L is the device length. Normalizing constant α can be calculated with Eq 2.5.

$$\alpha = \int_0^L S_1(\tau) E_{tan}(\tau) d\tau \tag{2.5}$$

As described with Eq 2.1, the local SAR value at the hotspot can be calculated using

Eq 2.6.

$$SAR\,(P) = \frac{\sigma\,(P)}{2\rho\,(P)} E_S(P) E_S^*(P) \approx \frac{\sigma\,(P)}{2\rho\,(P)} |\alpha|^2 E_1(P) E_S^*(P) \tag{2.6}$$

where σ(P) is the conductivity of the medium and ρ(P) is the mess density. Here, the contribution of the tangential E-field along the test subject on the E-field/SAR amplification at device ends can be calculated using the transfer function.

Second step includes calculation of the tangential E-fields along the test subject via electromagnetic simulations and estimating the RF-induced heating using the previously derived transfer function. For this purpose, the RF system used in the MRI scanner is simulated and the simulation results are validated via experimental field mapping. Once the simulation setup is validated, virtual human body models can be simulated with the same setup and tangential E-field along any arbitrary trajectory in the air and body can be extracted (Figure 2.8). After this point, extracted tangential E-field values can be used as transfer function inputs and the local SAR so that the RF-induced heating at the hotspot can be calculated. Hence, RF safety of iMRI devices can be tested and validated for in-vivo use conditions and the worst case RF-induced heating (when the phase distribution of the incident E-fields always contributes constructively) can be defined using the transfer function approach.

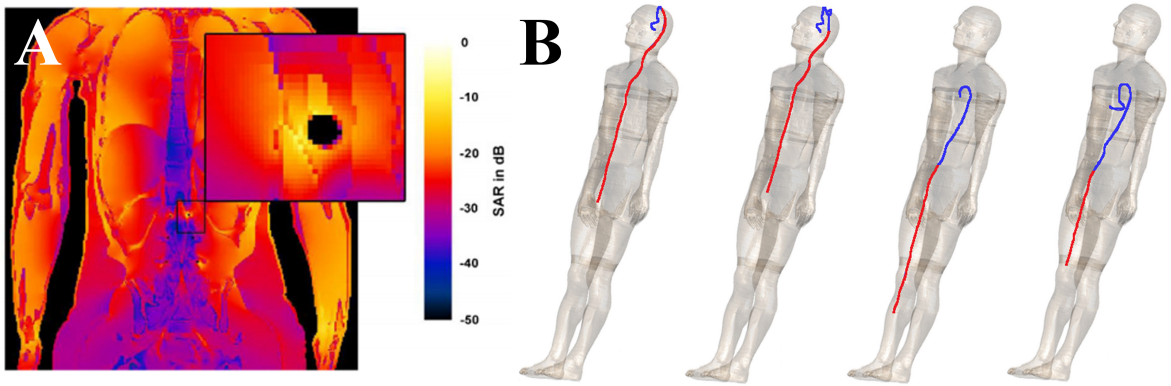


Figure 2.8 (A) Local SAR distribution in a virtual human body at 1.5T based on electromagnetic simulation results [132]. (B) A virtual human body within the RF transmit volume coil in the electromagnetic simulation environment and arbitrary iMRI device trajectories where the tangential E-fields are extracted [130]. Blue sections indicate the device portion inserted into the body. Red sections indicate the device portion remains outside the body.

In addition to the piece wise excitation and reciprocity principle, MRI based transfer function methods have also been introduced however accuracy of these methods for solenoid structures needs further investigation [133, 134]. It is no doubt that the transfer function is a novel approach and enables comprehensive assessment of iMRI devices' RF safety which is not feasible via experimental methods. However, calibration and certification of the equipment required for the transfer function measurements including the exciter and MRI compatible E-field and SAR probes are limited with 1.5T and 3T Larmor frequencies. Most of the calibration labs worldwide do not have certified calibration setups for low-field Larmor frequencies. As a result most required equipment are not readily available for low-field at the moment which limits the accuracy of transfer function measurements at low-field frequencies.

2.7 Electromagnetic computation and modelling in MRI

Computational modelling has been applied in various fields of medicine so far. Few examples include the use of MonteCarlo simulations by medical physicists to study radiation transport during diagnostic and therapeutic ionizing radiation applications, and the use computational fluid dynamics (CFD) by clinicians to better understand the cardiovascular system and investigate arterial blood flow. Similarly, computational biomechanics (CBM) has been employed to study soft tissues, bones and joints. Computational modelling has also been applied to medical device design and development such as CFD for developing blood pumps, stents and artificial heart valves, and CBM for the development of artificial tissues and organs [135].

With the developing high capacity computational systems, sophisticated software packages and high resolution human model, electromagnetic (EM) computation and modelling have been heavily employed in MRI field in every aspect from design and development of the system components to patient and equipment safety. Main magnet design and optimization [136], B_0 homogeneity and shimming [137], biological effects of the strong magnetic field [138], gradient coil design and optimization [139], peripheral nerve simulation [140] and RF coils have been the main topics investigated

using computational EM tools. Computational RF coil studies involved transmit coil design and optimization [141], B_1 homogeneity [142] and receive coil design, optimization and SNR [143]. Local SAR distribution within the human body is apart from being homogenous and patient-specific, hence experimental investigation of patient safety is nearly impossible. RF safety of patients during clinical MRI exams also has been extensively investigated with electromagnetic simulations [144].

Electromagnetic modelling for implant safety and active iMRI device visibility certainly have been the most important topics for iMRI field. Electromagnetic modelling using Maxwell equations aims to investigate how the electromagnetic fields in the MRI environment interact with implantable medical devices, especially active iMRI devices with elongated metallic components since unpredictable, complex couplings may result in RF safety concerns in addition to the unwanted image artifacts [144]. As discussed in the previous section, computational electromagnetic studies supported by experimental findings showed that metallic components can induce amplified RF power deposition in the tissue resulting in RF-induced heating which may change dramatically depending on the dimensions, shape, location and orientation of the implant. Experimental investigation of implantable medical devices for every possible clinical use condition is not feasible for many reasons including ethical concerns. Hence, the importance of electromagnetic simulation tools for medical device development has been recognized by United States Food and Drug Administration (FDA) with a guidance document [145] and the use of such computational tools has been mandated for certain iMRI tools and implants by regulatory standards [125, 126]. In addition to the improved safety benefits, electromagnetic simulation tools can be used to study receive sensitivity profiles of active iMRI devices which can be used to predict the image signature of the device [81].

Electromagnetic simulation tools are mainly divided into four categories based on the solver type. Finite element methods (FEM) and finite-difference time-domain (FDTD) solvers are the most used kinds. However, surface integral equation (SIE) and volume integral equation (VIE) solvers have also been used in recent studies [146, 147]. Each solver has advantages and disadvantages for each specific application. FEM

solvers use tetrahedron and triangular discretization so that large models incorporating small features can be simulated efficiently however anatomical data acquired with CT or MRI cannot be efficiently discretized. They use high RAM capacity and central processor units (CPU) for computation so that simulations cannot be accelerated using graphical processor units (GPU). However, they can perform multi-port RF coil simulations in a single solve [148]. FTDT solvers use rectangular voxels for discretization so that voxel body models can be efficiently simulated. They require lower RAM capacity compared to FEM solvers and they can be easily accelerated using multiple GPUs. Time-domain broadband coil response can be evaluated in a single simulation using FTDT solvers. However, simulation time increases with decreasing voxel size because of the reduced time steps [149]. SIE and VIE solvers are compatible with voxel body models and they can easily model thin structures. Their biggest advantage is that they do not require absorbing boundary conditions so that only the coil/device model can be simulated. Similar to FTDT solvers, they require low RAM capacity and they can be accelerated using multiple GPUs [150].

2.8 Specific aims

We hypothesized that advantages of MRI coupled with safe-by-design, clearly visible and mechanically sufficient interventional tools can provide physicians with a better and safer image-guidance to perform routine and complex cardiovascular procedures using endovascular or minimally-invasive approaches. Our objective was, first, to introduce reliable and repeatable design and fabrication methods for iMRI device development and then to provide a set of fundamental interventional tools including an active needle, a metallic active guidewire and a MRI-safe metallic catheter to cover a wide range of interventional cardiovascular procedures under MRI, and in long term, to enable clinical implementation of iCMR in suitable target applications.

Based on the background summarized above and the gaps in our understanding of interventional MRI device design and development, the objective of this thesis study was completed through the following specific aims:

1. **Improvement of the conductive ink printing method and testing of clinical grade iMRI device fabrication capabilities.**

   Previously, the conductive ink printing method was introduced by our group as a precise, reliable, repeatable, and time and cost effective method for iMRI device fabrication. In this study, the conductive ink printing method was improved by employing biocompatible heat shrink polymers and closed-loop control of the ink flow. Using this method, desired part geometries (e.g. RF antenna parts and transmission lines) for MRI visibility could be formed directly onto heat-shrink polymers by depositing silver nano-particles containing ink mixture with a custom, computer controlled printing system. Polymer layers incorporating printed parts were transferred onto the device body thereafter. Rapid active iMRI device fabrication and medical grade device fabrication capabilities of the improved method were tested.

2. **Establishment of electromagnetic simulation setups to address design and safety challenges in iMRI device development.**

   Electromagnetic (EM) simulation setups were established using FDTD and FEM solvers to investigate the near field SNR profile and RF safety of various active and passive iMRI device designs. Optimum design parameters were defined via EM simulations eliminating costly iterative design steps. Magnetic field vectors were studied to better understand the relationship between the coil characteristics and the RF magnetic field, and to predict MRI signature of iMRI devices which is quite difficult to perform via experimental measurements. Experimental validations were performed to further improve the accuracy of modelling and to gain sufficient confidence in simulation results to address future challenges.

3. **Development of a 20 Gauge active needle design with thin-film printed circuitry for interventional MRI at 0.55T.**

   Needles are widely used in interventional medicine for interventional access, injection, tissue aspiration and tissue sampling. A 20 G active needle design was developed for interventional MRI at 0.55T using improved conductive ink printing method. A series of electromagnetic simulations were performed to define

optimal setpoints for the device RF antenna geometry. Active iMRI needle prototypes with a printed RF antenna were built based on the simulation results. In-vitro and in-vivo MRI visibility and in-vitro RF-induced heating performance of the prototypes were tested and compared to a typical active iMRI needle built using manually wound insulated copper wire RF antenna at 0.55T.

4. **Development of a 0.035" outer diameter actively visualized, metallic guidewire with unique curved tip geometry and complete device visibility for interventional MRI at 0.55T.**

   Guidewires are workhorse tools of interventional cardiology. They are heavily used to navigate through narrow vasculature and gain access to target heart chamber. A 162.5 cm long monopole antenna-based active iMRI guidewire with 0.035" outer diameter was developed for high performance human cardiac catheterization at 0.55T. Electromagnetic simulations were performed to study the magnetic field around antenna whip. The active guidewire prototype was manufactured using medical grade materials in an ISO Class 7 cleanroom. RF-induced heating performance of the active guidewire prototype was tested in a gel phantom per ASTM 2182-19 both alone and in tandem with a metal braided catheter. In-vitro and in-vivo real-time MRI visibility was tested in one gel phantom and in one swine, respectively. The mechanical performance was tested in terms of stiffness, trackability and torque transmission, and compared to commercial equivalents.

5. **Development of a MRI safe, metal braided catheter design for interventional MRI at 1.5T.**

   Non-metallic catheters cannot provide the mechanical performance required for interventional therapy delivery. Metal braiding is commonly used for cardiovascular catheter designs to provide sufficient column strength, kink resistance and torque transmission. Metal wire braided 6 Fr catheter shaft subassemblies were built using electrically insulated stainless-steel wires and off-the-shelf biocompatible polymers. Braiding pattern was investigated and electromagnetic simulations were performed to define the segmentation strategy. The metal braiding was segmented, in-situ, using lasers to create non-resonant wire lengths. The heating and

mechanical performance of segmented metal braided catheter shaft subassemblies was compared with those of the unsegmented subassemblies.

2.9 Thesis Outline

A brief introduction and motivation of the thesis study is presented in chapter 1. Advantages of minimally-invasive diagnostic and therapeutic methods over surgical procedures, current imaging modalities used for the image guidance of cardiovascular interventions and work principals of MRI are discussed in chapter 2. Real-time MRI, iMRI device types, challenges in iMRI device development, MRI safety and electromagnetic computational modelling topics are also discussed in this chapter.

Chapter 3,4 and 5 are the main chapters discussing the development of most fundamental interventional devices to enable broad applications of iMRI as a clinical tool. Chapter 3 describes the improvements implemented on the conductive ink printing method and introduces a 20 G active needle design with printed RF antenna for iMRI at 0.55T. Chapter 4 introduces a metallic active guidewire design with clinically acceptable mechanical performance, a continuous tip and whole device visibility and 162.5 cm length to allow catheter exchange, for iMRI at 0.55T. Finally, a MRI-safe metal braided catheter design is introduced for high performance human catheterization at 1.5T in chapter 5. These main chapters consists of individual Introduction, Materials and Methods, Result, Discussion and Conclusion sections which provide application specific information in addition to chapter 2.

3. A 20 GAUGE ACTIVE NEEDLE DESIGN WITH THIN-FILM PRINTED CIRCUITRY FOR INTERVENTIONAL MRI AT 0.55T

3.1 Introduction

Hollow needles are in widespread medical use for delivery of therapeutic materials, tissue aspiration and sampling, tissue drainage, and device delivery during minimally invasive procedures [151]. Needle positioning is performed "blind" guided by anatomic landmarks [152], palpation or aspiration [153]; or guided by imaging such as X-ray fluoroscopy [154], CT [155], ultrasound [156] or MRI [157–160] for precise navigation. MRI is of particular interest for image-guided needle interventions because it permits ionizing radiation free procedures with exquisite soft tissue contrast superior to other imaging modalities [2, 4, 25]. Moreover, imaging windows are available in any arbitrary orientation providing real-time 3D anatomical data at up to 10 frames per second (fps) [73, 161, 162] which is comparable to the temporal resolution of X-Ray fluoroscopy and ultrasound, and sufficient for most minimally invasive operations [162].

The combination of RF transmission and a strong magnetic field in the MRI environment makes interventional MRI (iMRI) devices difficult to design. Additional efforts including an interaction with the main magnetic field (B_0) and proton spins are required to render interventional devices conspicuous under MRI [4]. iMRI devices can be categorized as passive, semi-active and active in terms of device visualization. Passive devices provide negative (dark) or positive (bright) contrast on the image [163] via signal voids [164], metallic susceptibility artifacts [165, 166] or using T1-shortening agents [58]. Commercially available metallic needles suitable for the MRI environment are visualized passively [56]. Such needles typically suffer ambiguous tip and shaft visualization especially at targets such as tissue interfaces and blood vessel margins which can exhibit magnetic susceptibility artifacts [167, 168]. Semi-active devices (resonant markers) inductively couple with the transmitted RF-energy and excite the surrounding

tissue with an amplified flip angle generating a bright signal on the image [169, 170]

Active iMRI devices incorporate electronic components directly connected to the MRI hardware receiver chain to accomplish MRI visibility [171]. RF-receiver coils integrated to the device body can detect nearby hyperintense MRI signal and theoretically exhibit high SNR, allowing unambiguous visualization (profiling) for safe and effective navigation and therapy delivery [37, 79, 172]. Such RF-receiver coils can also be used for real-time device localization and automatic imaging plane adjustment (active tracking) [71, 173]. Adversely, long metallic components integrated into such device designs are prone to RF-induced heating during real-time MRI [103]. However, various electrical safety enhancements have been introduced to mitigate RF-induced heating [79, 108, 114, 115, 120, 123, 174, 175] encouraging the design and use of active iMRI devices The reduced RF power deposition at low field strengths inherently enhances electrical safety [122,123,176]. Also, the increased electrical wavelength (33 cm for an uninsulated wire) at low-field improves safety margins 3 and 9 fold compared to 1.5T and 3T, respectively [103, 121, 176].

RF-receiver coils can be formed over the needle surface using insulated copper wire but these cause irregularities in needle profile that may impair mechanical performance, risk bystander tissue damage or shearing of integrated components during clinical use. Standard circuit components used in RF coil/antenna designs are also rigid and bulky compromising the overall device profile and mechanical properties [177]. All such characteristics are excessively rigid and impair device miniaturization; indeed, currently there is no commercially available active MRI needle device. Recently, micro-electro-mechanical systems (MEMS) fabrication techniques including 3D laser lithography [88,178], aerosol deposition [179,180], hot embossing [181], deposition by thermal evaporation [169], wrapping flexible circuit sheets [182] and focused beam sputtering [183] have been used to build RF receiver antenna components as thin-film structures predominantly on planar surfaces. These methods may require detailed preparations and/or a high maintenance infrastructure such as a cleanroom. In addition, these techniques have limited ability to fabricate non-planar multi-layer circuits [184] and their in-vivo performance on non-planar metal surfaces hasn't been

evaluated.

As an alternative, we propose to incorporate the required RF-antenna components directly onto the non-planar needle surface using conductive ink and flexible materials to satisfy user electrical and mechanical requirements during clinical use. We introduce a novel technique to precisely print thin-film RF antenna structures onto MRI compatible intravascular devices using conductive ink and biocompatible polymer tubing. Medical grade devices require the use of biocompatible materials for device fabrication and their safety and efficacy need to be confirmed through appropriate clinical trials and regulatory approvals for direct clinical use [185, 186] We tested the performance and medical grade device manufacturing capabilities of the proposed method by fabricating a 20 Gauge (Outer Diameter [OD] = 0.87 mm) active needle designed to accomplish needle access to superficial and deep blood vessels and organs during iMRI procedures at 0.55T.

3.2 Methods

A conductive ink printing system was built for small diameter active iMRI device fabrication. A series of electro-magnetic simulations were run to determine optimal setpoints for the device RF antenna geometry. Active iMRI needle prototypes with a printed RF antenna were built based on the simulation results. In-vitro and in-vivo MRI visibility and in-vitro RF-induced heating performance of the prototypes were tested and compared to a typical active iMRI needle built using manually wound insulated copper wire RF antenna at 0.55T.

3.2.1 Conductive ink printing system design and characterization tests

We designed and built a custom, computer-numeric-control (CNC) based four-axis electromechanical system featuring an automated ink dispenser to print RF antenna components on non-planar interventional medical device surfaces using conduc-

tive ink. Housing of the ink dispenser unit was designed using a computer aided design software (Solidworks, Dassault Systems, MA, USA) and manufactured using a 3D Printer (S5, Ultimaker, Netherlands). A hybrid stepper linear actuator (Ametek, CT, USA) was used as the plunger of the ink dispenser. 3cc Luer-lock disposable syringes with 32 G disposable needle tips (Fishman Corp, MA, USA) were used to contain and inject the conductive ink. A hybrid stepper linear actuator (Ametek, CT, USA) was modified by adding a Luer-lock apparatus at the actuator rod end and used as the plunger actuator. A disposable inline blood pressure sensor (Deltran, Utah Medical, UT, USA) was integrated to the syringe outlet to monitor the conductive ink pressure. Precise control of conductive ink flow was secured implementing a closed-loop proportional-integral-derivative (PID) control (Figure 3.1). The material flow was controlled with a pressure driven flow control model [187] using Eq. 3.1.

$$\Delta P = \frac{128 \mu V l}{\pi d^4} \tag{3.1}$$

where P is the pressure (Pa), μ is the viscosity (Pa·s), V is the flow velocity (m/s), l is the channel length (m) and d is the hydraulic diameter (m).

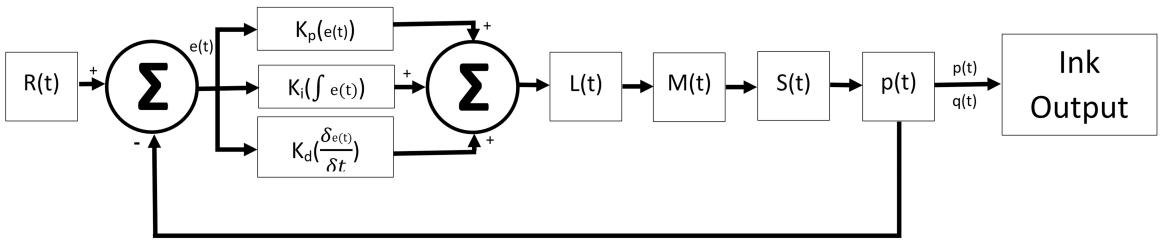


Figure 3.1 Closed-loop Proportional-Integral-Derivative (PID) control diagram of the ink dispenser unit where R(t) is the target pressure value (reference), e(t) is the calculated error between the reference value and the actual pressure, Kp is the proportional coefficient, Ki is the integral coefficient, Kd is the derivative coefficient, L(t) is the linear position of the actuator, M(t) is the linear to angular position conversion, S(t) is the step calculation and the p(t) is the actual pressure value from the sensor and q(t) is the calculated material flow.

PID controller measures the actual output pressure value and aims to direct the system towards the target pressure output by calculating the error between the actual and target pressure values. The proportional stage amplifies the error with a constant

(K_p). The integral stage cumulatively adds the error during the control cycle and multiplies the result with a constant (K_i). The derivative stage monitors the change in error between the beginning and end of the control cycle and multiplies the result with the a constant (K_d). Next, the linear displacement of the plunger rod required for the pressure adjustment is calculated [L(t)] and converted to an angular value [M(t)]. Finally, the calculated angular value is converted to number of steps [S(t)] required to move the stepper linear actuator yielding the pressure output to reach the target value.

The disposable pressure sensor was calibrated using a certified pressure sensor calibration device (Delta-Cal, Utah Medical, UT, USA). A micro-controller unit (UnoR3, Arduino, MA, USA) was used to implement closed-loop PID control of the material flow [188] for high precision printing (Figure 3.2). Finally, the automated ink dispenser unit was mounted onto the Z axis of the motion control system (Figure 3.3).

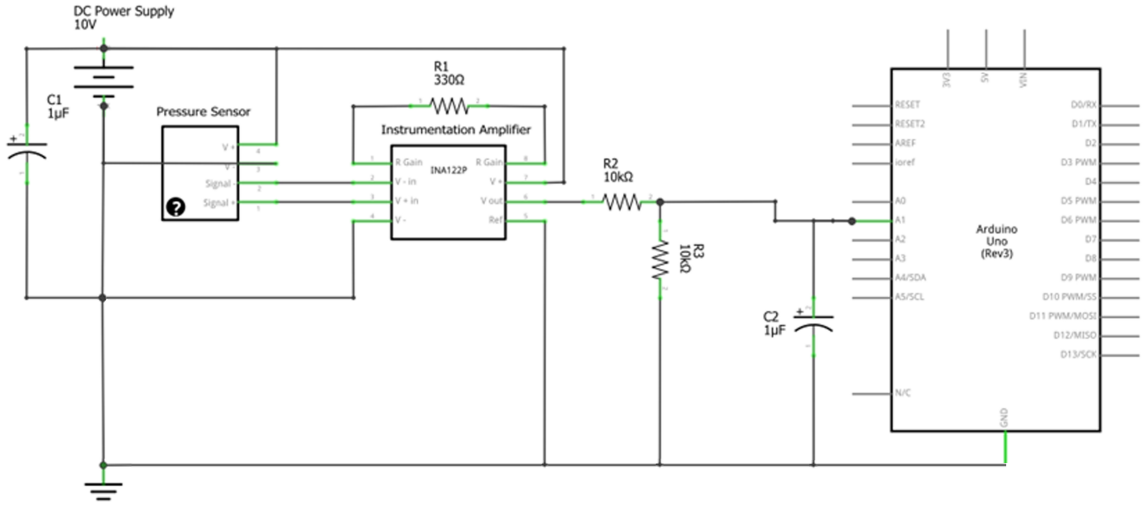


Figure 3.2 Electronic schematic of the closed-loop PID control circuit consisting of a disposable inline blood pressure sensor, a low-noise amplifier and a microcontroller.

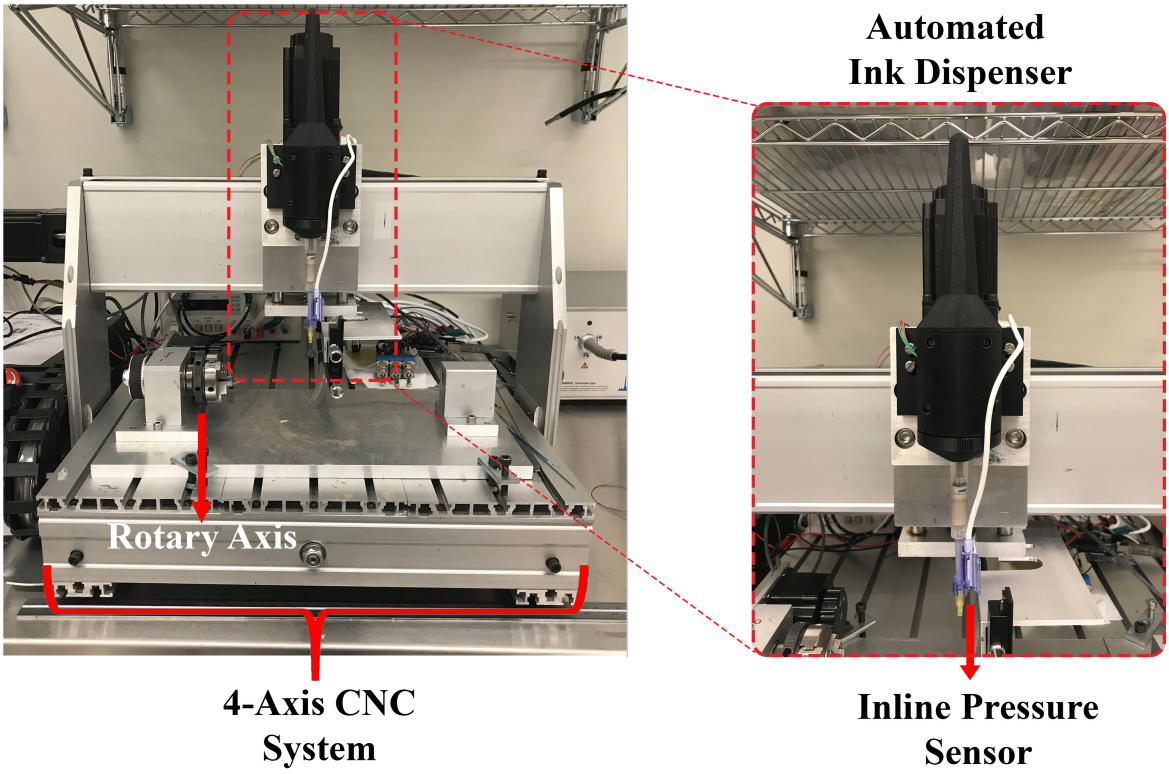


Figure 3.3 CNC-based four axis conductive ink printing system with a rotary axis for non-planar fabrication. The 3D printed automated conductive ink dispenser with the disposable inline pressure sensor is mounted on the Z axis.

The dispenser unit control accuracy was tested applying arbitrary reference values including a step, a fast changing and a programable profile to the PID input. PID control response to the reference values was recorded to calculate the response time and the error margin of the dispenser unit. The mechanical accuracy of the electromechanical system was tested by printing circumferential straight lines with 1, 3, 5 and 10 mm separations onto a 5 Fr Pebax hypotube (Nordson Medical, MA, USA). The ink deposition rate was kept constant to print identical lines during the test. The distances between straight lines were measured with an optical microscope (SOL, MicroVu, CA, USA). The optical microscope was calibrated for the measurement focal distance using the vendor provided certified calibration slide. Measurements were performed on triplicate samples. Additionally, adjustable ink flow and fine printing capabilities of the system was tested by printing fine lines with adjusted line thickness on biocompatible heat shrink polyester hypotube.

3.2.2 MRI compatible active needle design and characterization tests

Design specifications of the active needle prototype were determined for clinical use by the interventional cardiologists in our group. The final prototype was expected to have 20 G (0.87 mm) OD and 90 mm usable length. The needle ID requires to be compatible with 0.014" (0.36 mm) guidewires. Whole device visibility provided by a single loop coil [75] without distinct markers may result in the misconception of device tip location when the distal portion of the device is off the imaging plane [37, 70]. Thus, three distinct markers with 30mm spacing were required for accurate estimation of the tip location and penetration depth. Solenoid coil geometry was implemented to concentrate the forward polarization RF-magnetic field (B_1^+) around the markers and provide distinct marker visibility. Individual marker length was limited to between 2 mm and 4 mm to minimize anatomical data obscured by the marker artifact.

3.2.2.1 Electromagnetic field simulations. By the reciprocity principle, B_1^+ can be used to predict the receive sensitivity and the near-field SNR of a RF antenna [189]. Finite difference time domain (FDTD) simulations were performed to calculate the B_1^+ distribution and visualize magnetic (B) field vectors to optimize coil parameters and desired antenna geometry. Sim4Life 6.2 (Zurich MedTech AG, Switzerland) electro-magnetic simulation software was used.

Solenoid coil behavior in the presence of a metal conductor such as a metal needle body in the solenoid axis is well examined in the literature [108]. Briefly, solenoid pitch is one of the factors affecting a coil's coupling efficiency with the surrounding B field [133]. In the case of a metallic needle having an integrated RF-receiver antenna, the induced common mode currents on the metallic needle body generate a transverse B field which is perpendicular to the longitudinal axis of the solenoid. The solenoid portions of the antenna can couple to this field if the solenoid pitch is sufficiently loose, which might cause the RF-induced temperature to decrease or increase, depending on the solenoid pitch and length, and the distance between solenoids [108]. We aimed to minimize this coupling for distinct marker visibility.

A 3D model of the active needle prototype consisting of three solenoid coils connected by straight conductors (Figure 3.4A) was prepared adhering to the actual component dimensions (Figure 3.4B).

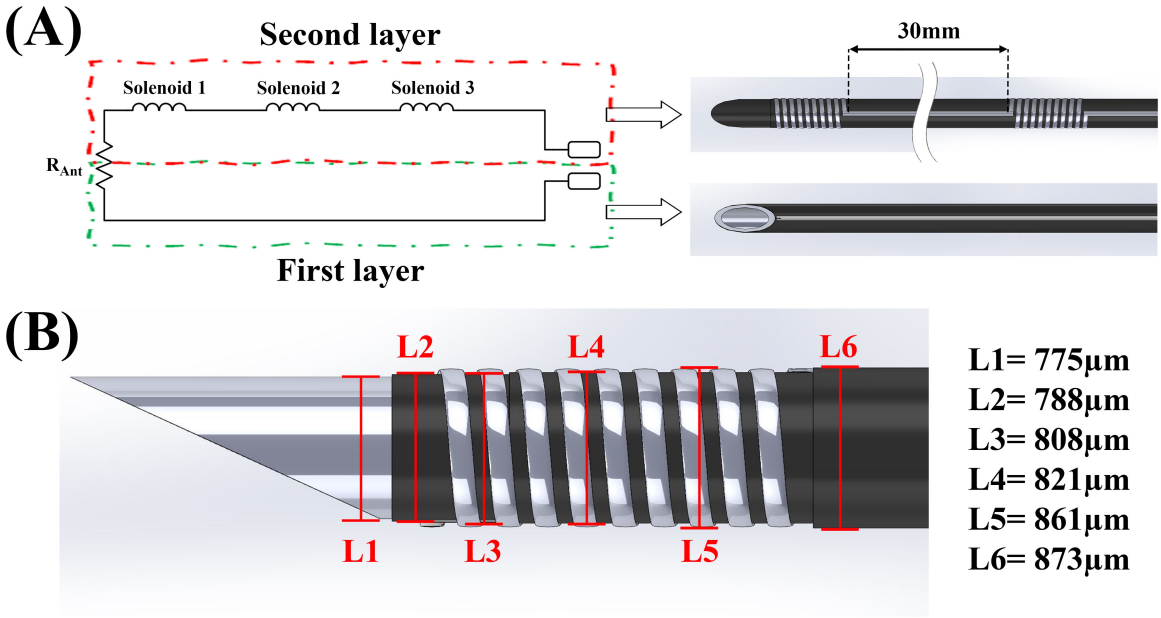


Figure 3.4 (A) Simplified schematic representation of the active needle RF antenna and corresponding printed polymer layers (parasitic capacitance of the solenoid coils and the transmission line is ignored). (B) 3D drawing of the active needle prototype used for the electro-magnetic simulations, showing the individual component dimensions. Polymer layers are retracted on the drawing to expose the normally encapsulated components. (L1 is the OD of the nitinol hypotube. L2 is the OD after the first layer polyester tube only, L3 is the OD after conductive ink printing on the first layer polyester tube. L4 is the OD after the second layer polyester tube only, L5 is the OD after conductive in printing on the second layer polyester tube. L6 is the final OD of the active needle.).

5 µm isotropic voxel size was used to accurately discretize the thin-film RF antenna and polyester tubing (Figure 3.5). The needle and printed RF antenna materials were defined as resistive conductors with 80 Ω/m and 50 Ω/m impedance at 23.66 MHz, respectively. Active needle models were partially immersed in a gel phantom with electrical conductivity of 0.47 S/m and relative permittivity of 80. The birdcage coil used for RF excitation in clinical MRI scanners was excluded for computational simplicity. The printed RF antenna was excited at the proximal end to exploit the reciprocity principle. Active needle models were simulated first parallel and then perpendicular to B_0 to evaluate the orientation dependence of the RF antenna performance. 10 turn

solenoids previously provided sufficient inductance (35 nH) [190] to produce distinctly visible markers [190]. The number of solenoid turns was kept as 10 to limit the number of optimization parameters. First, incremental lengths (2 mm, 2.5 mm 3 mm and 4 mm) of a 10 turn solenoid coil were tested. Next, effects of the conductor thickness and normalized pitch ("p", the ratio of the distance between the adjacent turns divided by the conductor diameter) [108] were assessed. Only 20 µm and 50 µm were tested as the conductor thickness because they represent the target printed conductive ink thickness and insulated copper wire diameter used to build a comparator needle, respectively. Effects of the electrical conductivity were not investigated via simulations. The B_1^+ magnitude alongside the needle was calculated on a straight line 1mm away and parallel to the needle.

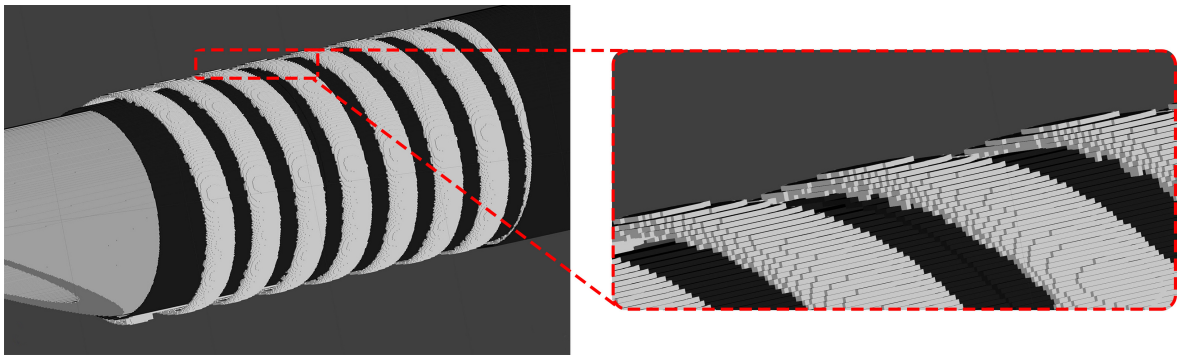


Figure 3.5 Discretized 3D model of the active needle prototype using 5 µm voxel size.

3.2.2.2 MRI Compatible Active Needle Design. An MRI compatible nitinol hypotube (Memry Corp, CT, USA) with 0.610 ± 0.025mm ID and 0.775 ± 0.025 mm OD was cut to 10 cm length and the distal tip of the tube was shaped as a sharp needle using a laser cutter (LASAG, Bern, Switzerland). A loop RF antenna was printed on biocompatible heat-shrink polyester tubing with 1.067 mm expanded ID and 6.35 µm wall thickness (103-0154, Nordson Medical, MA, USA) as two coaxial layers using silver conductive ink (AG-510, Kayaku Advanced Materials, MA, USA). An alternating current tends to travel at the outer most part of a cylindrical conductor due to the "Skin Effect". The "Skin Depth" which is the AC current carrying portion

of the conductor's cross section can be calculated using Eq 3.2 [191].

$$\delta = \sqrt{\frac{\rho}{\pi f \mu_r \mu_o}} \tag{3.2}$$

where δ is the skin depth (m), ρ is the resistivity of the material (ohm/m), f is the frequency (Hz), μ_r is the relative permeability and μ_o is the permeability constant.

The skin depth for the silver conductive ink at 23.66 MHz can be calculated as 16.9 µm. 20 µm conductor thickness was targeted to eliminate the skin effect. The first layer polyester tube contained only a straight line (Figure 3.6A) while the second layer had three solenoid coils 30 mm apart but connected with straight lines in series (Figure 3.6B). According to simulation results, 2 mm long solenoid coils would provide the highest peak-to-peak marker SNR. However, 2.5 mm long, 10 turns solenoid coils were preferred since 32 G (240 µm OD) needle tips were used as the ink outlet. 150 µm conductor width (p=0.67) was targeted to minimize the transverse magnetic field coupling. The printed coil and conductor dimensions were measured using an optical microscope (SOL, MicroVu, CA, USA). The conductive ink printed polyester heat-shrink tubing was placed onto the nitinol needle body and heat-shrunk at 135 °C using a hot air station (210-A, BEAHM Design Inc., CA, USA). The coaxial polyester printed layers were electrically connected at the distal end using the silver conductive ink to complete the antenna circuit. 1mm long electrical connectors were formed from a nitinol hypotube with 0.864 ± 0.025 mm ID and 0.965 ± 0.025 mm OD (Memry Corp, CT, USA) via laser cutting and soldered to a 36 AWG micro-coaxial cable (9436-WH033, Alpha Wire, NJ, USA). A silver epoxy (8331S, MG Chemicals, Ontario, Canada) was applied to the inner lumen of the hypotube pieces and connected to the proximal ends of the printed RF antenna. The same polyester tube was applied over the second layer to completely insulate the printed antenna (Figure 3.6E). A custom Luer-lock hub was 3D printed and assembled on the active needle prototypes to connect with standard syringes (Figure 3.6F). The total DC resistance of the printed antenna was measured before and after the heat treatment, using a vendor calibrated multi-meter (117, Fluke, WA, USA).

For a higher quality comparison, another active needle prototype with a nearly identical design incorporating a manually-wound RF antenna was built using a 44 AWG enamel coated copper wire (79748#039, Remington Industries, IL, USA) and the same nitinol hypotube (0.775 µm OD).Since the enamel coating on the copper wire is very thin, the heat-shrink polyester tube was applied onto the nitinol needle body first, then the copper wire wound antenna was integrated onto the polyester layer to minimize coupling with the metal needle body.

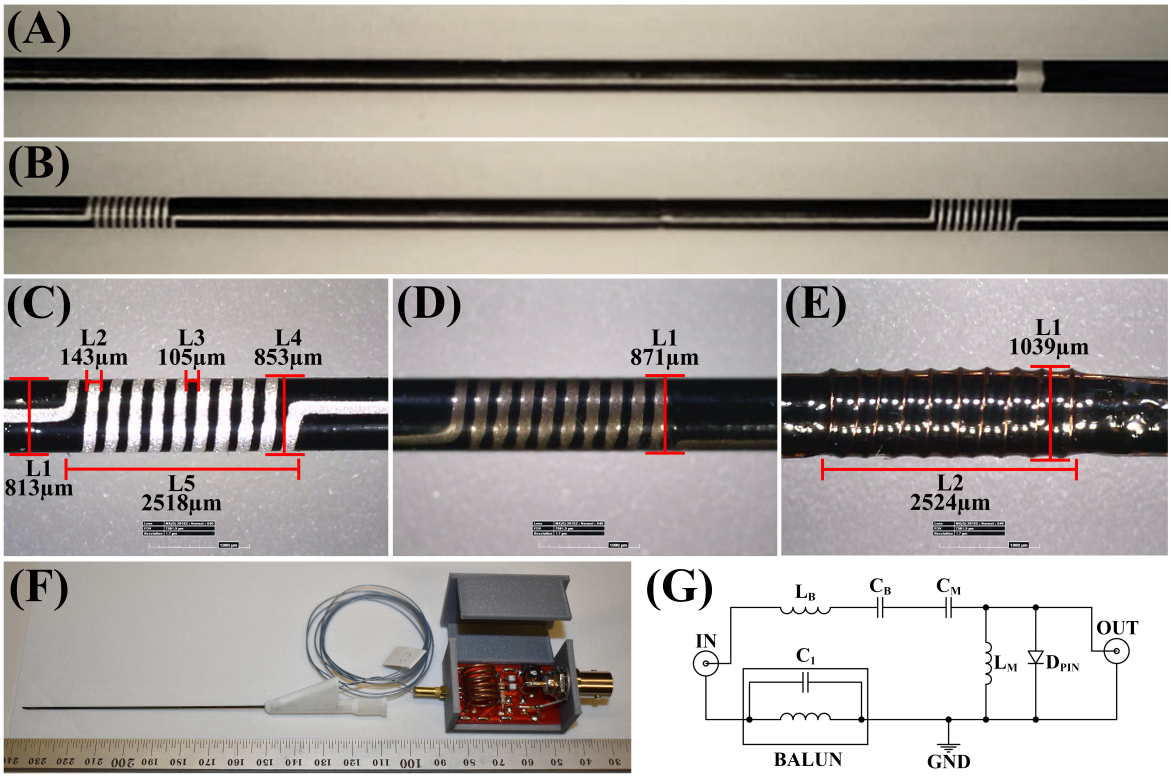


Figure 3.6 (A) The first layer conductive ink printed polyester tube consisting only a straight line and (B) the second layer conductive ink printed polyester tube with solenoid coils of the RF antenna connected with straight lines. (C) Optical microscope measurements of the printed solenoid coils (L1 is the needle diameter after the second polyester layer, L2 is the printed conductor width, L3 is the distance between the adjacent windings, L4 is the needle diameter after the second printed layer and L5 is the solenoid coil length). Final profile measurements of the active needle prototypes (D) with the printed RF antenna and (E) with the insulated copper wire wound RF antenna. L1 is the final needle OD and L2 is the solenoid coil length. (F) The final assembly of the active needle prototype with the custom Luer-lock hub, micro coaxial cable and the tune and match circuit. (G) Tune and match circuit diagram of the RF antennas. (A)-(D) belong to the active needle prototype with the conductive ink printed antenna. (E) belongs to the active needle prototype with the 44 AWG insulated copper wire antenna.

The heat-shrink polyester tube was applied onto the copper wire antenna to mimic the printed RF antenna construction (Figure 3.6E). The proximal ends of the insulated copper wire RF-receiver antenna were soldered directly to the 36 AWG micro-coax cable. Active needle prototypes were tuned to 23.66 MHz and matched to 50Ω remotely at the proximal end of the micro-coax cable using a vector network analyzer (VNA) (4395a, Agilent, CA, USA). A choke BALUN was used to eliminate the shield common mode currents. A serial capacitor and a parallel inductor were used for impedance matching. A PIN diode was used to minimize coupling between the needle RF antenna and the scanner RF-transmit coils during RF excitation to minimize RF-induced heating (Figure 3.6G). The micro-coax cable was shortened until a 90° phase difference ($\lambda/4$), at 23.66 MHz, between the PIN diode and the RF antenna was obtained so that the low impedance, when the PIN diode is activated, can be translated as a high impedance at the RF antenna end.

3.2.2.3 In-vitro characterization tests. The mechanical performance of the active needle prototype was evaluated via bending and puncture tests per ASTM F1874 [192] and ASTM F2132 [193], respectively. Results were compared to commercially available 20 G puncture needles including a non-MRI compatible stainless steel needle (BD Spinal Needle, Becton, Dickinson and Company, NJ, USA), and MRI conditional titanium (Philips Invivo, Germany) and Inconel needles (MReye Chiba, Cook Medical, IN, USA). A custom fixture apparatus was 3D printed to hold the needle under test steady during bending tests. A digital force meter (ZP-11, Imada Inc., IL, USA) was attached onto an automated linear actuator (MH2, Imada Inc., IL, USA) to measure the applied force. The needle under test was extended 40 mm from the fixture apparatus and fixed. Perpendicular bending force was applied at a point 20 mm apart from the needle tip (Figure 3.7A). The digital force meter was advanced at 2 mm/sec to push the needle under test for 10 mm and retracted at the same speed.

Same test setup was used for the puncture test with small modifications. The fixture apparatus was used to fix a tissue simulating porous polymer block and the needle under test was securely attached to the digital force meter using a Luer-lock

connector (Figure 3.7B). The needle under test punctured the polymer block and was advanced at 3mm/sec for 21mm, then it was retracted at 6mm/sec. The polymer block was renewed before each puncture. Both tests were repeated three times per needle.

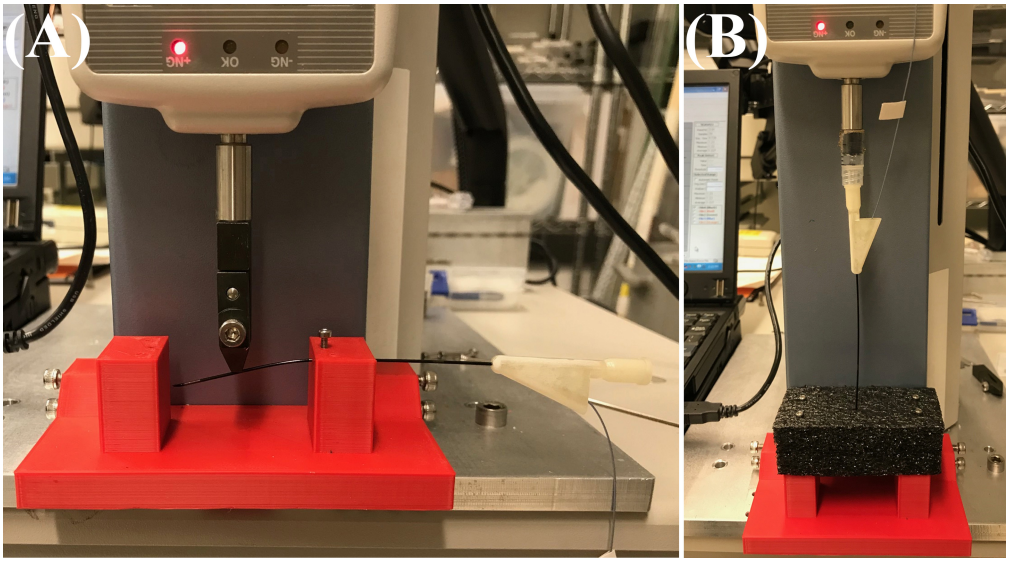


Figure 3.7 Mechanical test setup for (A) the bending and (B) puncture tests. Same setup was used for both tests with small modifications.

A real-time bSSFP pulse sequence (TE/TR:1.05/2.50ms, FA:45°/60°/75°, FoV: 320x320 mm, bandwidth: 1042 Hz/Px, matrix: 192x144, ST:6 mm, 3 fps), typically used for clinical MRI catheterization at 0.55T at our institution, was used during the in-vitro tests. The bSSFP sequence is prevalent in iMRI due to favorable image contrast and image acquisition speed. Due to the high specific absorption rate (SAR) brought about by the short TR/high flip angle combination, bSSFP presents an appropriate upper limit in SAR for the active iMRI devices [4, 194]. In-vitro RF-induced heating and imaging performance of the active needle prototypes were tested using a high-performance low-field scanner at 0.55T (prototype MAGNETOM Aera, Siemens Healthcare, Erlangen, Germany).

The RF-induced heating performance of the active needle prototypes was tested in a gel phantom per ASTM 2182-19 [125]. The active needle prototypes were immersed in the middle of the gel phantom, 45° oblique to Z axis, parallel to B_0 and 2 cm away from the right edge of the phantom where the SAR is maximum (determined

via previous experiments) [121] and the heat dissipation is minimum. Scans were performed in the "First Level" SAR mode (max. 4W/kg) and the reported whole body SAR value was 2.78 W/kg, 3.56 W/kg and 3.96 W/kg for 45°, 65° and 75° FAs, respectively. Temperature measurements were performed using fiber optic temperature sensors (OPT M-170, OpSens, Canada). Temperature probes were attached to the needle body using polyamide hypotubes with 80 µm ID and 90 µm OD (214-1584, Nordson Medical, MA, USA), and 3 mm long heat-shrink polymers as described before [195]. First, the location of the "hot spot" was confirmed by gradually withdrawing the temperature probe lengthwise "profiling" the temperature rise alongside the needle prototypes. Next, heating measurements were performed at the hot spot. The baseline temperature was recorded for 30 seconds before each scan, then needle prototypes were scanned for 90 seconds which represents the starting point of the plateau after the clinically significant temperature rise. The coupling efficiency of two loop coils increases with the decreasing distance between coils and maximizes when they are parallel [105]. The test was repeated by placing the active needle prototypes in the same location but perpendicular to the B_0 to increase the coupling between needle solenoid coils and the RF transmit system of the scanner. Increased coupling was confirmed via heating measurements. Additional in-vitro two-port VNA measurements or induced current measurements were not performed. Temperature profiling was repeated for each needle and orientation. Finally, the active needle prototypes were scanned with 75° flip angle for 15 minutes, perpendicular to the B_0 to simulate a challenging, uninterrupted, long MRI scan.

The in-vitro MRI visibility performance of the active needle prototypes was tested using the same real-time bSSFP sequence but with only 45° flip angle in the ASTM gel phantom. First, the prototypes were scanned at isocenter, 45° oblique to Z axis and parallel to the B_0. Then, the prototypes were rotated perpendicular to the B_0 in the same location and scans were repeated. Still MR images were reconstructed using only the active channel signal received from the active needle prototypes and all other imaging coils were deactivated. The SNR maps of the in-vitro MR images were calculated using the pixel SNR method [196] with N=100 using Matlab (2020a, MathWorks, MA, USA). The SNR profiles on a straight line alongside the active needle

prototypes were calculated to assess the MRI marker distinguishability. Real-time in-vitro MRI tracking performance of the active needle prototypes was tested during insertion, rotation, and an exaggerated deflection in the field of view. A prototype interactive real-time MRI interface (MonteCarlo, Siemens, Germany) was used with a real-time bSSFP sequence (TE/TR:2.0/4.0 ms, FA:45°, FoV: 320x320 mm, bandwidth: 1042 Hz/Px, matrix: 192x144, ST:8 mm, 3 fps). A four-element spine coil was used for phantom imaging. The active channel signal was colorized on the MR image [73] after scaling with window level/window width = 16/16. Both prototypes were scanned with the same RF receiver gain for the active channel signal. A custom, 3D printed sliding and rotating needle holder was used during tests (Figure 3.8).

3.2.2.4 In-vivo characterization tests. The real-time in-vivo MRI visibility performance of the active needle prototypes was tested in one swine under general anesthesia by advancing the active needle prototypes into the liver. Animal experiments were approved by the National Heart, Lung and Blood Institute (NHLBI) Animal Use and Care Committee and performed according to the contemporary National Institutes of Health (NIH) standards. Non-sterile prototypes were tested as an "add-on" experiment to another non-survival porcine experiment to minimize use of animals. All used general anesthesia and mechanical ventilation.

MonteCarlo interactive real-time MRI interface software was used with the same real-time bSSFP sequence used for real-time in-vitro MRI. Imaging parameters were tailored for a low frame rate since the liver is a stationary organ. Only a four-element spine coil underneath the animal was used for the anatomical imaging. No surface coil was used since the tests were performed as an add-on to an open-chest cardiac experiment. The active channel signal was colorized on the MR image [73] after scaling with window level/window width = 16/16. Both prototypes were scanned with the same RF receiver gain for the active channel signal. Real-time device tracking was performed manually by adjusting imaging planes. The active marker signal drops-off rapidly away from the device antenna causing a nebulous artifact. The active needle artifact size was measured on DICOM images after isolating the active marker signal

and thresholding with cutoff pixel intensity value 5 using Matlab to calculate the size of the surrounding anatomy obscured by the marker artifact.

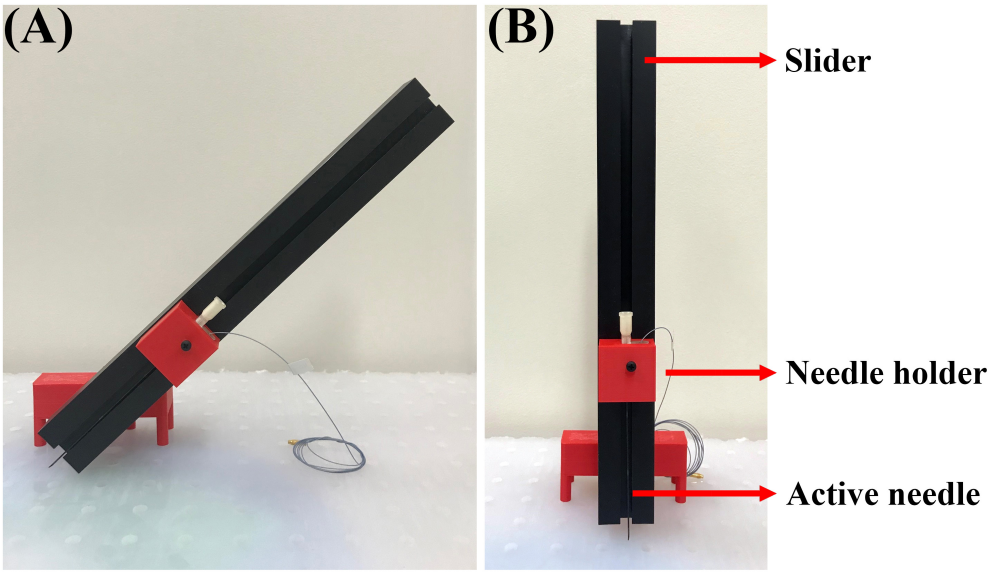


Figure 3.8 Custom, 3D printed sliding and rotating needle holder used for in-vitro real-time MRI tests. (A) 45° rotated and (B) vertically fixed. Active needle prototype is mounted on the needle holder and slid and/or rotated in the field of view.

3.3 Results

3.3.1 Conductive ink printing system characterization tests

The measured response error of the PID controller of the automated conductive ink dispenser remained under 2% for the step input, under 8% for the dynamically changing input and under 6% for the programmable input (Figure 3.9A). The average response time of the PID controller was measured less than 250 ms (Figure 3.9A). The accuracy of the PID controller was also confirmed visually with the consistency of the printed line dimensions during the electromechanical system accuracy tests and active needle manufacturing. The optical microscope measurements of the printed RF antenna components demonstrating the mechanical accuracy of the electromechanical system and the control accuracy of the ink dispenser unit are shown in Figure 3.9B. The overall system precision provided a fine printing resolution (<4 µm). Closed-loop

PID control of the ink flow allowed on-the-fly adjustment of the printed line width (Figure 3.9C).

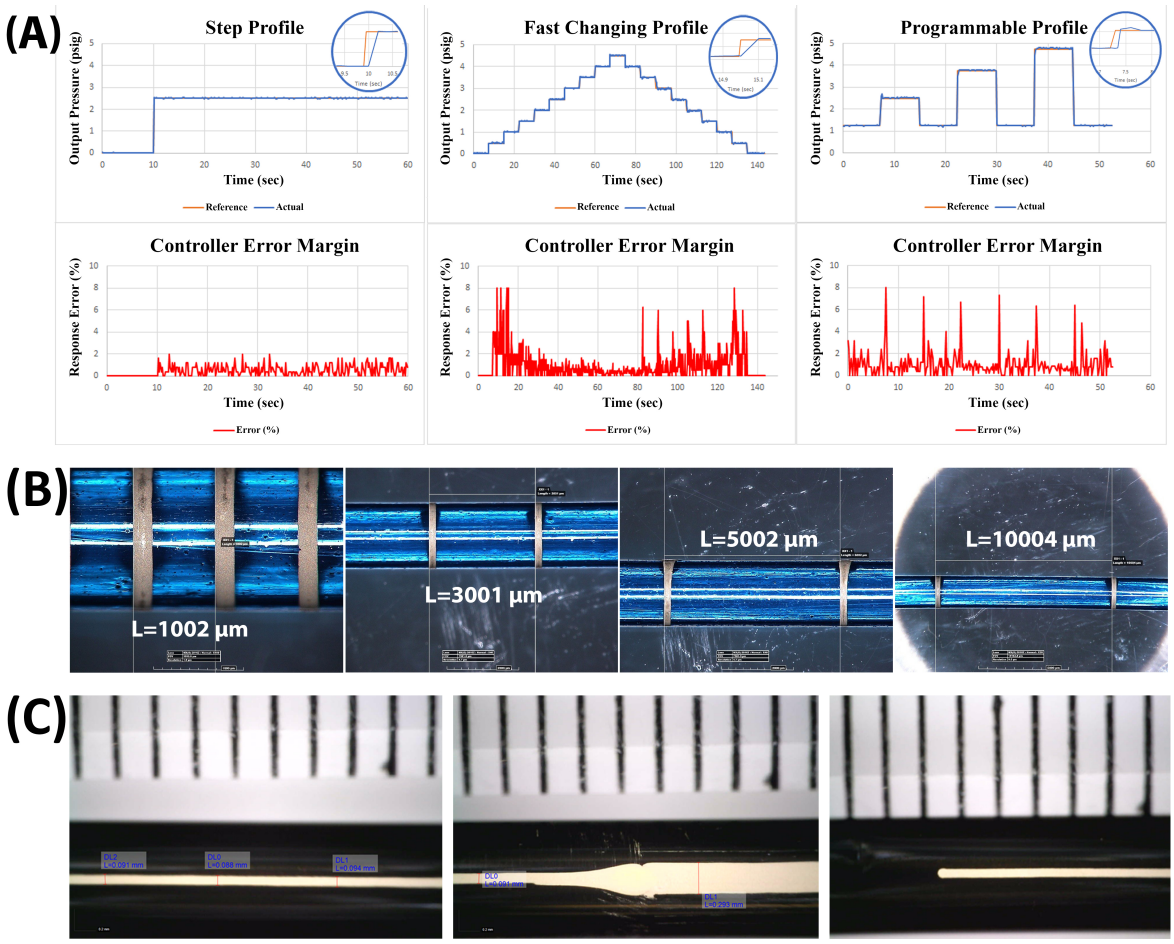


Figure 3.9 (A) PID controller response to the reference inputs including a step profile, a fast changing profile and a programmable profile with the corresponding controller error margins showing the ink dispenser unit control accuracy test. (B) Circumferential straight lines printed on a 5Fr Pebax hypotube with 1mm, 3mm, 5mm and 10mm separations for the mechanical accuracy test of the electromechanical system. (C) Fine printed lines with 100 µm and 300 µm line width. Line width can be changed on-the-fly. PID control eliminates residual ink globs at the needle tip.

3.3.2 Electromagnetic field simulations

Figure 3.10 and 3.11 show the electro-magnetic simulation results of the active needle designs with 2 mm, 2.5 mm, 3 mm and 4 mm long, 10 turns solenoid coils placed 30 mm apart as MRI markers. B_1^+ distributions show that the antenna sensitivity can be concentrated around the solenoid coils (Figure 3.10A).

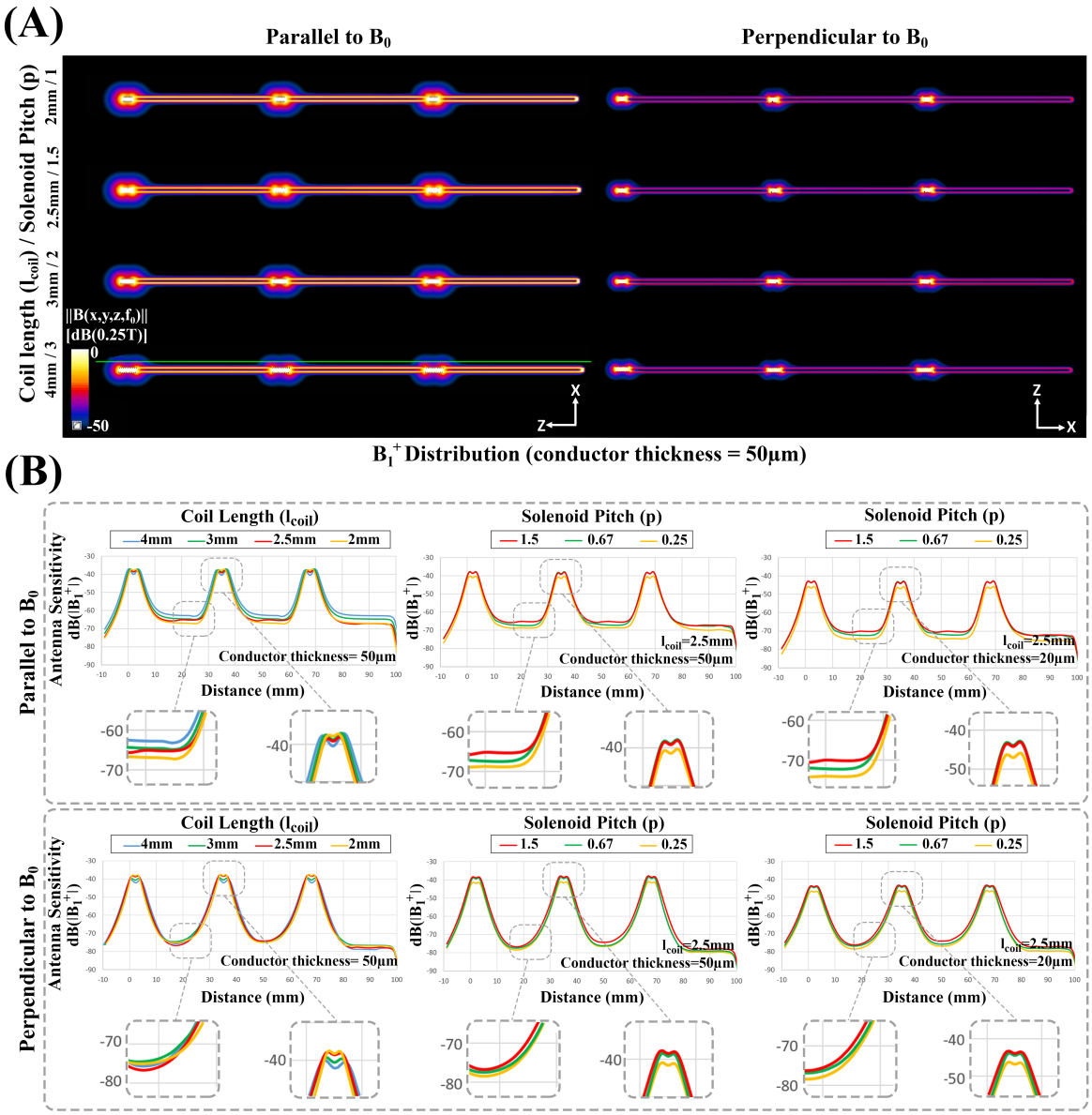


Figure 3.10 Electro-magnetic simulation results of the active needle design. (A) B_1^+ distribution of the desired antenna geometry with 10 turns solenoid coils. (B) The B_1^+ magnitude alongside the active needle design showing the effects of the solenoid coil length, conductor thickness, normalized pitch (the ratio of the distance between the adjacent turns divided by the conductor diameter) and needle orientation with respect to B_0. B_1^+ profiles were extracted on the green line parallel to active needle models.

Figure 3.10B shows B_1^+ magnitude profiles alongside the active needle designs. RF antenna sensitivity changes with the conductor thickness, solenoid length and pitch, and needle orientation with respect to B_0. Figure 3.11 shows B field vectors along and

among the coil windings. Non-zero transverse B field (rotated field vectors from the longitudinal axis around the windings) presents when the coil pitch is sufficiently loose. Transverse B field approaches zero if the coil pitch is sufficiently small because of the cancellation between the coil windings. According to simulation results, 2.5 mm long solenoid coils with p=0.67 provide sufficiently distinguishable marker visibility and minimize the coupling with transverse B field.

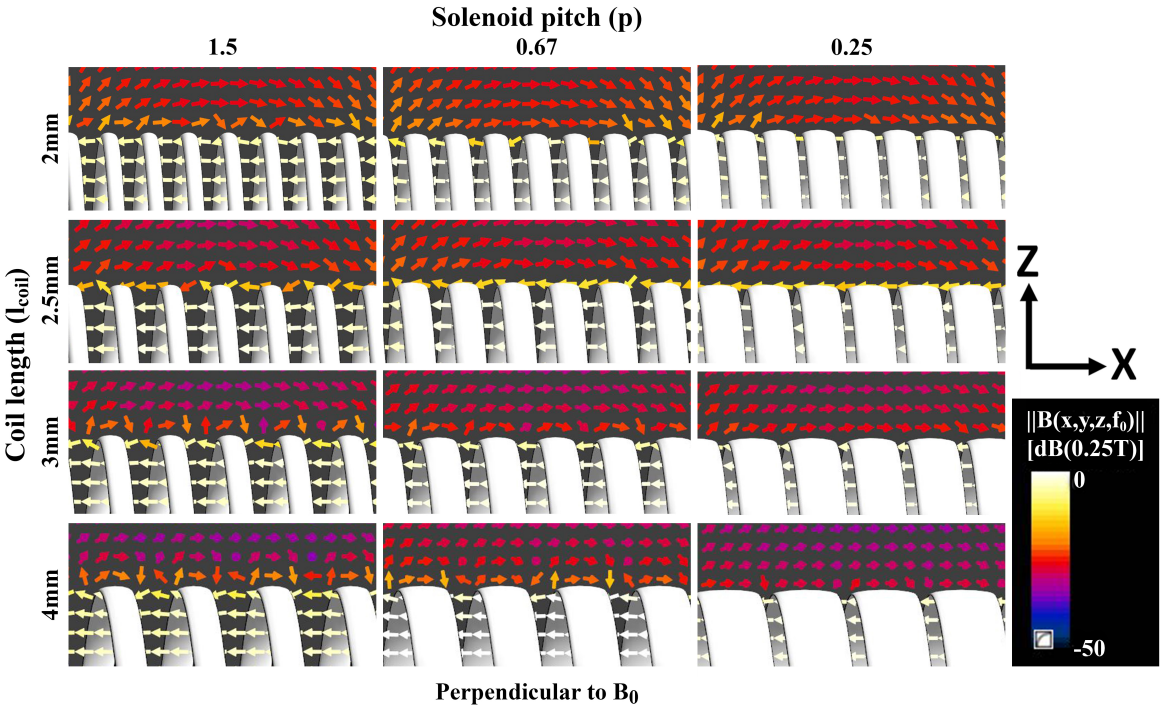


Figure 3.11 Magnetic field (B) vectors around the windings of 2 mm, 2.5 mm, 3 mm and 4 mm long, 10 turns solenoid coils with 1.5, 0.67 and 0.25 normalized pitch as the needle is oriented perpendicular to B_0. Rotated vectors from the longitudinal axis around the windings indicate the presence of transverse magnetic field (B_{Tr}) which is perpendicular to solenoid axis. 2.5 mm long solenoid coil with 0.67 normalized pitch shows sufficient marker visibility and minimizes the B_{Tr} coupling.

3.3.3 MRI compatible active needle characterization tests

The optical microscope measurements of the active needle prototypes with the printed and insulated copper wire RF antennas are shown in Figure 3.6C-E. Total printing time was 86 seconds. The conductor width and the conductor thickness of the printed RF antennas were measured as 145 ± 3.2 µm and 20 ± 1 µm, respectively

(Figure 3.6C). The final needle diameter was measured as 871 ± 1 µm (Figure 3.6D) and 1039 ±1µm (Figure 3.6E) for the active needle prototypes with the printed antenna and with the insulated copper wire antenna, respectively. The total DC resistance of the conductive ink printed RF antennas was 221.38 ± 2.57Ω before and 63.21 ± 2.54Ω after the heat treatment compared to 0.7Ω of the insulated copper wire antenna. The heat treatment increased conductivity of the conductive ink 3.5 fold. Commercially available 20G needles showed similar stiffness during the bending tests. Active needle prototype was more flexible than the commercially available comparators requiring smaller forces to deflect (Figure 3.12A). On the other hand, the active needle prototype performed as well or even better than the commercially available comparators during puncture tests (Figure 3.12B).

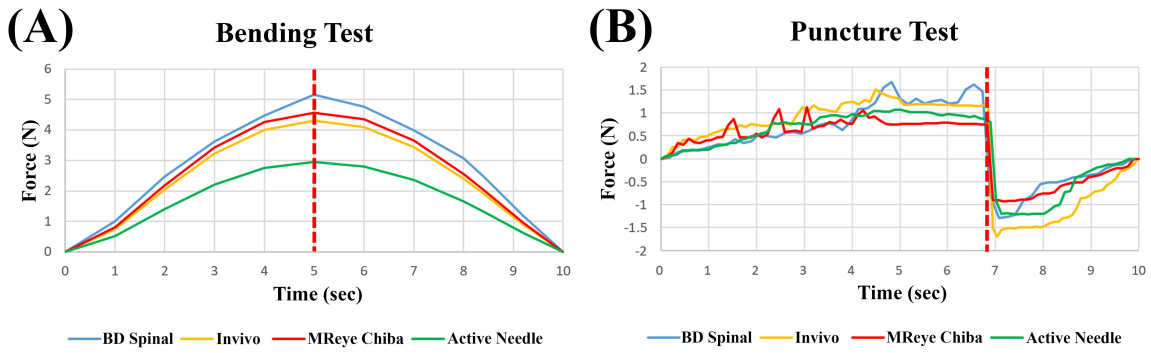


Figure 3.12 Test results of (A) the bending and (B) puncture tests. Each test was repeated three times per needle and the average of the results are plotted. The red dashed line on the graphs indicate the beginning of the retraction phase for each test.

In-vitro MR images of the active needle prototypes in the ASTM gel phantom with respect to B_0 can be seen in Figure 3.13 (all images windowed with the same window width (20), window level was not changed). The hyper-intense MRI signal picked up by the solenoid coils appears as bright spots on the images serving as MRI markers. Active needle prototypes with insulated copper wire RF antenna and with the printed RF antenna both provided distinct visibility at the marker locations. Figure 3.14 shows the in-vitro SNR maps of the active needle prototypes on the sagittal and axial planes. Each major peak on the intensity profile, plotted alongside the active

needle prototypes, represents a solenoid coil (MRI marker) location.

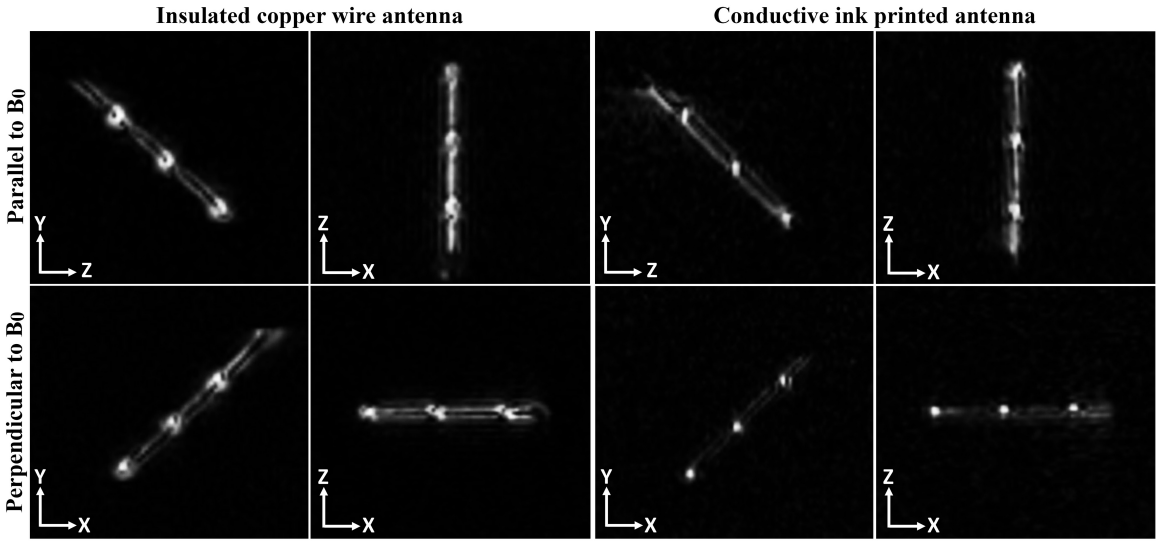


Figure 3.13 In-vitro MR images of the active needle prototypes at 0.55T using a real-time bSSFP imaging sequence. Straight conductors, connecting solenoid coils in series, couple better with the transverse magnetic field when the needle is parallel to B_0 providing a bright signal between the solenoid markers. This coupling decreases when the needle is perpendicular to B_0 providing a more distinct marker signal.

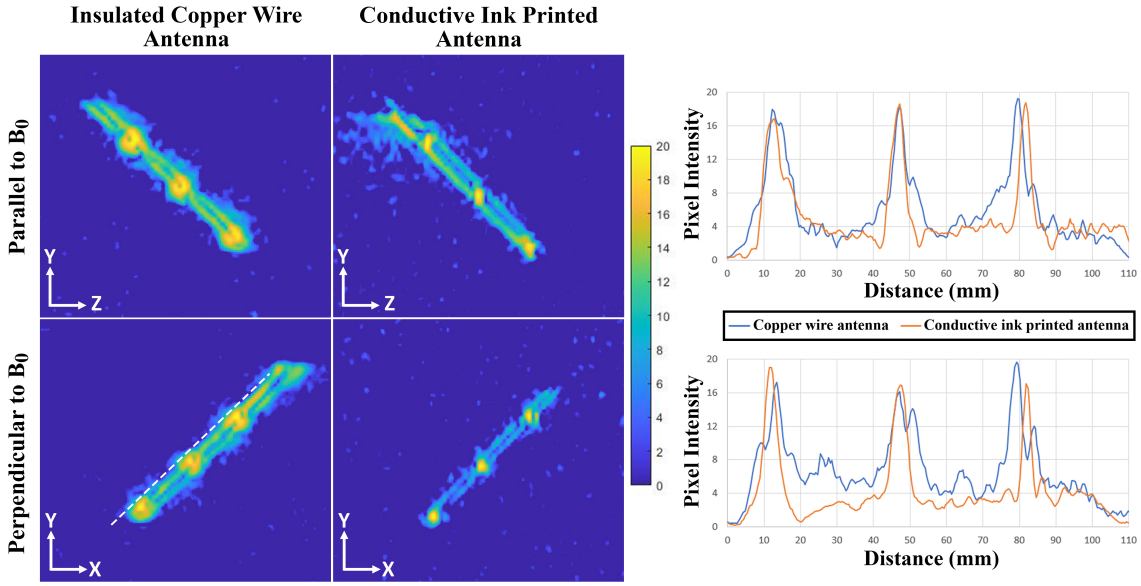


Figure 3.14 In-vitro SNR maps of the active needle prototypes on sagittal and axial planes. Pixel intensity so that the SNR profiles are calculated on a straight line 1 mm away from and parallel to the active needle prototypes (the white dashed line). The major peaks at the pixel intensity profiles represent the solenoid coil locations.

Real-time in-vitro MRI performance of active needle prototypes during insertion, rotation with respect to B_0 and an exaggerated deflection is demonstrated Figure 3.15.

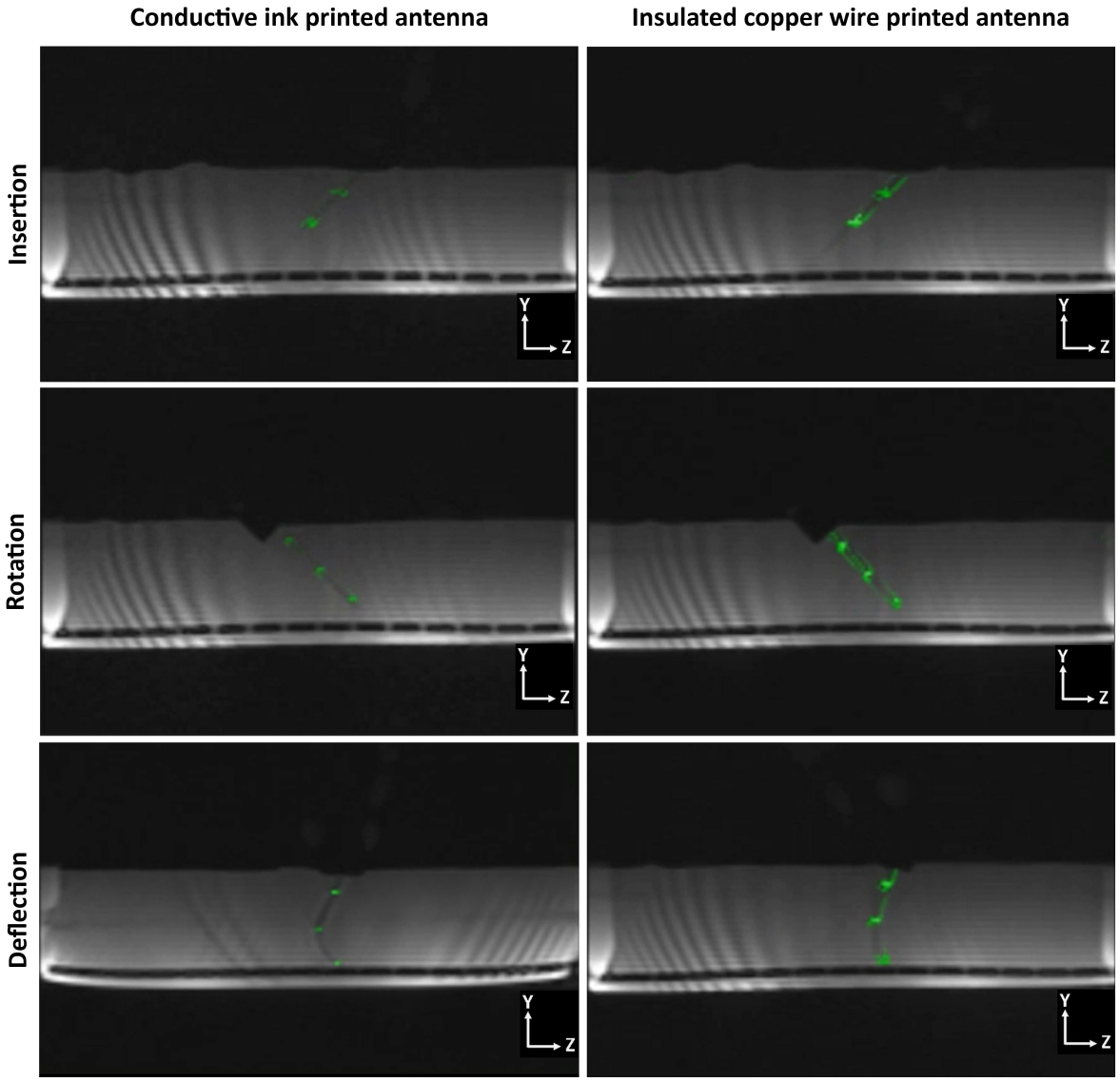


Figure 3.15 In-vitro real-time MRI of active needle prototypes during insertion, rotation with respect to B_0 and exaggerated bending in sagittal plane.

RF-induced heating test results of active needle prototypes in the gel phantom are shown in Figure 3.16. The hottest spot was at the solenoid coil placed at the distal end of the active needle prototype for both designs.

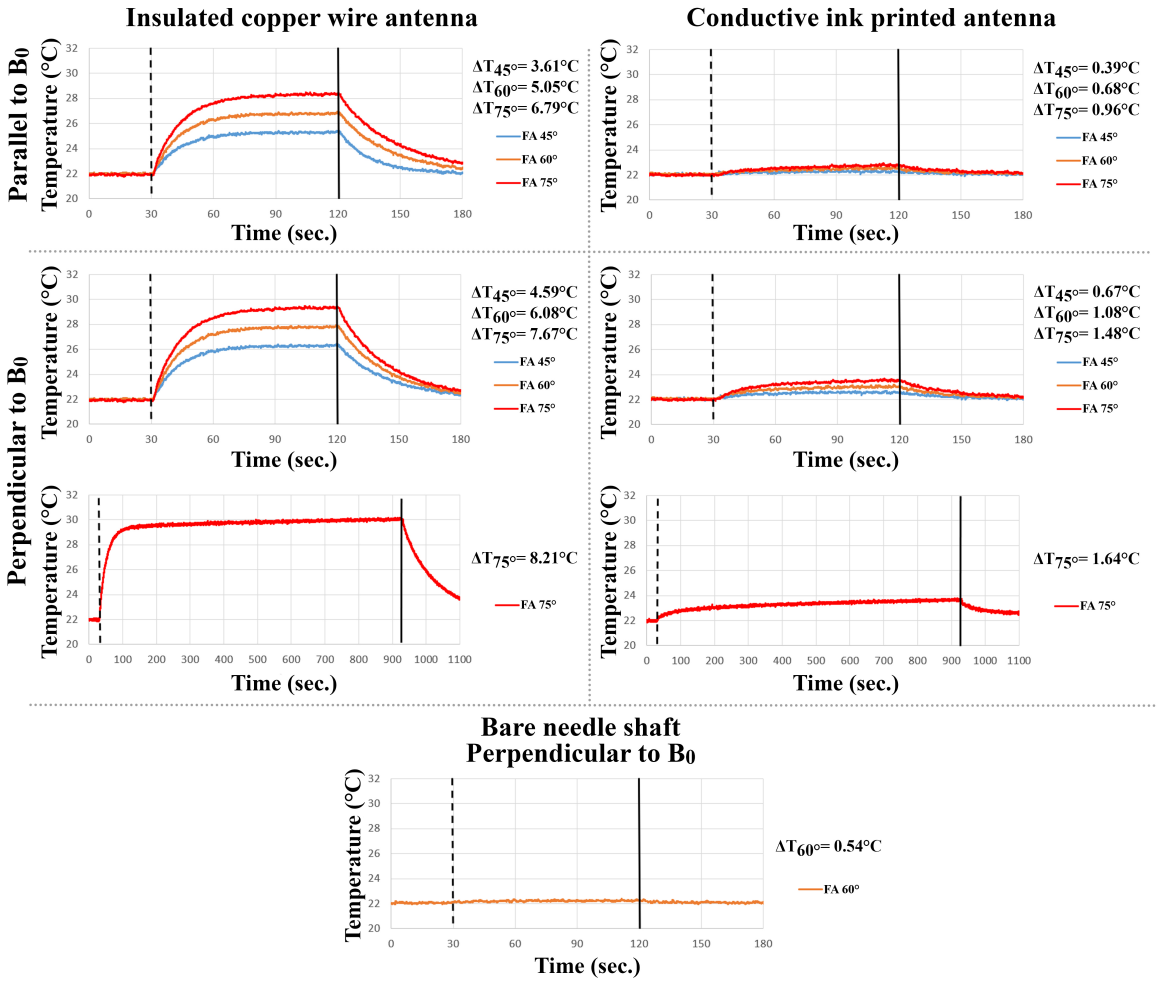


Figure 3.16 RF-induced heating test results of the active needle prototypes parallel and perpendicular to B_0 for 90 seconds and 15 minutes, and the RF-induced heating measurement of a bare nitinol needle body parallel to B_0 for 90 seconds. The dash line indicates the start of the MRI scan and the solid line indicates the stop of the MRI scan. The RF-induced heating rise of the active needle prototype with the insulated copper wire antenna exceeds clinically acceptable limits (>2°C) in every condition.

The temperature at the hot spot starts to rise right after the start of the MRI scan and saturates quickly after the first 60 seconds. The RF-induced heating rise increased with the flip angle. The temperature rise of the conductive ink printed antenna remained under 1°C when it is parallel to B_0 and under 1.5°C when it is perpendicular to B_0. The temperature rise at the end of the 15 minutes scan was 1.64°C for a 75° flip angle when the needle is perpendicular to B_0. The temperature rise of the insulated copper wire antenna was measured as 3.61°C, 5.05°C and 6.79°C

with 45°, 60° and 75° flip angles, respectively, when it is parallel to B_0. The temperature rise of the same prototype was 4.59°C, 6.08°C and 7.67°C with 45°, 60° and 75° flip angles, respectively, when it is perpendicular to B_0. The temperature rise at the end of the 15 minute scan was 8.21°C for a 75° flip angle when the comparator prototype with copper wire antenna is perpendicular to B_0. The temperature rise of the bare nitinol needle body at the needle tip (hot spot) was recorded as 0.54°C with 60° flip angle, at the end of 90 seconds when it is parallel to B_0.

The real-time in-vivo MR images of the active needle prototypes are shown on sagittal and axial planes (Figure 3.17).

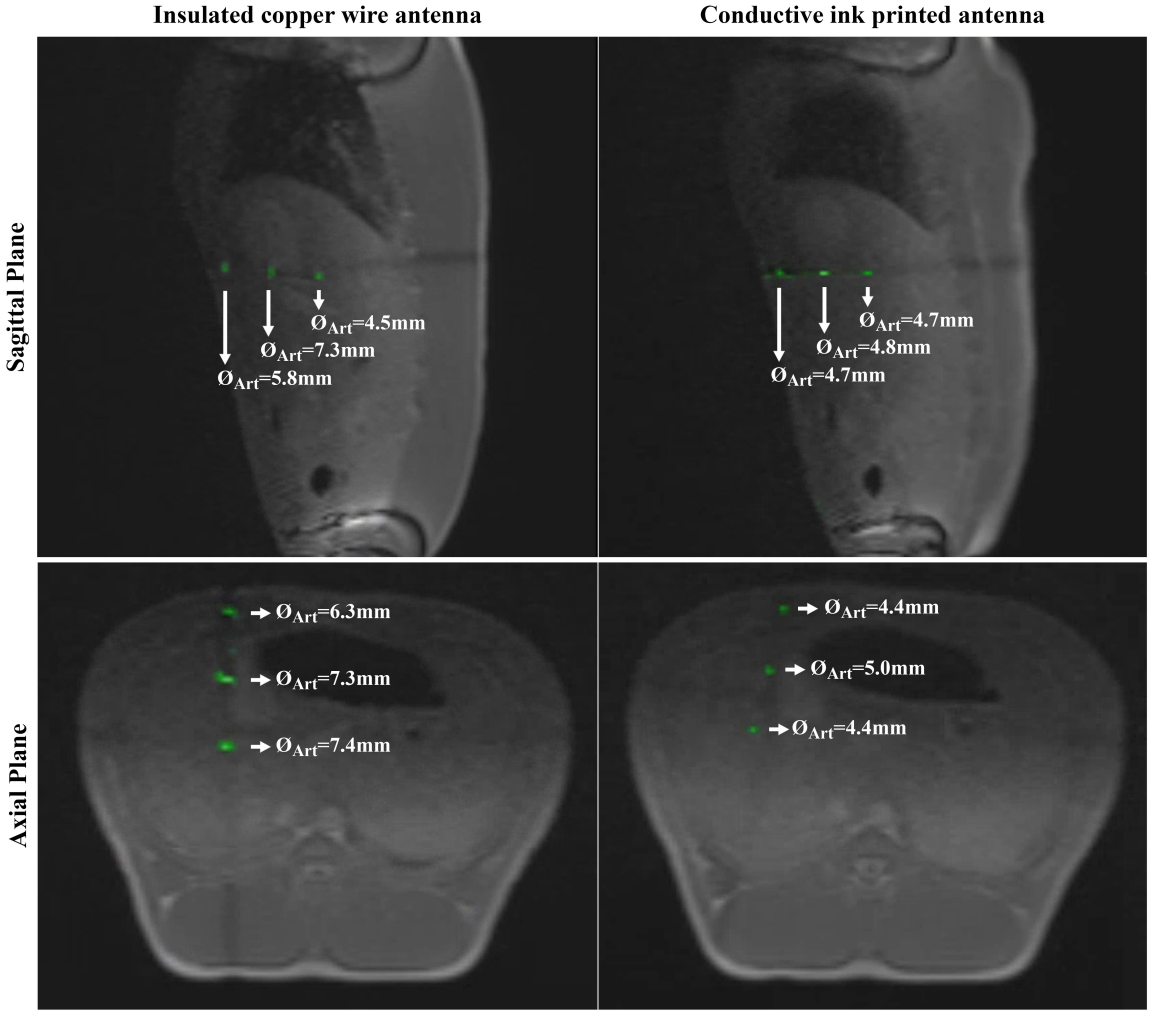


Figure 3.17 In-vivo real-time MRI of the active needle prototypes. The active needle signal is colorized after windowing with window width/window level = 16/16. The printed RF-antenna provides a more refined marker signal obscuring less anatomical information compared to the insulated copper wire RF-antenna.

The real-time MRI signal received from the active needle prototypes via a separate channel was colorized and scaled with window level/window width=16/16, then superimposed on the monochromatic MR images at 3 fps during the in-vivo liver intervention. Intersecting slices in the real-time acquisition creates cross-plane signal saturation and produces dark lines in the images. The MRI marker artifact diameter generated by the active needle prototype with the insulated copper wire antenna measured 6.98 ± 0.49 mm on the axial plane and 5.75 ± 1.44 mm on the sagittal plane, compared to 4.59 ± 0.28 mm and 4.73 ± 0.05 mm on the corresponding planes for the active needle prototype with the printed antenna (Figure 3.17).

3.4 Discussion

The mechanical accuracy of the CNC-based electromechanical system showed the fine printing capabilities of the proposed method with ∼4 µm resolution. The accurate control of the print material flow was secured with the PID control of the ink dispenser unit. The desired antenna or transmission line geometries can be translated to a G-code program and directly printed onto a planar or non-planar surface using the proposed method allowing the fabrication of complex geometries. This technique eliminates the time consuming and/or expensive preparations required for alternative MEMS based fabrication methods [88, 120, 169, 180, 181, 197]. Moreover, any change in the desired RF antenna geometry can be applied instantaneously by modifying the corresponding part of the software control code without the need for any alterations in the fabrication setup.

A lump-free overall device profile is crucial for an interventional device design since surface irregularities compromise the functionality and safety (tissue injury). The printed antenna had only a modest impact on the 0.775 mm hypotube diameter compared with the insulated copper wire antenna (95 µm vs 264 µm, Figure 3.6D and 3.6E). Likewise, the maximum profile alteration along the active needle prototype surface with the printed antenna (20 µm) was lower than the prototype with the 44 AWG insulated copper wire antenna (113 µm).

Mechanical test results showed that the active needle prototype is ∼32-40% more flexible than commercially available equivalents (Figure 3.12). This is attributed to super elastic material properties of nitinol [198] and thin wall thickness (82.5 µm) of the nitinol hypotube used in this study compared to commercial equivalents (175 µm). On the other hand, the active needle prototype performed as well or even better than commercial equivalents during puncture tests (Figure 3.12). Additionally, the active needle prototype successfully punctured the skin tissue, a relatively hard tissue compared to target internal organs, and reached to the liver without a significant deflection during in-vivo experiments. We hypothesize that stiffer nitinol hypotubes [190], other MRI conditional alloys (titanium, Inconel, 316LVM stainless steel, etc.) or even commercially available MRI conditional needles can be used to fabricate stiffer active needles using the proposed method.

The needle RF antenna geometry was optimized using the electro-magnetic simulation results. Simulation results showed that the RF antenna sensitivity can be concentrated around solenoid coils as distinct markers (Figure 3.10). Straight conductors of a RF receive antenna couple only with the magnetic field perpendicular to the conductor axis generated by proton spins and this coupling maximizes when the conductors are parallel to B_0 and diminishes when the conductors are perpendicular to B_0 during MRI [79]. As a result, sensitivity of straight conductors between solenoid coils drops when the antenna is perpendicular to B_0. Shorter solenoids demonstrated less sensitivity drop along the coil approximating a single peak. Maximum peak-to-peak marker SNR can be achieved using 2 mm long solenoid coils with an insignificant difference (∼2 dB) from 2.5 mm long solenoids (Figure 3.10B). Non-zero transverse magnetic field can be observed in the close vicinity of the solenoid turns if the solenoid pitch is sufficiently loose (Figure 3.11). B field vectors were analyzed only for the case where needle prototypes are oriented perpendicular to B_0 since it is the most common use of interventional needles. Similar and adequate RF antenna performance at various angles with respect to B_0 was shown via in-vitro MRI. 2.5 mm long, 10 turns solenoids were chosen since a 32 G (240 µm OD) needle tip was used as the ink outlet and they would provide sufficient visibility minimizing transverse B field coupling, based on the simulation results. A smaller diameter needle tip can be used to print shorter and

tighter pitch coils for more distinct markers. However, the skin effect [191] and the relationship between the near-field SNR and conductor thickness [79] need to be considered. Alternatively, a single loop coil can be employed for whole shaft visibility; or longer, loose pitch solenoids can be used for less distinguished and longer markers [75].

The RF-induced heating rise of the active needle prototype with the insulated copper wire antenna far exceeded clinically acceptable heating limits ($\gg$2°C) in almost all cases even at low-field (low SAR). The RF-induced heating rise of the active needle prototype with the printed antenna always remained under the clinically significant limits ($<$1.65°C) even for an extended imaging duration well beyond typical use (Figure 3.16). The RF-induced heating of metallic parts under MRI is dominated by resistive coupling due to resistive mismatch between the conductor and surrounding tissue [103]. A lower resistance conductor such as insulated copper wire increases the resistive mismatch causing a higher RF-induced heating. The printed antenna exhibited a distributed resistance due to the high intrinsic resistivity of the conductive ink resulting a lower RF-induced heating. We predict that, based on these observations, the RF-induced heating risk of an interventional MRI device antenna can be minimized using printed conductors even with the use of higher field (1.5 or 3.0T) clinical scanners. The tuning and matching of the antenna need to be adjusted for higher field Larmor frequencies [190].

In-vitro and in-vivo MRI visibility performance of the conductive ink printed antenna was comparable to the insulated copper wire antenna demonstrating the real-time device tracking capability (Figure 3.13, 3.14, 3.15 and 3.17). Both prototypes provided sufficient in-vitro real-time MRI visibility during insertion, rotation with respect to B_0 and an exaggerated deflection in the field of view (Figure 3.15). Conductive ink printed markers exhibited a smaller size artifact ($\sim$4.65 mm) compared to the insulated copper wire markers ($\sim$6.4 mm). The smaller artifact size so that the lower SNR of the printed antennas can be attributed to several factors. The wire thickness of the insulated copper wire (44 AWG, 50 µm) is 2.5 times bigger than the conductive ink printed conductor (20 µm). The difference between the artifact sizes is attributed to the relationship between the wire diameter and the near-field SNR [79] explained

by the Biot-Savart law. Also, the coil quality of the insulated copper wire antenna is inherently higher than the conductive ink printed antenna because of the increased coil loss [199] due to the high intrinsic resistivity of the conductive ink. At low-field Larmor frequencies, the SNR is strongly dependent on the coil losses as sample losses can be ignored due to improved magnetic field homogeneity. The SNR can be improved by increasing the quality factor (Q) of the coil since it is directly proportional to the $\sqrt{Q}$ [199]. The conductive ink printed conductor cross section approximates to a flat strip conductor compared to the round shape of the copper wire. The lower SNR performance of the flat strip wires, compared to round wires, was reported in detail in the literature. This effect was attributed to the increased resistance due to the lateral skin effect [200]. Even though the total impedance ($R_{Antenna}$ + R_{Cable}) matching helps to reduce signal losses, the impedance mismatch between the high resistance printed antenna and low resistance coaxial cable causes transmission losses between the printed antenna and the coaxial cable. The impedance matching can be performed at the proximal end of the printed antenna before the micro coaxial cable connection to minimize the resistive mismatch losses. Additionally, The electrical characteristics of the conductive ink can be improved adjusting the silver and epoxy contents of custom conductive inks. As expected, the heat treatment process increases the conductivity of the printed conductors. This effect was attributed to the thermal evaporation of the epoxy increasing the silver content. Further improvement of the conductivity can be achieved using more specialized heat treatment methods including selective heating of the silver nano-particles.

In-vivo signal signature of the active needle prototypes was very well matched to the in-vitro signature and electromagnetic simulation results. Real-time in-vivo needle visualization was performed by manually adjusting the imaging planes. No projection-based tracking was applied [171]. Temporary individual marker signal loss on individual imaging planes was observed due to respiratory motion or slight needle deflection. However, tracking of individual marker signals and needle position was feasible on other imaging planes. Alternatively, imaging planes can be adjusted to capture any specific marker signal. The Imaging speed was set at 3 fps which is sufficient for this application as the liver is only affected by respiratory motion. The active needle

prototypes were well visualized even when using relatively thick 8 mm slices (Figure 3.17). The in-vivo visualization performance was found acceptable and comparable to previously reviewed iMRI devices [2, 163, 171] by the interventional cardiologists and MRI technologists in our group when using a validated acquisition strategy. Hence, we believe that clinical translation of the needle prototype is feasible

Real-time imaging speed and anatomical image quality can be tuned with particular applications in mind, by e.g. using alternative reconstruction and parallel imaging methods [2,161,162], though in this work we calibrated device visibility for use in conjunction with out established clinical acquisition. We predict that at higher imaging frame rates, obtained by increased under sampling, or at higher image spatial resolution, the marker SNR would diminish as predicted by the standard SNR relationships in MRI. However, as the signal from coils on the needle prototype can be processed independently for display, marker visibility can be preserved as long as the marker signal is higher than background noise. In-vitro, the markers displayed a peak-to-trough CNR of ∼16-20 (Figure 3.14) indicating that even with significant increases in under sampling or spatial resolution, marker visualization should be feasible (i.e. CNR $>$ 5). Further work is required to determine the limits of device visibility.

3.5 Conclusion

In this work, a custom, CNC-based conductive ink printing method was introduced for non-planar iMRI device fabrication. The medical grade device manufacturing capability of the proposed method was successfully demonstrated by prototyping a low profile 20 G (0.87 mm OD) active iMRI needle. The active needle prototype was clearly visible both in-vitro and in-vivo during real-time MRI at a 0.55T prototype scanner. The RF-induced heating test results showed that the active needle fabricated using conductive ink heated less than the nearly identical active needle fabricated using insulated copper wire antenna. The maximum temperature rise (1.64°C) was clinically acceptable. This technology will enable fabrication of lower-profile interventional MRI devices, especially attractive for pediatric or other less-invasive procedures.

4. A NOVEL ACTIVE GUIDEWIRE DESIGN WITH A CURVED TIP GEOMETRY FOR INTERVENTIONAL MRI APPLICATIONS UNDER 0.55T

4.1 Introduction

Guidewires are workhorse tools for interventional cardiology. They are utilized for navigation through narrow vascular structures, accessing target lesions, facilitating passage through occlusions, and delivering and exchanging various devices for diagnostic and therapeutic purposes [201]. To date, X-Ray fluoroscopy (XRF) has been the primary imaging modality for image guided minimally invasive cardiovascular procedures. Albeit XRF's capability of providing information about interventional devices, it suffers from limited soft tissue contrast [4] and ionizing radiation which increases long term cancer risk [202]. MRI, on the other hand, is a promising alternative to XRF for image guidance of interventional procedures because it provides excellent soft tissue contrast without ionizing radiation, simultaneous multi-planar real-time imaging with frame rates up to 10 frames per second and intra-operational assessment of hemodynamics and tissue characteristics [2, 161, 203]. Despite the advantages of MRI over XRF, clinical applications of interventional MRI (iMRI) has been limited due to lack of clinically safe and conspicuous iMRI devices [2, 4].

Interventional XRF devices are visualized due to attenuation of incident X-Ray photons by radiopaque materials used in device construction. iMRI devices require additional attempts including an interaction with the main magnetic field (B_0) and surrounding proton spins, to be rendered visible under MRI. iMRI devices are classified as passive, semi-active and active devices in terms of device visualization. Passive devices are visualized due to intrinsic material properties or metallic susceptibility artifacts [165] as dark or bright signatures on the MR image [163]. However, such devices suffer from poor contrast and the device artifact may obscure the surrounding anatomy. Semi-active (inductively coupled) devices interact with the transmitted RF energy and

excite its close vicinity with a higher flip angle providing a bright artifact [169, 170]. However, this amplification so that the device conspicuity diminishes with high flip angles unless specific reverse polarization imaging techniques are implemented [67, 68]. Active devices incorporate RF antennas and electronic components embedded into device body and their signal is directly carried to the MR scanner [171]. Such devices provide high SNR device visibility thanks to the nearby hyperintense MR signal picked up by the device RF-antenna [204]. Their signal can be colorized and overlaid onto the anatomical image for augmented conspicuity [73]. RF coils embedded into the device body can also be used for imaging [75, 205] or automated device tracking [71]. However, long metallic conductors used in active iMRI device designs are prone to RF-induced heating during real-time MRI [103, 127]. Interventional XRF devices use conventional metals such as stainless-steel to provide adequate mechanical characteristics including torque transmission, tracking and stiffness. In addition to RF-induced heating risk, the strong magnetic field employed by MRI systems limits the use of such metals for iMRI device designs. As a result, design and engineering of safe and conspicuous iMRI guidewires become challenging because of the electrical and mechanical requirements and size limitations (sub-millimeter device diameter).

Previously, metallic components were replaced with polymer counterparts to avoid RF-induced heating risk of iMRI guidewires [206]. However, these polymer based guidewires lack adequate mechanical performance. Alternatively, passive guidewire and catheter designs were introduced using segmented and electrically insulated yet mechanically coupled metallic components [111, 195]. However, conspicuity of these passive devices cannot compete with active designs.

Considering the size limitations, the loopless antenna structure can be exploited to design active iMRI guidewires thanks to its simplicity and high near-field SNR. Previously, monopole loopless antenna-based active guidewire (AGW) designs were introduced by extending the inner conductor of a coaxial transmission line, providing a continuous device visibility [79, 80, 124, 207, 208]. Interventional cardiologists need to visualize the whole guidewire and the exact tip location to operate within the vascular structures safely. One drawback of the loopless antenna design is that the current

intensity which defines the antenna sensitivity profile decreases to zero towards the distal tip of the monopole antenna (whip) which renders the distal tip of the guidewire invisible under MRI, risking the operational safety [104]. One attempt was to pack the whip as a coil to recover this signal loss [81]. Even though this approach provides a better balanced sensitivity profile along the whip, it shortens the flexible portion of the guidewire length significantly. Another approach was to taper the insulation at the distal part of the whip to enhance the current sensitivity towards the tip, providing indistinct tip visibility [209]. However, perforation risk and desired clinical mechanical performance require further investigation. Another design integrated a solenoid loop coil to the distal end of a monopole antenna-based AGW to provide tip visibility via a separate channel [69]. This design supersedes the simplicity of the loopless antenna design and risks coupling between two antennas. Alternatively, the whip length was extended and the extended conductor was coiled backwards on the whip to provide a distinct tip visibility [70, 210]. Additionally, a fiberoptic temperature probe was integrated to this design to provide real-time temperature monitoring of the AGW [70]. Recently, another approach combined continuous device visibility with mitigated RF-induced heating risk by electrically exposing a portion of the distal tip and actively controlling the current flow on the guidewire [211]. Despite this is an innovative approach, perforation and the micro-shock risks posed by the exposed metal tip require further investigation [212, 213]. As a result, iMRI field still lacks a commercially available, electrically safe AGW with acceptable mechanical performance and adequate conspicuity.

Recent developments in the low-field MRI technology, on the other hand, enable safe-by-design iMRI devices [121, 204]. The reduced RF power deposition [122, 123] and increased electrical wavelength [103, 124] afforded by contemporary high-performance low-field systems inherently enhance iMRI device electrical safety. In this study, we introduce a novel, 0.89 mm (0.035") outer diameter (OD) actively visualized, monopole antenna-based metallic guidewire design for human interventional cardiac catheterization procedures at 0.55T. Proposed design incorporates an atraumatic curved tip geometry, a unique distal tip and continuous shaft visibility, clinically acceptable mechanical characteristics and a detachable radio frequency electrical connector which

allows catheter delivery and exchange over the AGW. Characteristics and performance of the proposed design were reported, briefly [214].

4.2 Methods

Design specifications of the active guidewire prototype were defined by the interventional cardiologists in our group to satisfy clinical user expectations. The final prototype was expected to have a 162.5 cm total length and 0.89 mm OD with a detachable electrical connector to deliver and exchange commonly used cardiovascular catheters over the guidewire during the procedure. Mechanical performance of the AGW was expected to be comparable with commonly used, commercially available equivalents. An atraumatic curved tip geometry with a unique tip and continuous shaft visibility is required to allow safe navigation and steerability through various luminal structures. A series of electromagnetic simulations were performed to define the optimum tip coil choice and provide continuous visibility at the distal tip of the AGW.

4.2.1 Electromagnetic field simulations

Previously, it was demonstrated that electrically connecting a tip coil recovers the weakened monopole antenna signal towards the tip and provides a distinct tip signal [70,210]. It is also known that insulating the whip alters the effective wavelength of the monopole antenna and provides a more homogenous current intensity throughout the whip resulting a higher SNR [81,209]. Here, we hypothesize that electrically extending the whip length using a tip coil, first, helps to push the current intensity towards the tip. Then, since the tip coil conductor is wound backwards on the whip, both radial and longitudinal components of the magnetic (B) field generated by the tip coil counteract with the transverse B-field of the whip cancelling out each other. This cancellation leads to a local signal decay along the coil, providing a distinct tip signal [70]. It was shown that B-field distribution around a solenoid coil so that the signal signature on the MR image can be altered adjusting the normalized pitch (p) of a solenoid

coil [75, 108, 204]. A previous study showed that a 50 mm long, 0.762 mm OD tip coil made of MP35N coil wire with 0.076 mm OD attached to a monopole antenna provides a distinct tip signal at 1.5T [70]. Finite elements method electromagnetic simulations were performed using COMSOL 5.2a (Stockholm, Sweden), first, to study the magnetic field along the whip and around the tip coil, and then to verify if a thinner coil wire so that a tighter pitch coil can be used to generate a dominant B_1^+ field around the tip coil and provide a continuous tip signal.

First, the AGW prototype was modeled as a monopole antenna by extending the inner conductor of a coaxial structure, using COMSOL computer aided design module. Next, all conductor materials were defined as nitinol with 80 Ω/m impedance at 23.66 MHz. The polymer material which separates the inner and outer conductors of the coaxial structure and covers the entire guidewire was defined as a dielectric material with electrical conductivity of 0 S/m and relative permittivity of 3.2. A finite volume encapsulating the antenna whip was defined as a gel material with electrical conductivity of 0.47 S/m and relative permittivity of 78, mimicking human body loading conditions. This definition simulates partial immersion of the AGW in the gel phantom. The AGW was aligned parallel to B_0 since this is the most common use condition of a guidewire. Finally, it was excited at the junction at 23.66 MHz with a 1A sinusoidal coaxial source to exploit the reciprocity principle and avoid the computationally expensive simulation of the birdcage coil used for RF transmission in clinical MRI scanners. Only wire diameter of 0.076 mm and 0.051 mm were simulated as the tip coil conductor since they are the thinnest insulated MP35N and 35N LT wires, respectively, we could obtain in the market. Normalized solenoid pitch, coil OD and coil length were kept 0.2, 0.762 mm and 50 mm, respectively, during the simulations and only coil wire OD was adjusted. Electromagnetic simulations were performed for a straight tip guidewire design since implementing a curved helical geometry dramatically increases the simulation time and required computational resources. Tip coil length was optimized experimentally for the curved tip geometry based on the simulation results.

4.2.2 Active iMRI guidewire design

The AGW prototype incorporating a modified monopole loopless antenna was fabricated in an ISO Class 7 cleanroom using medical grade MRI compatible materials. A custom ground nitinol rod and a superelastic nitinol hypotube were used to form the monopole antenna design. These metal components were coated with different size thermoplastic Pebax tubings using a hot air source (210-A, BEAHM Design Inc., CA). By this way, the inner conductor is extended 37.5cm ($\sim\lambda/4$ at 23.66 MHz in human body loading conditions) [103] out of nitinol hypotube to maximize the radio frequency receiver antenna performance. A tight pitch tip coil with 0.762 mm coil OD, made of a 0.051 mm OD insulated 35N LT wire (Fort Wayne, IN) was placed at the distal end of the whip and soldered to the whip only at the distal end, and the proximal end remained floating. Finally, overall guidewire length was coated with pebax thermoplastic polymer for electrical insulation purpose. (Figure 4.1A and 4.1B). The optimum solenoid coil length was 50 mm, based on straight whip simulation results, and experimentally decreased to 14 mm for the curved tip geometry.

A detachable radio frequency connector was designed using commercially available torquer device (97327, Qosina, NY) and a mmcx connector (262125, Amphenol RF, CT) (Figure 4.1C). The monopole antenna impedance was matched to 50Ω at 23.66 MHz using a tune and match circuit via a vector network analyzer (VNA) (E5080B, Keysight, CA). A radio frequency balun was used to eliminate shield common mode currents and a positive intrinsic negative (PIN) diode was used to actively detune the monopole antenna during RF transmission. Additionally, a leakage current blockage circuit was added to the tune and match circuit to avoid current leakage from MRI RF receiver chain to the AGW and eliminate the micro shock risk (Figure 4.1D). The AGW prototype was limited to function only in receive mode and no RF energy was allowed to be transmitted over it.

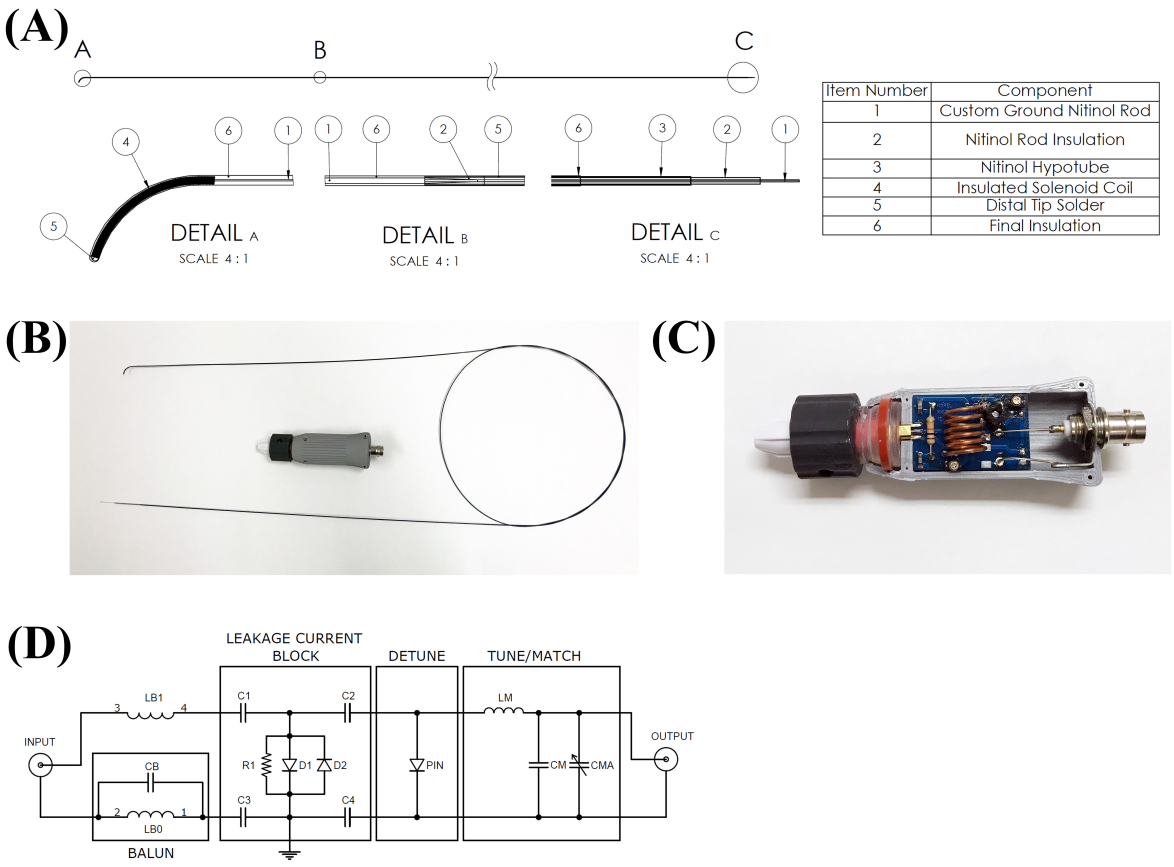


Figure 4.1 (A) The component list and schematic representation of the AGW prototype. (B) Final assembly of the AGW prototype and the detachable handle. (C) Subassembly of the detachable handle showing the modified torquer device and the tune and match and leakage current blockage circuit. (D) Electrical diagram of the tune and match and the leakage current blockage circuit.

Additionally, three straight guidewire prototypes (one with no tip coil, two with a 50 mm long, 0.762 mm OD tight pitch tip coils made of 0.076 mm OD insulated MP35N and 0.051 mm OD insulated 35N LT coil wires [Fort Wayne, IN], respectively) and a curved tip guidewire prototype with a 24 mm long, 0.762 mm OD tight pitch tip coil made of 0.076 mm OD insulated MP35N coil were manufactured to assess the effects of invisible and distinct tip signal signatures.

4.2.3 In-vitro characterization tests

Electrical characteristics of the AGW prototype were assessed using the VNA both in air and in an ASTM gel phantom with electrical conductivity of 0.47 S/m and relative permittivity of 78. The leakage current tests were performed using a power supply (Vega 650, TDK-Lambda, UK) used in Siemens Aera scanners, a vendor provided 4-channel flex coil adaptor and a leakage current tester (LT-601HC, ED&D Inc., NC).

A real-time balanced steady-state free precession (bSSFP) sequence (TE/TR: 1.05/2.50ms, flip angle: 45°/60°/75°, FOV: 320 × 320mm, bandwidth: 1042Hz/Px, matrix: 192×144, slice thickness: 6mm, 3 fps), typically used for clinical MRI catheterization at 0.55T at our institution, was used during in-vitro tests. The bSSFP sequence is commonly used in iMRI thanks to its favorable image contrast and high image acquisition speed. bSSFP also presents an appropriate upper limit specific absorption rate (SAR) with combination of short TR/high flip angle which challenges the RF-induced heating performance of iMRI devices [194]. In-vitro RF-induced heating and imaging performance of the AGW prototype was tested using a high-performance low-field scanner (prototype MAGNETOM Aera, Siemens Healthcare, Erlangen, Germany) at 0.55T.

RF-induced heating performance of the AGW prototype was tested in a gel phantom per ASTM 2182-19 [105]. The distal 50cm portion of the AGW prototype was immersed in the gel phantom, aligned parallel to B_0, 2 cm away from the right edge of the phantom and 3 cm below the surface of the gel where the SAR is maximum (as observed in previous experiments) [114, 175, 204] and heat dissipation is minimum. Scans were performed in the "First Level" SAR mode (max. 4W/kg) with reported whole body SAR values of 2.78W/kg, 3.44W/kg and 3.96W/kg for 45°, 60° and 75° flip angles, respectively. 0.080 mm OD fiberoptic temperature probes (OPT M-170, OpSens, Canada) were used for temperature measurements. Temperature probes were attached to the guidewire body using a 0.082 mm ID, 0.090 mm OD polyamide hypotube (214-1586, Nordson Medical, MA, USA) and 3mm long heat-shrink polymer

hypotube segments as described before [195]. First, the temperature probe was advanced 10 mm beyond the distal end of the AGW prototype. Next, the "hot spot" where the maximum heating occurs, was located by gradually withdrawing the temperature probe alongside the AGW prototype, profiling the temperature rise during MRI scan. Finally, RF-induced heating tests were performed as the temperature probe was placed at the hot spot. Baseline temperature was recorded for 30 s before each scan and then the AGW prototype was scanned for 90 s which represents the start of saturation after the clinically significant temperature rise. Same measurements were repeated when the AGW prototype is in tandem with a MRI compatible 6 French metal braided catheter (Infiniti, Cordis, FL) in various tandem configurations to assess the effects of the metal braiding over the AGW prototype. Finally, the AGW prototype was scanned with 75° flip angle for 15 minutes, both alone and in tandem with the metal braided catheter in the configuration which maximum heating occurs, to simulate a challenging, uninterrupted long scan.

In-vitro MRI visibility performance of the AGW prototype was tested using the same bSSFP sequence but with only 45° flip angle in the ASTM gel phantom. The AGW prototype was placed parallel to B_0, 5 cm away from the right edge of the phantom and 4 cm below the gel surface. It was first scanned alone, and then in tandem with a list of commercially available, commonly used catheters. The list of catheters is tabulated in Table 4.1. Additionally, guidewire prototypes with no tip coil and a tip coil, made of MP35N wire, were scanned alone under same conditions. Still MR images were reconstructed using only the active channel signal received from the AGW antenna and all other imaging coils were deactivated. All prototypes were scanned with the same RF receiver gain. SNR maps of the AGW prototypes with tip coils were calculated using the pixel SNR method [215] with N=100, using Matlab (2020a, Mathworks, MA) to assess the signal profile along the antenna whip. Real-time in-vitro MRI tracking performance of the AGW prototype was tested using a prototype interactive real-time MRI interface (MonteCarlo, Siemens, Germany) with a real-time bSSFP sequence (TE/TR:2.0/4.0ms, FA:45°, FoV: 320x320mm, bandwidth: 1042 Hz/Px, matrix: 192x144, ST:8 mm, 3 fps). First, the AGW prototype alone was manipulated in a 3D-printed left heart model. Next, A 6FR pig-tail catheter

(SuperTorque, Cordis, FL) was operated using the AGW prototype. A four-element spine coil was used for phantom imaging. The active channel signal was colorized on the MR image after scaling with window level/window width = 16/16.

Table 4.1
Commercially available catheters with which the active guidewire prototype was tested in tandem.

Commercially available catheter	Braiding type
Cordis, Super Torque Angiographic Catheter, 5 Fr.	Metallic
Cook, Flow Directed Balloon Catheter.	None
Medtronic, Pulmonary Wedge Pressure Catheter.	None
Vascor, Balloon Wedge Pressure Catheter.	None
Edwards, True Size Monitoring Catheter.	None
Edwards, True Size Hi-Shore Monitoring "T" Tip Catheter.	None
Arrow, Balloon Wedge Pressure Catheter.	None
Edwards, True Size Monitoring “S” Tip Catheter.	None
Cordis, Super Torque JR4.	Metallic
Cordis, Super Torque MPA.	Metallic
Woven, NIH.	Non-metallic
Woven, Goodale-Lubin nylon-braided Catheter.	Non-metallic

Mechanical performance of the AGW prototype was tested for torque transmission, stiffness and tracking, and compared to commercially available, commonly used clinical guidewires including a Glidewire (Terumo, NJ), a HiWire (Cook, IN) and a Nitrex (stiff) (Medtronic, Dublin, Ireland). The stiffness test was performed using a digital force meter (ZP-11, Imada Inc., IL, USA) and a programmable linear actuator (MH2, Imada Inc., IL, USA). The guidewire sample was fixed onto a 3-point bending apparatus and pushed for 10 cm and then allowed to recoil to its initial state. The force required for pushing and recoiling was measured. The torque transmission test was performed placing the guidewires in a vessel phantom mimicking the trajectory of a transfemoral catheter across the ascending aorta. Two identical paper protractors were attached to both ends of the test sample. The guidewire sample was torqued from the proximal end in 90° increments and the resulting distal end rotation was measured.

Finally, the trackability of the guidewire samples were tested using a dedicated apparatus (IDTE 2000, MSI, AZ) by pushing guidewire samples through a 55 cm long, tap water filled vascular phantom and measuring the required force via a loadcell (Figure 4.2). Additionally, stiffness of the AGW prototype was tested by straightening out a metal braided pigtail catheter (Supertorque, Cordis, FL) and compared to Glidewire (Terumo, NJ).

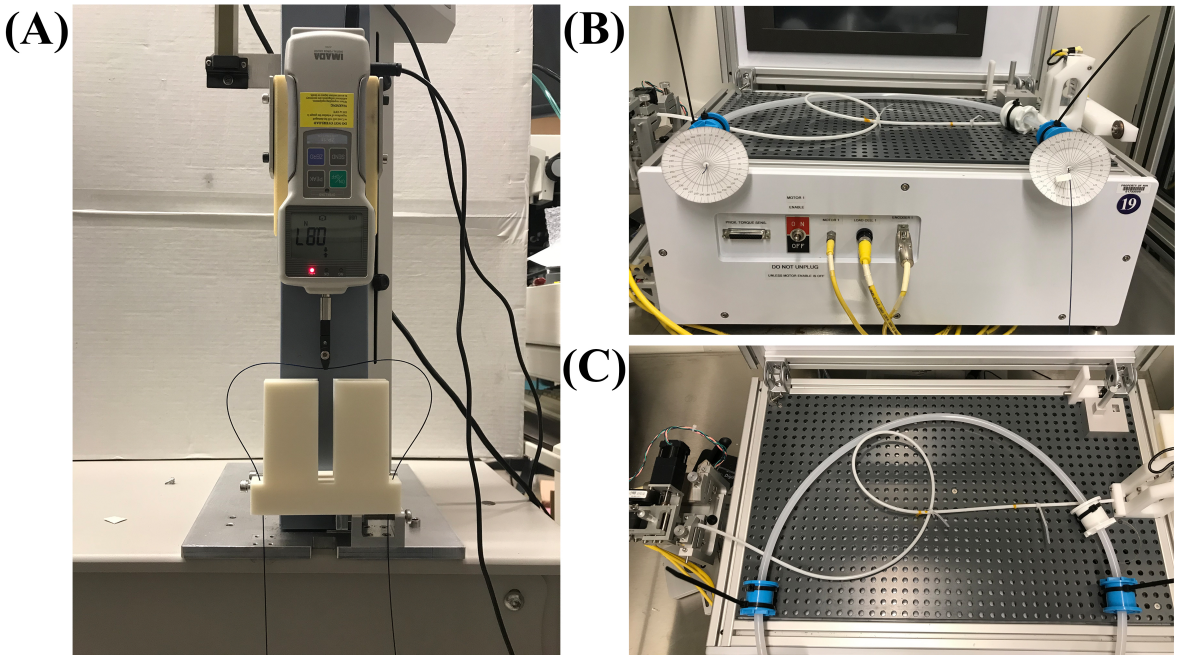


Figure 4.2 Mechanical test setups for (A) the stiffness, (B) torque transmission and (C) trackability tests of the AGW prototype. The AGW prototype is fixed on the custom apparatus forming an arch for the stiffness test. A paper indicator was attached to the proximal end of the AGW prototype for the torque transmission test and the tip cure itself was used as the distal end indicator. The AGW prototype was manipulated by the rubber coated actuators of the dedicated trackability test setup.

4.2.4 In-vivo characterization tests

The real-time in-vivo MRI visibility performance of the AGW prototype was tested in one swine under general anesthesia. Animal experiments were approved by the National Heart, Lung and Blood Institute (NHLBI) Animal Use and Care Committee and performed according to the contemporary National Institutes of Health (NIH) standards. A non-sterile prototype was tested as an "add-on" experiment to another

non-survival porcine experiment to minimize use of animals. All used general anesthesia and mechanical ventilation. First, the guidewire prototype alone was advanced to the left ventricle, retrograde, following femoral entry. Next, the AGW prototype was advanced through the inferior vena cava, in tandem with a balloon catheter (Arrow, Teleflex, PA). MonteCarlo interactive real-time MRI interface software was used with the same real-time bSSFP sequence used for in-vitro real-time MRI. The active channel signal was colorized on the MR image after scaling with window level/window width=16/16. No projection based tracking method was applied and the real-time device tracking was performed manually by adjusting imaging planes.

4.3 Results

4.3.1 Electromagnetic field simulations

Figure 4.3 shows the electromagnetic simulation results of the AGW prototype with no tip coil, and tip coils made of a 0.076 mm OD (MP35N) and 0.051 mm OD (35N LT) insulated wires. B_1^+ field distributions show that the tip coil configuration alters the signal signature of a monopole antenna-based AGW.

4.3.2 In-vitro characterization tests

Characteristic impedance of the coaxial part of the AGW prototype ($r_o = 0.787$ mm, $r_i = 0.127$ mm) was calculated as 61.13 Ω. The input impedance of the modified monopole antenna was 22.2 - j15.4 Ω in air and 37.6 - j4.9 Ω in the gel phantom. The leakage current was measured as 45.1 and 13.2 µA before and after the leakage current block, respectively.

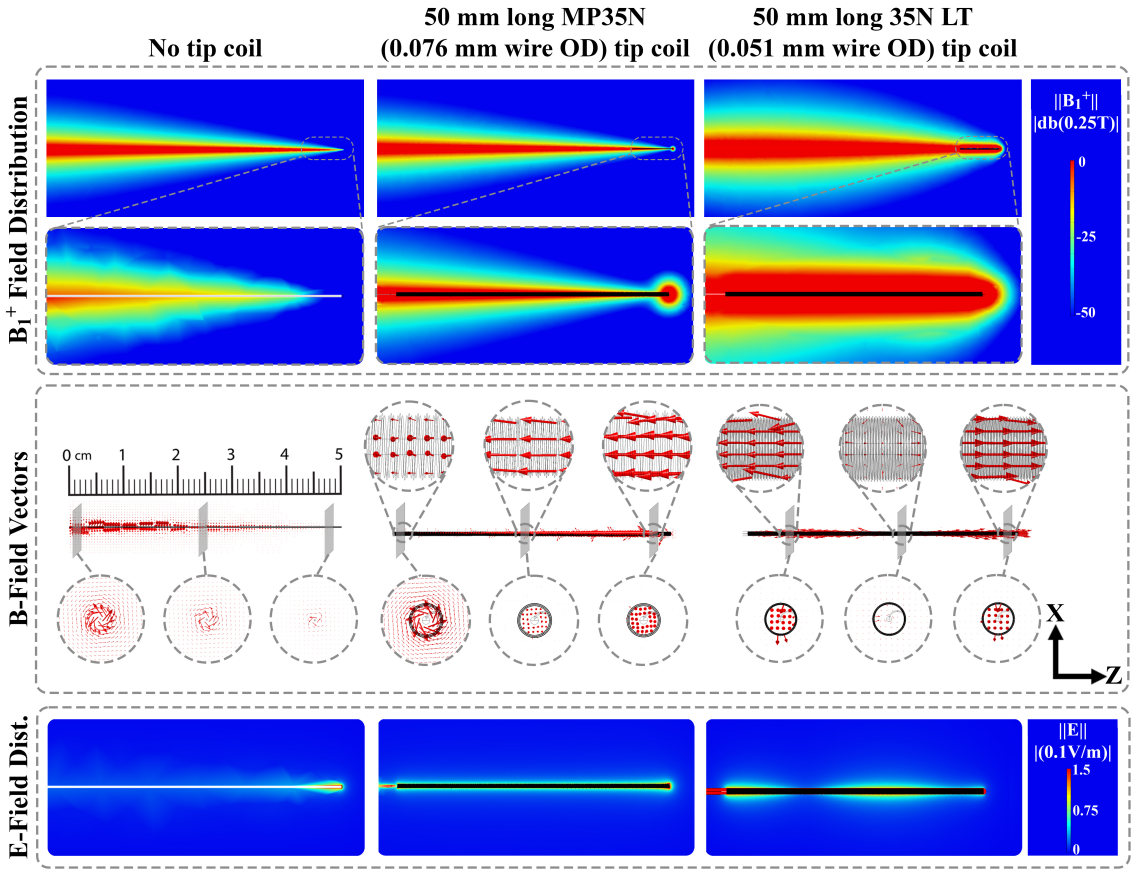


Figure 4.3 Electromagnetic simulation results of the AGW prototypes. B_1^+ field distribution shows that signal sensitivity towards the tip of the monopole antenna-based AGW can be recovered using a tip coil and configured adjusting the coil specifications. B-field vectors and the E-field distribution within and around the tip coil show the standing wave formation along the monopole antenna and its effects on the generated B-field direction so that the MRI artifact signature.

RF-induced heating test results are shown in Figure 4.4. The hot spot was at the distal tip of the AGW prototype. The temperature at the hot spot starts to rise right after the MRI scan starts and saturates quickly after the first 60 seconds. Maximum temperature rise during a 75° flip angle, 90 seconds long scan was 4.64 and 5.98 °C when the AGW prototype was alone and in tandem with the metal braided catheter, respectively. Maximum in tandem temperature rise was observed when the distal tip of the metal braided catheter was aligned with junction. Maximum temperature rise at the end of a 75° flip angle, 15 minutes long scan, representing a challenging uninterrupted scan, was 5.21 and 6.54 °C when the AGW prototype was alone and in tandem with the metal braided catheter, respectively.

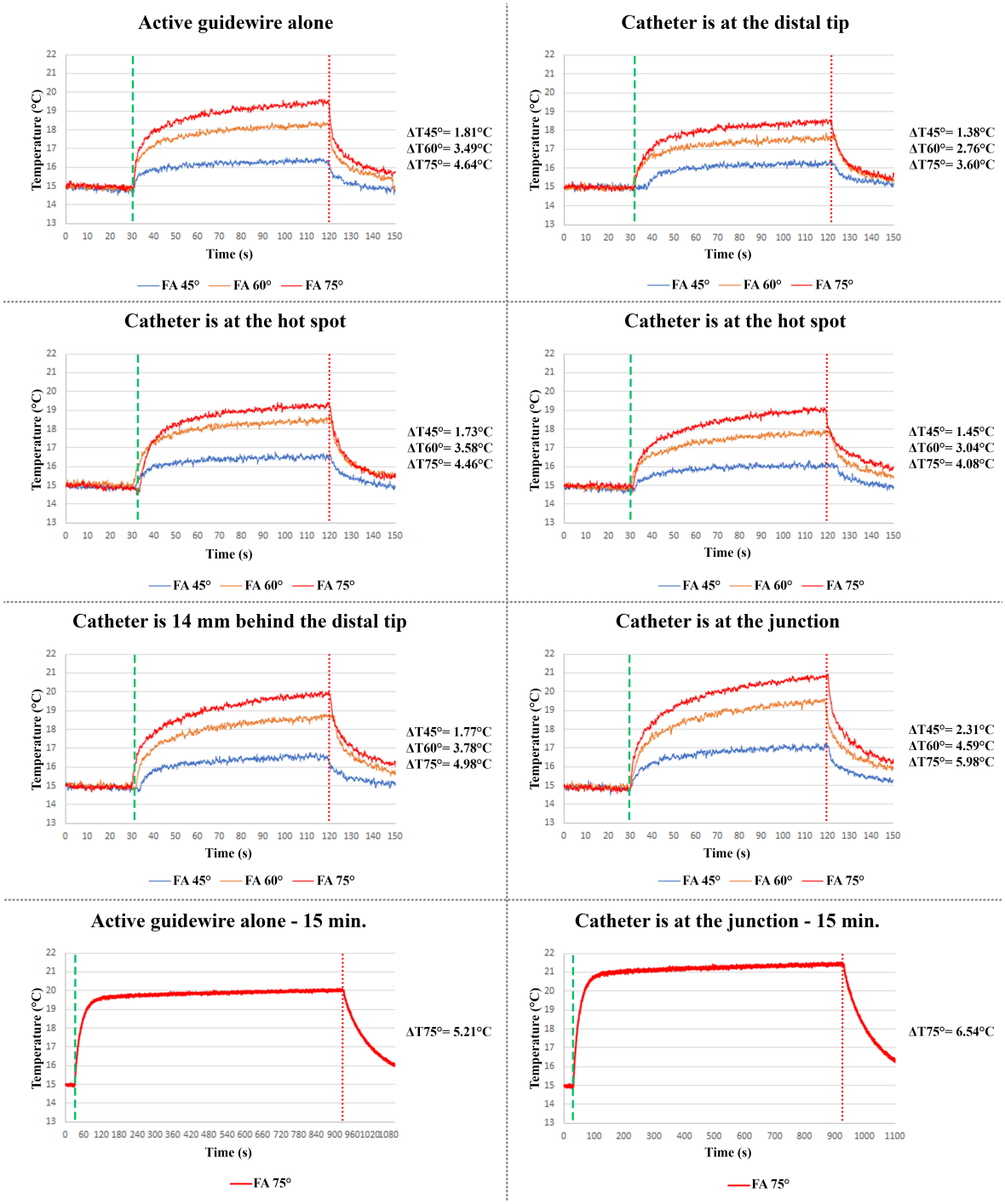


Figure 4.4 RF-induced heating results of the AGW prototype alone and in tandem with a MRI compatible metal braided catheter (Infiniti, Cordis, FL). Maximum temperature rise is observed when the tip of the metal braided catheter is aligned with the junction of the AGW prototype. Green dashed line indicates the start of the MRI scan. Red dotted line indicates the end of the MRI scan.

Figure 4.5 shows in-vitro MR images and corresponding SNR maps of the AGW prototypes aligned parallel to B_0 and alone in the gel phantom. The close vicinity hyperintense MR signal picked up by the AGW prototype, appears as a bright artifact on the image. 0.051 mm OD coil wire provides a continuous tip signal while 0.076 mm OD coil wire provides a distinct tip signal.

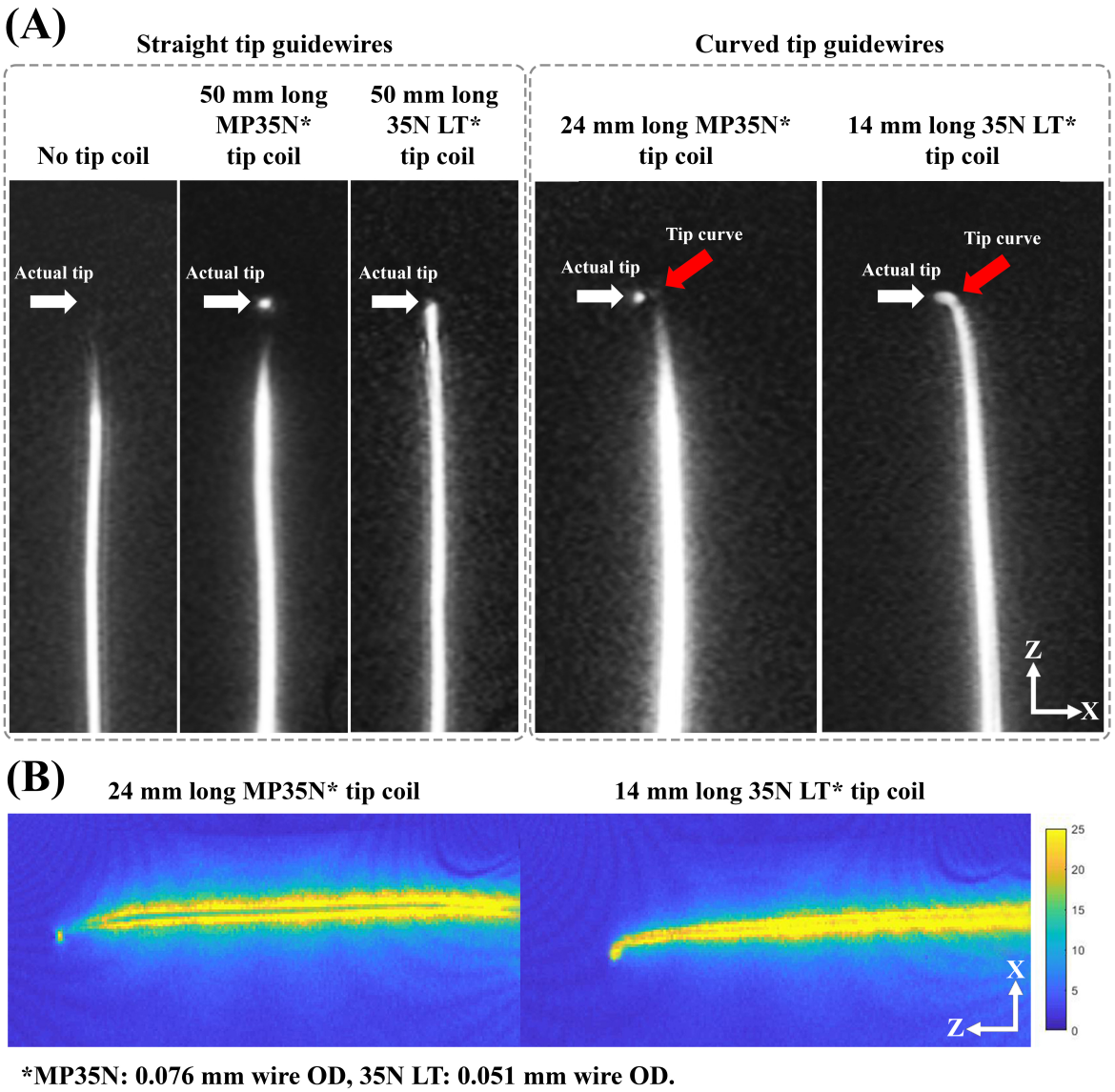


Figure 4.5 In-vitro MR images of the AGW prototypes. Artifact signature of the straight guidewire prototypes match with the electromagnetic simulation results. Use of a relatively loose pitch tip coil (MP35N coil wire) results in a distinct tip signal which causes the loss of the curve information for the curved tip geometry. The tight pitch tip coil (35N LT coil wire) provides a full shaft and continuous curve visibility which also gives information about the wire rotation.

In-vitro MR images of the AGW prototype in tandem with commercially available clinical catheters are presented in figure 4.6.

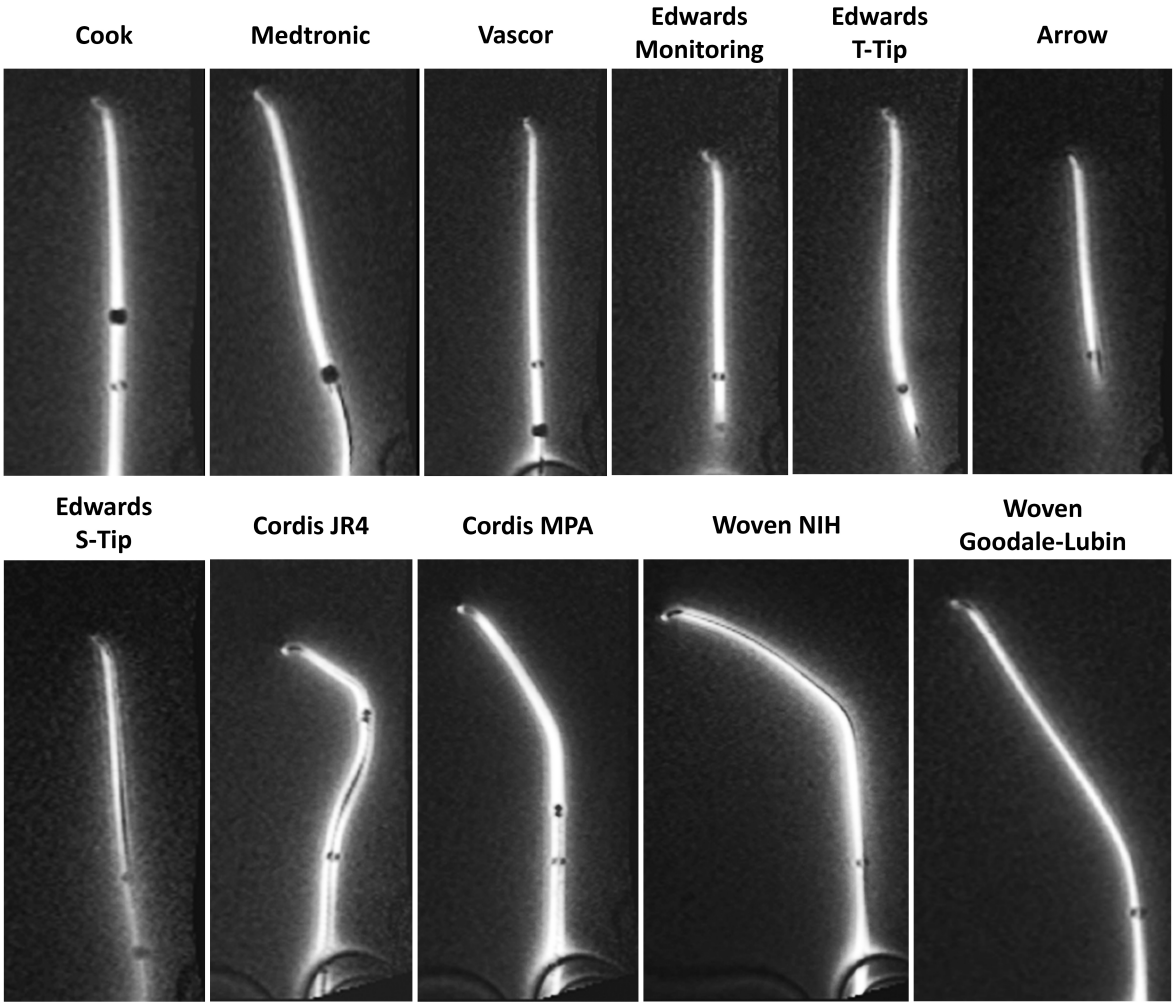


Figure 4.6 In-vitro MRI of the AGW prototype in tandem with commercially available clinical catheters. Circular dark artifacts on images are signal voids caused by mounting pegs and/or air filled balloons of the catheters. Since the tested catheters have curved geometries, it is not always possible to align the whole AGW prototype parallel to one plane which explains the SNR fluctuations along the AGW prototype.

Figure 4.7 shows in-vitro real-time MR images of the AGW prototype alone in the 3D-printed heart model and in tandem with a metal braided, pigtail Supertorque, Cordis catheter.

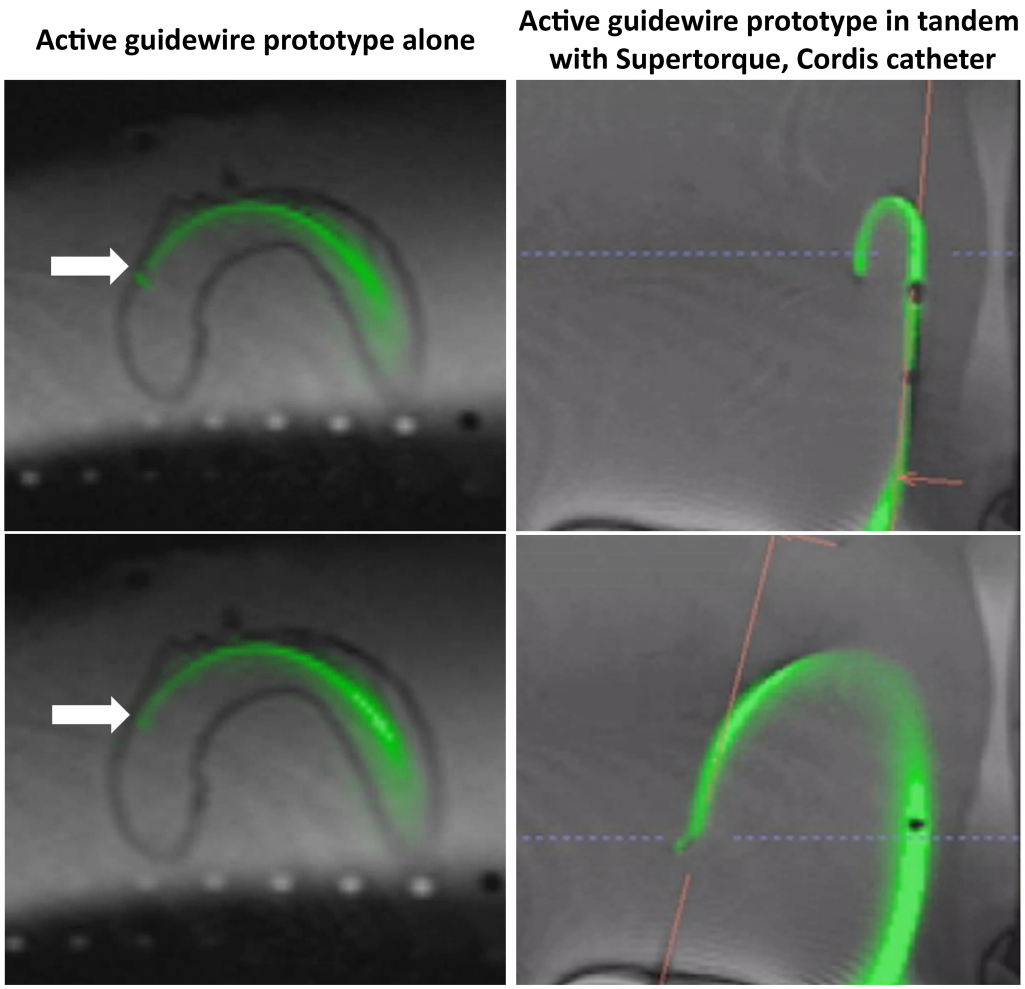


Figure 4.7 In-vitro MR images of the AGW prototype alone in a 3D-printed heart model and in tandem with a Supertorque, Cordis catheter. White arrows indicate the actual tip curvature. As the AGW tip pushes against the model wall the tip curve is pushed out of imaging plane resulting a signal loss. Curve signal recovers as the AGW tip is free in the model. The dark susceptibility artifact on the top right image is caused by the metallic braiding of the pigtail catheter. AGW prototype can straighten out the pigtail catheter without any alteration on the device signal.

Mechanical test results are shown in figure 4.8 and compared to commonly used commercial equivalents. Figure 4.9 shows the additional stiffness test results by straightening out the metal braided pigtail catheter.

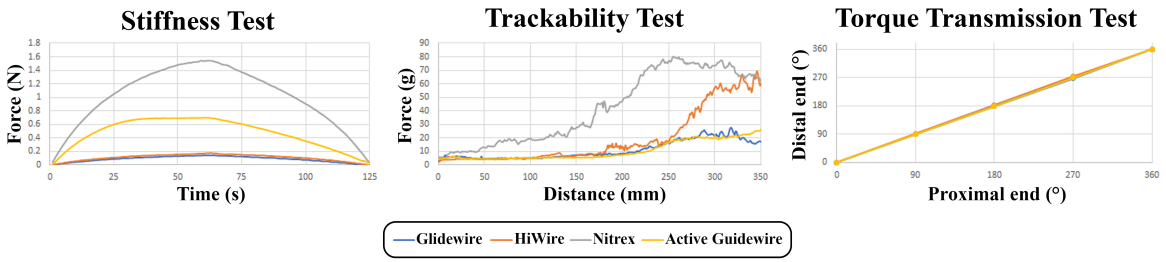


Figure 4.8 Figure 4.8. Mechanical test results of the AGW prototype compared to commercially available equivalents. All results show that the AGW prototype has clinically acceptable mechanical performance comparable to the commercially available equivalents.

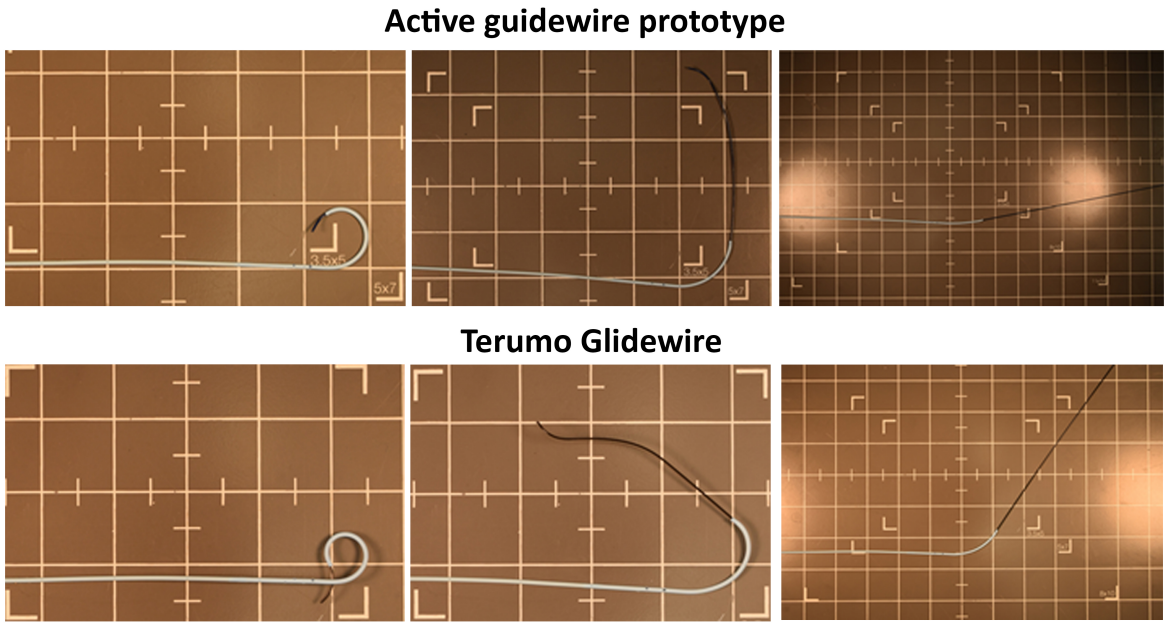


Figure 4.9 Figure 4.9. In tandem stiffness test result. AGW prototype has a comparable stiffness with the commercially available guidewire and can completely straighten out a metal braided pigtail catheter.

4.3.3 In-vivo characterization tests

Figure 4.10 shows in-vivo MR images of the AGW prototype in the aortic arch alone and in inferior vena cava in tandem with the balloon catheter. Real-time MRI signal received from the AGW prototype via a separate channel was colorized and scaled

with window level/window width = 16/16, and superimposed on the monochromatic anatomical images at 3 fps during real-time MRI. The AGW prototype provided in-vivo full shaft and continuous tip visibility.

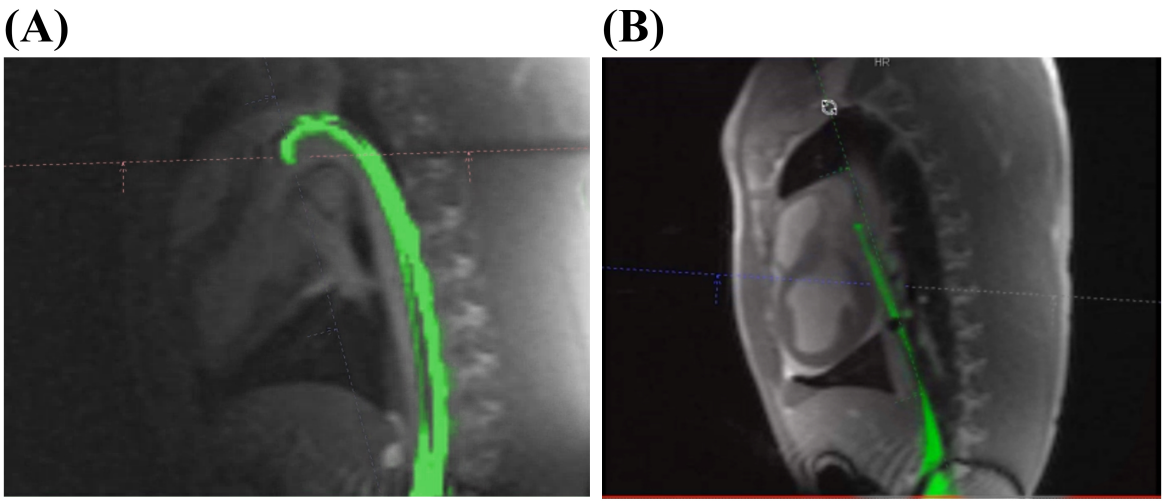


Figure 4.10 In-vivo MR images of the AGW prototype (A) alone, rotated parallel to the imaging plane in the aortic arch and (B) in tandem with the balloon catheter, rotated perpendicular to the imaging plane in inferior vena cava. The black dot on the image represents the air filled balloon. The full shaft and continuous shaft visibility provides exact tip location and rotation information in both cases.

4.4 Discussion

This study introduces a novel, 0.89 mm (0.035") OD, monopole antenna-based actively visualized metallic guidewire design with full shaft and continuous tip visibility, suitable for MRI guided high performance human catheterization procedures at 0.55T.

Electromagnetic simulation results showed that the signal signature of a monopole antenna-based AGW can be altered using a tip coil (Figure 4.3). Even though insulating the whip increases the effective wavelength [81], when there is no tip coil, the performance of a monopole antenna with a 37.5 cm extended inner conductor approximates to a half wavelength dipole antenna. The current intensity so that the B-field along the whip approximates to zero towards the tip rendering the distal end of the

AGW prototype invisible under MRI (Figure 4.5A). When the whip length is extended using an insulated MP35N wire (OD = 0.076 mm) and the extension is coiled backwards on the whip with a relatively loose pitch (p = 0.2), the current intensity is pushed towards the open end of the tip coil increasing the current intensity at the geometrical end of the whip. Here, the tip coil still exhibits solenoid behavior generating a strong longitudinal B-field at the center and a strong radial B-field around the soldered end (Figure 4.3). Longitudinal and radial B-fields of the solenoid counteract with the transverse B-field generated by the straight whip before the soldered end cancelling out each other. Also, the radial B-field among relatively loose coil windings results in a decreased B-field along a solenoid structure [204]. The combination of the field cancellation and the decreased B-field along the solenoid results in a signal loss right before the distal end. However, the current intensity still decreases to zero towards the open end of the coil causing the loss of the dominant B-field generated by the coil. Right after the cancellation of B-fields, the transverse B-field of the whip becomes dominant and recovers the MRI visibility. All these effects collectively provide a full shaft visibility with a distinct tip signal for the AGW prototype (Figure 4.5). E-field distributions along the tip coil show that multiple standing wave high points form along the tip coil when the 35N LT coil wire (OD = 0.051 mm) is used. This is attributed to the fact that a longer conductor is packed in the same volume to form the same length (50 mm) tip coil, extending the whip length by multiple orders of $\lambda/4$, when a thinner coil wire is used. As a result, current intensity does not decrease to zero at the open end of the coil and the solenoid behavior is sustained all along the tip coil. However, because of the multiple standing wave high points, the longitudinal B-field direction changes along the coil and only the transverse B-field of the straight whip exists around the middle of the coil (Figure 4.3). The non-zero current intensity generates a dominant B-field also at the open end of the solenoid providing a continuous tip and full shaft visibility for the AGW prototype (Figure 4.5).

Small dimensions of guidewire components in combination with the long guidewire length (162.5 cm), require a large number of elements (>109) to discretize the guidewire design with curved tip geometry. Simulating such a design with finite-difference time-domain solvers takes a few weeks for each configuration, using our computational ca-

pacity with the disadvantage of the low-field frequency. On the other hand, the required memory by the finite element method solvers to simulate the same design exceeds the capacity of our workstation (512 GB). As a result, electromagnetic simulations were performed only for the AGW design with straight tip geometry. The tip coil length was experimentally shortened to 14 mm to obtain a continuous tip signal for the guidewire design with curved tip geometry. B_1^+ field can be used to predict the sensitivity profile of a RF antenna in a circularly polarized B-field. B_1^+ and B_1- fields are the rotational components of the projection of the B-field on a plane normal to B_0 [68]. Hence the orientation and shape of a coil affect the B_1^+ distribution so that the MRI visibility of the coil. The requirement for shortening the tip coil of the AGW design with curved tip geometry was attributed to the changing geometry and orientation of the tip coil. However, detailed electromagnetic simulations should be performed using a higher computational capacity or alternative simulation strategies to investigate the magnetic field along and within the curved tip coil.

RF-induced temperature rise safely remained under 6°C when the AGW prototype is alone and slightly exceeded 6°C (6.54°C) when it is in tandem with a metal braided catheter during 15 minutes long scans (Figure 4.4). Maximum RF-induced heating was observed at the upper limits of the scanner allowed whole body SAR (75° flip angle, 3.96W/kg) and when the AGW prototype was positioned in the max. SAR location of the phantom where the heat dissipation is minimum. Additionally, the maximum heating was observed when the metal braided catheter was aligned right at the junction. This is attributed to the adjusted effective wavelength along the coaxial structure which eventually effects the active detuning performance. The plasma protein denaturation starts around 6°C above the body temperature setting the safety limit for clinical applications [216]. However, we hypothesize that the RF-induced temperature rise will safely remain under 6°C during a human catheterization due to the perfusion and more heterogenous E-field distribution within the body. Besides, it is very unlikely to operate the proposed design in the maximum heating tandem configuration during such a long scan. No adverse change in the hemodynamics was observed during the in-vivo animal experiments, supporting our hypothesis. The RF-induced heating tests were performed per ASTM 2182-19a during this study. One limitation of this standard

is that it is designed for completely implanted passive devices and does not cover the partially immersed active devices. Also, the establishment of the relationship between the in-vitro and in-vivo temperature rise is expected from the investigator [105]. To ensure complete electrical safety, a more comprehensive RF safety assessment of the proposed design via the transfer function approach [102] per ISO/TS 10974:2018 [126] is definitely required and currently, it is being investigated by our group.

In-vitro MR images of the AGW prototypes very well matched with the electromagnetic simulation results for the straight tip geometry (Figures 4.3 and 4.5). SNR maps showed that both configurations with distinct and continuous tip visibility provide full shaft visibility. Localization of the exact tip location is important for the interventional cardiologists for operational safety and efficiency. The curved tip AGW design with the distinct tip signal lacks the curve information which is important for the assessment of the AGW rotation and for eliminating the perforation risk.

The mechanical performance of the proposed design was comparable to the commercial equivalents (Figure 4.8 and 4.9). The tapered nitinol rod as the inner conductor provided a smooth transition between the coaxial shaft and the whip. A pigtail catheter was straightened and a broad selection of catheters was delivered over the proposed design without its MRI visibility performance is being affected (Figures 4.6, 4.7 and 4.4.10). Various guidewires with varying mechanical properties are used for each specific application in clinics. Here, we aim to propose a one-for-all design to cover a wide range of clinical applications and meet an urgent need in the iMRI field. Hence, the component dimensions were chosen for a slightly higher stiffness. However, those dimensions can be altered considering the electrical characteristics to obtain desired mechanical characteristics for specific applications in mind.

The proposed design was clearly visible during in-vivo real-time MRI. The unique curved tip geometry with continuous tip visibility allowed access to left ventricle through the aortic arch (Figure 4.10). The AGW visibility was not affected by the changing orientation with respect to B_0. The detachable electrical connector in combination with 162.5 cm device length allowed intra-operational delivery and exchange

of cardiovascular catheters over the AGW prototype (Figure 4.6). The continuous tip signal allowed the determination of the AGW rotation in the inferior vena cava (Figure 4.7).

Clinical grade devices require the use of biocompatible materials for device fabrication, and their safety and efficacy need to be confirmed through appropriate clinical trials and regulatory approvals for direct clinical use. A well-established manufacturing and quality control pipeline which is well beyond the capacity of a research lab, is required to manufacture a large number of device samples required for regulatory approval tests. For this reason, an industrial partner was contracted for bigger scale manufacturing of the proposed design and the clinical evaluation is expected within a year.

4.5 Conclusion

In this work, a novel, actively visualized metallic guidewire with 0.89 mm (0.035") OD and 162.5 cm length, a unique curved tip geometry and a detachable electrical connector was introduced for high performance human cardiovascular catheterization at 0.55T. The proposed design was clearly visible both in-vitro and in-vivo during real-time MRI providing a full shaft and continuous tip visibility. The RF-induced heating performance of the AGW prototype was considered safe for clinical applications. The mechanical performance of the proposed design was comparable to the commercially available equivalents. The detachable connector with 162.5 cm device length allowed delivery and exchange of a broad selection cardiovascular catheters. This novel design will enable a wide range of MRI guided cardiovascular interventions at 0.55T.

5. A CARDIOVASCULAR MAGNETIC RESONANCE (CMR) SAFE METAL BRAIDED CATHETER DESIGN FOR INTERVENTIONAL CMR AT 1.5 T.

5.1 Introduction

MRI catheterization is an attractive strategy because it avoids ionizing radiation and affords superior soft tissue contrast in arbitrary imaging planes, in real-time, at speeds up to 10 frames per second [3,33,40,217,218]. Clinical adoption of MRI catheterization remains limited because clinical grade MR-compatible devices, e.g. guidewires and catheters, are currently not available for safe and effective catheter procedures in patients [34, 55, 219]. Limited diagnostic and therapeutic MRI catheterization procedures have been embraced by a handful of clinical centers by using either MR compatible commercially available devices or clinical grade MR-conditional device prototypes or both [220, 221]. MR catheter devices typically omit metallic components to reduce image distortion and enhance MRI compatibility and RF safety [197]. However, non-metallic components reduces the overall mechanical performance of the medical devices adversely [222, 223], and limits their suitability for interventional procedures.

Ideally, an MRI-compatible catheter must have a comparable mechanical performance to commercially available devices designed to perform a similar procedure under fluoroscopy. Commercial catheters incorporate metal braids or coils along the shaft to impart torque response, push-ability and kink resistance. However, such designs are intrinsically susceptible to radiofrequency (RF)-induced heating under MR, risking thermal injury [128, 223–225]. Replacing metal wires with polymer fibers in braiding layer avoids RF-induced heating, however results in inferior mechanical, hence operational, performance during MRI catheterization [222]. However, if the electrical length of each metal component used in catheter construction is restricted to be less than a quarter-wavelength at a specified electromagnetic field, standing wave formation thus RF-induced heating can be reduced or eliminated [128, 224, 225]. At 1.5 Tesla (T), a

quarter wavelength within the body is approximately 12 cm [127]. In a previous work it was demonstrated that MR-safe guidewires can be constructed using by mechanically joining but electrically isolating quarter-wavelength metallic segments [226]. Here, we demonstrate an MR safe full metal braided catheter design by segmenting each individual braid wire such a way that the electrical continuity is disrupted every 10 cm along the wire while maintaining circumferential braid continuity over the whole shaft. This allows standard commercial manufacturing procedures to be largely preserved in building MRI safe metallic braided catheters.

5.2 Methods

Electromagnetic simulations were performed to study electric field (E-field) coupling performance of individually segmented metallic braiding wires. We compared heating, in-vitro and in-vivo imaging and mechanical performance of conventional braided steel catheter shaft subassemblies with segmented variants described below. These used commercial clinical grade components assembled in our laboratory. A key difference between our subassemblies and standard commercial clinical subassemblies is that we used electrically insulated steel wires for construction, so crossed braiding wires would not create short-circuits. As there is no commercially available MRI compatible metal braided catheter, we compared mechanical properties of in-house developed prototypes with a commercially available but not MRI compatible metal braided catheter (6F Supertorque Angiographic Catheter, Cordis Cardinal Health, Miami Lakes, FL).

5.2.1 Electromagnetic field simulations

Electromagnetic simulations of the non-segmented and segmented metal braiding designs were performed using a finite elements method solver (Comsol 5.2a, RF Module, Stockholm, Sweden). Since the braiding patter is too complex to model using Comsol computer aided design (CAD) module, both designs were 3D-modelled using Solidworks 2019 (Dassault Systems, MA) (Figure 5.1).

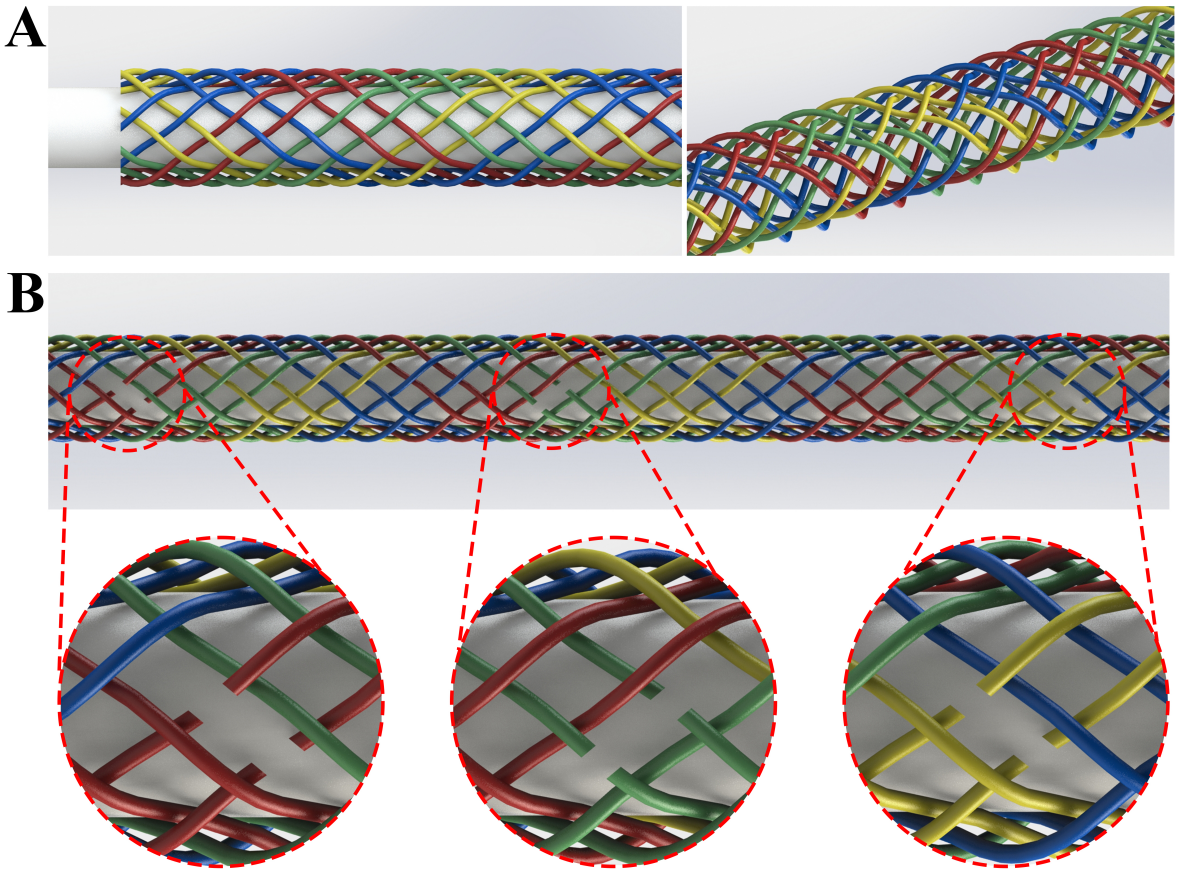


Figure 5.1 3D model of the (A) non-segmented and (B) segmented full load braiding pattern (two over, two under). Braiding wires are colored for the ease of visual tracking. Same color wire pairs are laser-cut in-situ at each segmentation step.

In this study, the full braid pattern (two-over-two-under) was used since it is to most commonly used pattern in the medical device industry. The full load braid pattern can be mathematically modelled [227].Cartesian coordinates of the braiding wires rotating in counter-clockwise direction can be calculated using the following equations:

$$r(\theta) = \begin{cases} \frac{a}{2} & ;0 < \theta < k_1\beta/2 \\ \frac{a}{2}\ sin(\frac{2\pi}{\beta}\theta + \frac{\pi}{2}) & ;k_1\beta/2 < \theta < (k_1+1)\beta/2 \\ -\frac{a}{2} & ;(k_1+1)\beta/2 < \theta < (2k_1+1)\beta/2 \\ \frac{a}{2}\ sin(\frac{2\pi}{\beta}\theta + \frac{\pi}{2}) & ;(2k_1+1)\beta/2 < \theta < (k_1+1)\beta/2 \end{cases} \tag{5.1}$$

$$r_0 = \frac{2(p+p')cos\alpha}{\beta} \tag{5.2}$$

$$X_i = (r_0 + r(\theta))\ \cos(\theta + (i-1)\beta),\ i = 1, 2 \ldots n \tag{5.3}$$

$$Y_i = (r_0 + r\,(\theta))\sin\,(\theta + (i-1)\,\beta),\ i = 1, 2 \ldots\ n \tag{5.4}$$

$$Z_i = r_0 \tan(\alpha\beta),\ i = 1, 2 \ldots\ n \tag{5.5}$$

Similarly, cartesian coordinates of the braiding wires rotating in clock-wise direction can be calculated using the following equations:

$$r(\theta) = \begin{cases} -\dfrac{a}{2} & ; 0 < \theta < k_1\beta/2 \\ \dfrac{a}{2}\ sin(\dfrac{2\pi}{\beta}\theta + \dfrac{\pi}{2}) & ; k_1\beta/2 < \theta < (k_1+1)\beta/2 \\ \dfrac{a}{2} & ; (k_1+1)\beta/2 < \theta < (2k_1+1)\beta/2 \\ \dfrac{a}{2}\ sin(\dfrac{2\pi}{\beta}\theta + \dfrac{\pi}{2}) & ; (2k_1+1)\beta/2 < \theta < (k_1+1)\beta/2 \end{cases} \tag{5.6}$$

$$r_0 = \frac{2(p+p')cos\alpha}{\beta} \tag{5.7}$$

$$X_i = (r_0 + r(\theta))\ \cos(-\theta - (i-1)\beta),\ i = 1, 2 \ldots n \tag{5.8}$$

$$Y_i = (r_0 + r\,(\theta))\sin\,(-\theta - (i-1)\,\beta),\ i = 1, 2 \ldots\ n \tag{5.9}$$

$$Z_i = r_0 \tan(\alpha\beta),\ i = 1, 2 \ldots\ n \tag{5.10}$$

where p is the length of the crossover region in the crimp path, p' is the length of the undulation region in the crimp path, a is the minor diameter of the yarn cross-section, k_1 is the coefficient between p and p', r_0 is the radius of the tubular braid, $r(\theta)$ is the crimp of braiding wire as a sine wave, β is the shift angle between the braiding wires moving in the same direction, α is the braiding angle with the horizontal axes, n is the

number of the braiding yarns revolving in the same direction, i is the counter defining the actual braiding yarn revolving in the same direction and θ is the wrapping angle ($0 < \theta < 2\pi$) [227].

Metal braiding wire was defined as 316 stainless steel and encapsulated in a polymer volume with relative permittivity of 3.2 and electrical conductivity of 0 S/m, mimicking the Pebax hypotube used for the actual prototype fabrication. Whole simulation volume was defined as a liquid material with relative permittivity of 78 and electrical conductivity of 0.47 S/m, mimicking the average human body loading conditions. The simulation volume boundaries were defined as perfectly matched layers so that the scattered electromagnetic field is totally absorbed. Whole simulation volume was excited with 1 V/m linearly polarized electric field tangential to the metal braiding to maximize the E-field coupling. E-field values at the ends of the metal braiding and individual braiding wire segments were plotted to assess the effects of the segmentation.

In this study, the full braid pattern was modeled and simulated. However, the diamond patter (one-over-one-under) which is also used regularly in the medical device industry, can be also mathematically modeled and simulated with the same approach. Cartesian coordinates of braiding wires of a diamond pattern rotating in counter-clockwise direction can be calculated using the following equations:

$$r_0 = \frac{2\ p\ cos\alpha}{\beta} \tag{5.11}$$

$$r\left(\theta\right) = \frac{a}{2}\sin\left(\frac{2\pi}{\beta}\theta + \frac{\pi}{2}\right) \tag{5.12}$$

$$X_i = \left(r_0 + r(\theta)\right)\ \cos(\theta + (i-1)\beta),\ i = 1, 2 \ldots n \tag{5.13}$$

$$Y_i = \left(r_0 + r\left(\theta\right)\right)\sin\left(\theta + \left(i-1\right)\beta\right),\ i = 1, 2 \ldots\ n \tag{5.14}$$

$$Z_i = r_0 \tan(\alpha\beta),\ i = 1, 2 \ldots\ ni = 1, 2 \ldots\ n \tag{5.15}$$

Similarly, cartesian coordinates of the braiding wires rotating in the clock-wise direction can be calculated using the following equations:

$$r_0 = \frac{2\ p\ cos\alpha}{\beta} \tag{5.16}$$

$$r\left(\theta\right) = \frac{a}{2}\sin\left(\frac{2\pi}{\beta}\theta + \frac{\pi}{2}\right) \tag{5.17}$$

$$X_i = \left(r_0 + r(\theta)\right)\ \cos(-\theta - (i-1)\beta),\ i = 1, 2 \ldots n \tag{5.18}$$

$$Y_i = \left(r_0 + r\left(\theta\right)\right)\sin\left(-\theta - \left(i-1\right)\beta\right),\ i = 1, 2 \ldots\ n \tag{5.19}$$

$$Z_i = r_0 \tan(\alpha\beta),\ i = 1, 2 \ldots\ ni = 1, 2 \ldots\ n \tag{5.20}$$

where p is the length of the crossover region in the crimp path, a is the minor diameter of the yarn cross-section, r_0 is the radius of the tubular braid, $r(\theta)$ is the crimp of braiding wire as a sine wave, β is the shift angle between the braiding wires moving in the same direction, α is the braiding angle with the horizontal axes, n is the number of the braiding yarns revolving in the same direction, i is the counter defining the actual braiding yarn revolving in the same direction and θ is the wrapping angle ($0 < \theta < 2\pi$).

5.2.2 Prototype construction

We first constructed a 6 French (Fr) stainless steel braided catheter prototype. A full load braid pattern was formed in a standard vertical braider (K80/16, Steeger Inc., SC, USA) by using perfluoroalkoxyalkane (PFA)-insulated 316L stainless steel wires (0.008" diameter bare wire insulated with 0.001" thick PFA polymer layer, A-M Systems, WA, USA). A polytetrafluoroethylene (PTFE) lined blue color thermoplastic polymer tubing with 0.080" inner diameter (ID) and 0.096" outer diameter (OD) (72D Pebax, Zeus Inc., NJ, USA) was used as the inner layer of the catheter. Insulated stainless steel wires were braided over the inner Pebax layer using 10 pitch per inch

(PPI) and 50 rpm table speed settings. Another clear Pebax polymer layer was applied on top of the assembly as the outer layer. Both Pebax layers were reflowed by heating (Model 210-A, BEAHM Design Inc., CA, USA) so that the metal braiding layer was embedded between two layers (Figure 5.2).

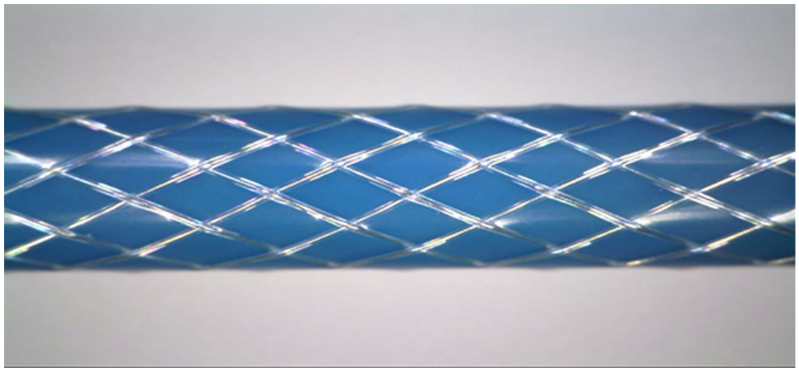


Figure 5.2 Embedded braiding layer between two Pebax layers after reflowing process.

The length of individual braiding wires can be calculated with the line integral of the formulations introduced above. Alternatively, the braiding pattern can be virtually unwrapped to a 2D shape and geometric calculations can be performed on the 2D pattern. In our selected braiding pattern, a pair of interweaved wires completes its 360-degree rotation and interweaves again, after 9 nodes (spots where the wires cross). The linear length (LL) of a single wire after a 360-degree rotation can be calculated using the Pythagorean theorem (Eq 5.21).

$$LL = \sqrt{LD^2 + PC^2} \tag{5.21}$$

where LD is the distance on horizontal axis after a 360-degree rotation and the PC is the perimeter of the catheter tube (braiding wire diameter is ignored). LD can be calculated using Eq. 5.22,

$$LD = 8 \cdot NN \tag{5.22}$$

where NN is the horizontal node-to-node distance of the braiding.

NN was measured as 1.35 mm and linear length of the wire was calculated as 1.28

cm. Every braiding wire was cut in 10.24 cm intervals using a 1064 nm Nd:YAG laser system (Lasag Inc., Switzerland) to process all wires in less than a quarter wavelength and eliminate RF-induced heating (Figure 5.3). At each segmentation point along the catheter, laser cutting was done on a pair of adjacent wires (two wires out of 16 wires each time) as shown in Figure 5.3. By following this segmentation pattern, electrical continuity of each braiding wire was interrupted at less than a quarter wave-length while sustaining a continuous braid structure.

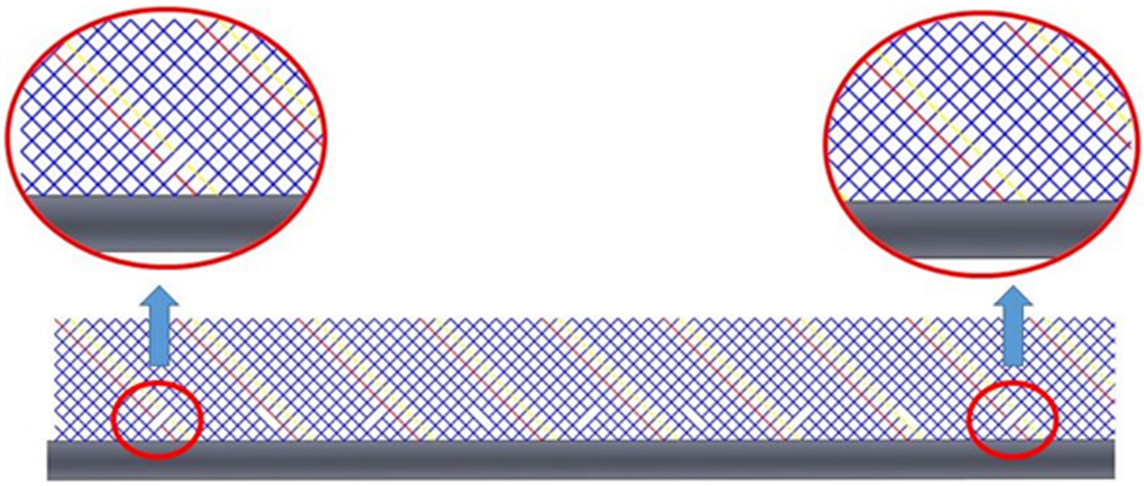


Figure 5.3 Schematic of a full-cycle braiding segmentation pattern. Breaks on the braid pattern can be seen by following the red and yellow lines. The pattern is shown in 2D, representing the unwrapped form of the catheter shaft.

The biggest differences between the materials used in the catheters we designed and commercial braided catheters include the use of PFA polymer for insulation and the choice of 316L stainless steel. PFA polymer was used for electrical isolation of crossing braiding wires, a must to prevent short circuits. We chose 316L surgical stainless steel as the braiding wire because it creates a modest susceptibility artifact compared with the common alternative 304 stainless steel. Compared with current commercial braided catheters, we add a single additional manufacturing step consisting of in-situ laser segmentation.

5.2.3 In-vitro characterization tests

Segmented braided catheter prototypes (100 cm long) were compared with equivalent length but non-segmented braided catheter samples in terms of RF-induced heating performance. The segmented and non-segmented catheter prototypes were tested for RF-induced heating per ASTM standard 2182-11a [152] at 1.5 T (Aera, Siemens, Erlangen, Germany) using a balanced steady-state free precession (bSSFP) (TE/TR=1.05/283.63 ms, flip angle=45°, FOV=300 mm, matrix=192x192, slice thickness=10 mm) and a gradient recalled echo (GRE) sequence (TE/TR=2.97/727.72 ms, flip angle=45°, FOV=300 mm, matrix=192x192, slice thickness=10 mm) which are commonly used real-time interventional MRI sequences. Real-time bSSFP was chosen because it is the workhorse pulse sequence used in clinical MRI catheterization, and it has relatively high average SAR values [31, 228]. In addition, we tested high flip angle real-time GRE pulse sequence. A fiberoptic temperature probe (OTG M170, OpSens, Canada) was introduced into a thin-wall polyamide tube affixed to the outer surface of catheter samples. Test samples were placed 3 cm away and parallel to the right edge of the ASTM gel phantom and positioned parallel to the main magnetic field (B_0) (Figure 5.4A and 5.4C). Temperature measurements began with the probe positioned at the distal tip of the catheter, and then retracted along the catheter shaft during continuous scanning to sample all potential "hot spots" along the catheter shafts. Tests were performed during up to 20 minutes of scanning.

MRI visibility performance of segmented and non-segmented braided catheter subassemblies was tested using a standard spin echo (SE) (TE/TR=20/500 ms, flip angle=50°, FOV=300 mm, matrix=192x192, slice thickness=5 mm) and a GRE (TE/TR= 15/500 ms, flip angle=50°, FOV=300 mm, matrix=192x192, slice thickness=5 mm) sequence in a phantom per ASTM standard F2119-07 [153]. Tests samples were positioned 5 cm away from the phantom edges both parallel and perpendicular to the main magnetic field making a 90° curve to assess the effects of the device orientation in the magnetic field on the magnetic susceptibility artifact. A reference object with 25.4mm diameter also placed in the phantom and the size of the magnetic susceptibility artifacts were evaluated according to ASTM standard F2119-07 (Figure 5.4B).

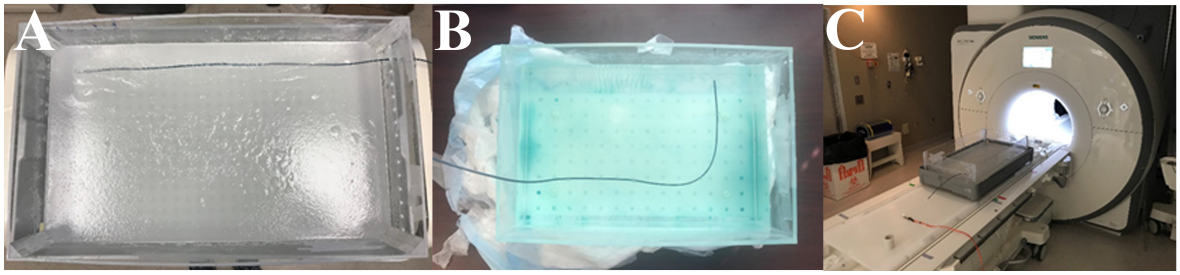


Figure 5.4 (A) Test sample position in the ASTM 2182 gel phantom, (B) in the ASTM 2119 copper sulfate phantom and (C) phantom and sample positions in the scanner.

Torque response, flexibility and push-ability characteristics of the segmented and non-segmented catheter prototypes and commercial comparators were tested to determine whether segmentation compromised mechanical integrity. The flexibility test was conducted using a digital force meter (IMADA Inc., Northbrook, IL) attached to a programmable linear actuator while the catheter sample was attached to a 3-point bending apparatus (Figure 5.5A). The bending properties of segmented and non-segmented braid samples and the commercial catheter were compared by pushing the samples for 15cm and then allowing them to recoil to their initial state (Figure 5.5B). The push-ability test was performed using a dedicated apparatus (IDTE 2000, MSI, AZ, USA) by pushing samples through a 55cm vascular phantom (Figure 5.5C). The load cell connected to the servo motor measured the reaction force during advancement 3 times per sample. The torque response test was conducted placing the catheter samples in an in vitro vessel phantom which mimicked the trajectory of a transfemoral catheter across the ascending aorta and connecting the proximal end to a digital torque meter (IMADA Inc., Northbrook, IL) (Figure 5.5 and 5.5E). The torque response test measured the torque transmitted to the distal end from the proximal end (Figure 5.5D), and the required torque to rotate the distal end 360 degrees (Figure 5.5E). Transmitted rotation was tested 3 times per sample while the required torque for 360-degree rotation was tested 5 times per sample.

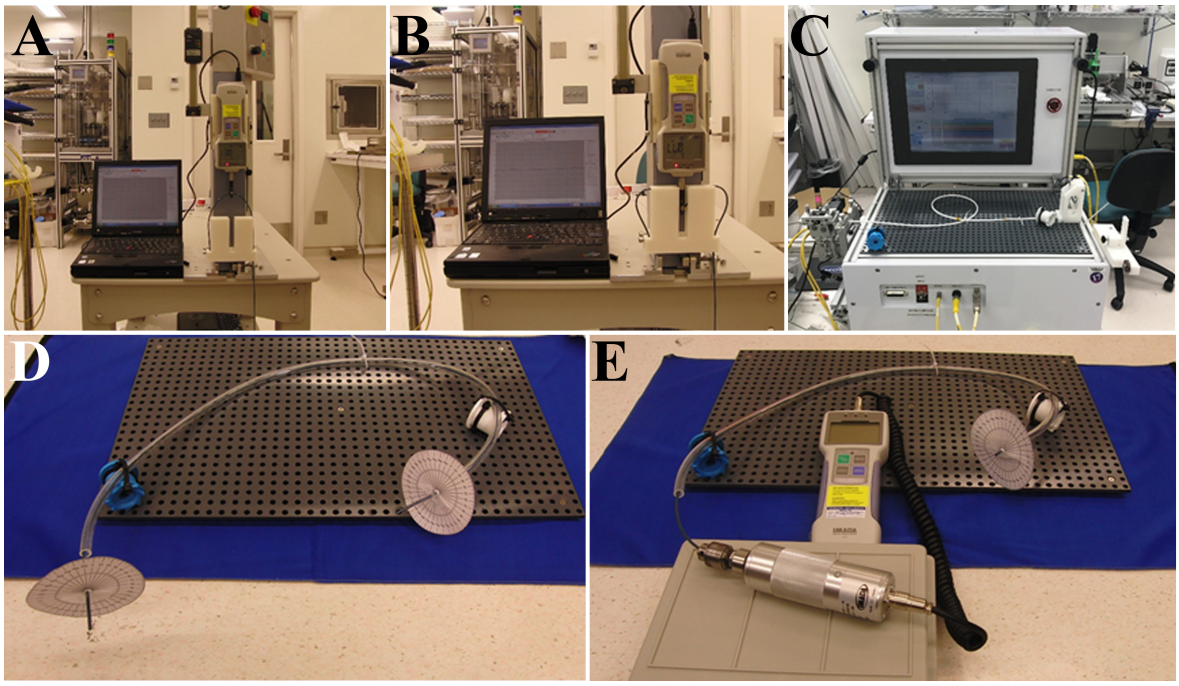


Figure 5.5 (A and B) Flexibility, (C) push-ability and (D) and (E) torque response test setups.

First flexibility and then the push-ability tests were repeated 150 times on the segmented catheter subassembly to evaluate possible effects of a mechanically challenging interventional procedure on the insulation layer integrity. Torque response, flexibility and push-ability tests were repeated after mechanical stress tests. The 21 cm long flex-tested sample was dissected and tested for electrical insulation integrity (Figure 5.6A). Extracted braiding was tested for conductivity (Figure 5.6B) using an electronic multimeter (Fluke 177, WA, USA) and carefully tracing the individual braiding wires, each stress-tested braiding wire was assessed for a possible short circuit between wires.



Figure 5.6 (A) 21 cm long dissected segmented braided catheter subassembly part and (B) detached and scraped braiding wires.

5.3 Results

5.3.1 Electromagnetic field simulations

Figure 5.7 shows the electromagnetic simulation results of the segmented and non-segmented metal braiding samples. E-field amplification is mitigated when the continuous metallic wires are electrically interrupted in less then quarter wavelength. Maximum local E-field values were 0.05 V/m and 50 V/m along the segmented and non-segmented braiding models.

5.3.2 In-vitro characterization tests

Braiding uniformity was confirmed visually all along the catheter shaft for each sample and corroborated by measuring the consistency of node to node distance as 1.35 $\pm$ 0.01 mm (Figure 5.8A) using a light microscope (Hirox KH-1300, Hirox Inc., NJ, USA). Laser, in-situ, interruption was also confirmed visually using the same setup (Figure 5.8B).

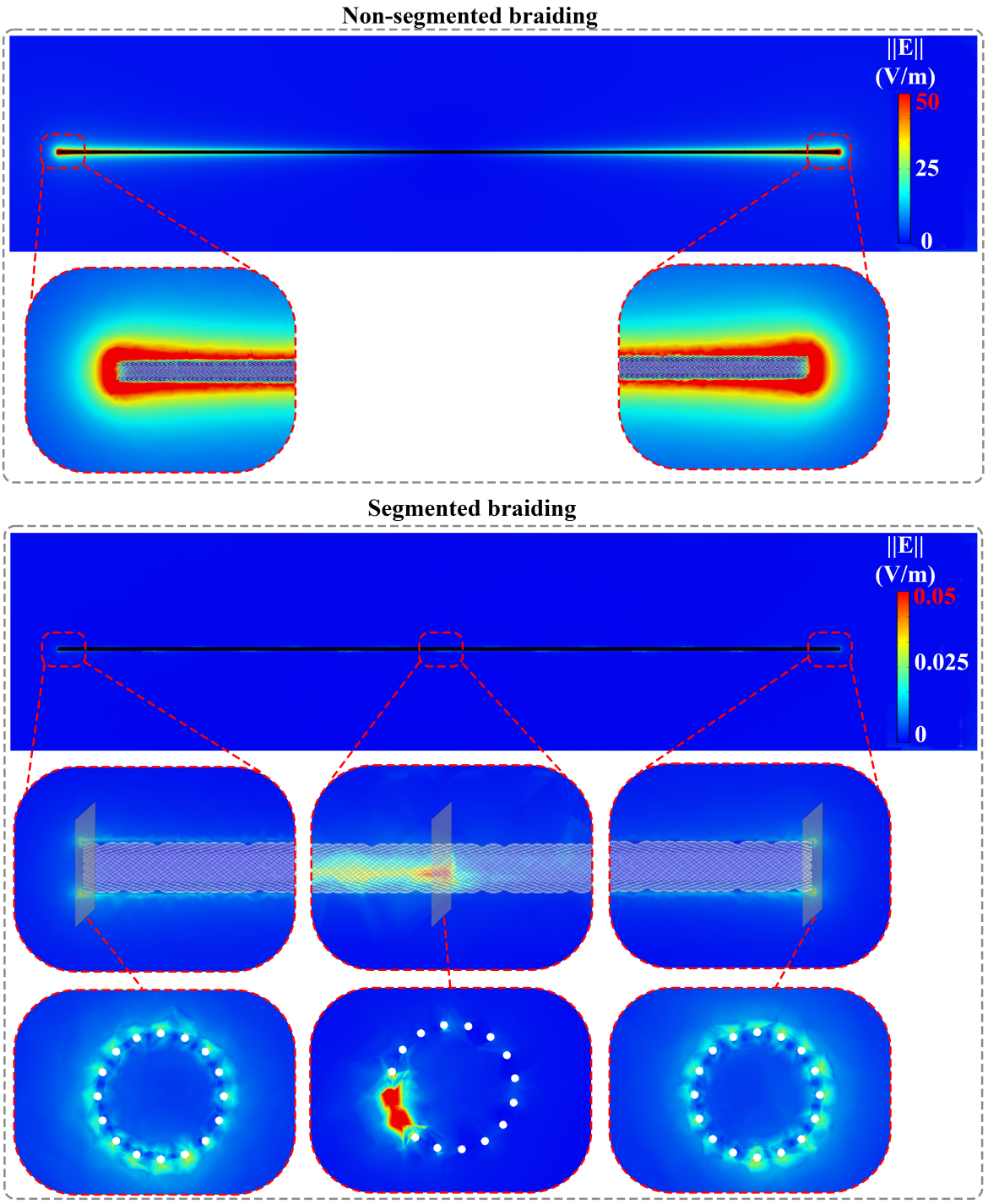


Figure 5.7 Electromagnetic simulation results of the non-segmented and segmented braiding models. E-field concentration at braiding ends is mitigated by electrically interrupting long conductive wires. Maximum E-field concentration occurs at the ends of individual short segments.

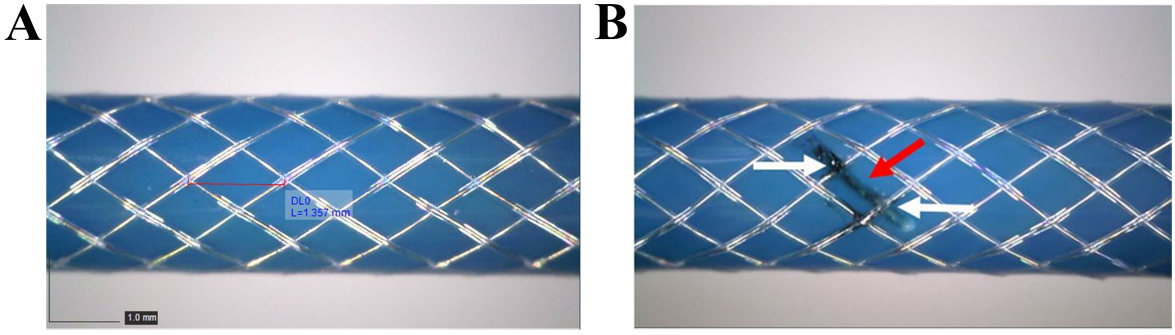


Figure 5.8 (A) Braiding uniformity and the node to node distance were confirmed under light microscope. (B) The segmented braid catheter constructed in-house. The segmentation points on the braiding layer are shown with white arrows (Blue insulation is discolored (red arrow) but not interrupted by the laser in-situ segmentation process).

Segmentation greatly reduced heating under the test conditions (Figure 5.9). Table 5.1 shows the temperature rise at the tip of the segmented- and continuous-braid catheters for bSSFP and GRE MRI scans.

Table 5.1
RF-induced temperature rise at the distal tip.

Sequence Type	**Scan Time**	**Segmented Braiding (Δ°C)**	**Non-segmented Braiding (Δ°C)**
Real-time bSSFP	60 sec	0.78	52.6
Real-time bSSFP	20 min	0.92	54.8
Real-time GRE	60 sec	0.67	13.4
Real-time GRE	20 min	0.82	14.1

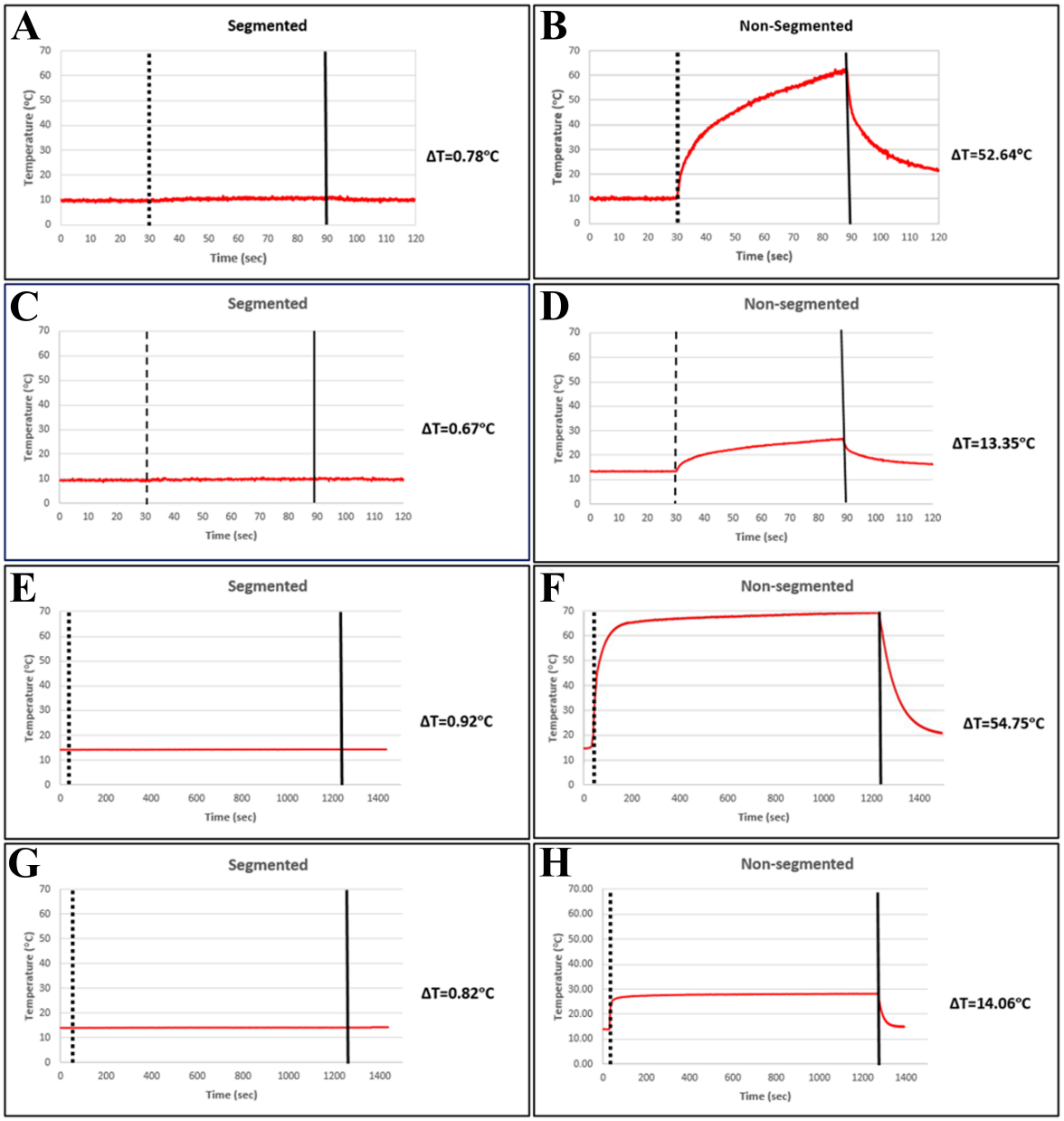


Figure 5.9 RF induced temperature rise of the segmented catheter subassembly after (A) 60 seconds bSSFP, (C) 60 seconds GRE, (E) 20 minutes bSSFP and (G) 20 minutes GRE scans. RF induced temperature rise of the non-segmented catheter subassembly after (B) 60 seconds bSSFP, (D) 60 seconds GRE, (F) 20 minutes bSSFP and (H) 20 minutes GRE scans.

Induced currents on the long conductive wires due to the E-field coupling during the RF excitation cause local flip angle amplifications which lead to artifacts in the close vicinity of the wire due to stimulated echoes. Electrically interrupting long conductive wires minimized the E-field coupling, thus reduced the local flip angle amplification

(bright signal) but did not affect the magnetic susceptibility artifact (signal void). Via spin echo imaging, artifact size as a bright signal was measured as 1.4 mm for segmented and 12.5 mm for non-segmented sample perpendicular to the B_0 and 17.3 mm for non-segmented sample parallel to B_0, on the coronal plane. Using the GRE sequence, when samples were parallel to B_0, the non-segmented sample caused a large blooming artifact while segmented sample did not cause any artifact. Conversely, when the samples were positioned perpendicular to B_0, the artifact size as a signal void was measured as 14.3 mm and 13.2 mm for the segmented and non-segmented samples, respectively (Figure 5.10).

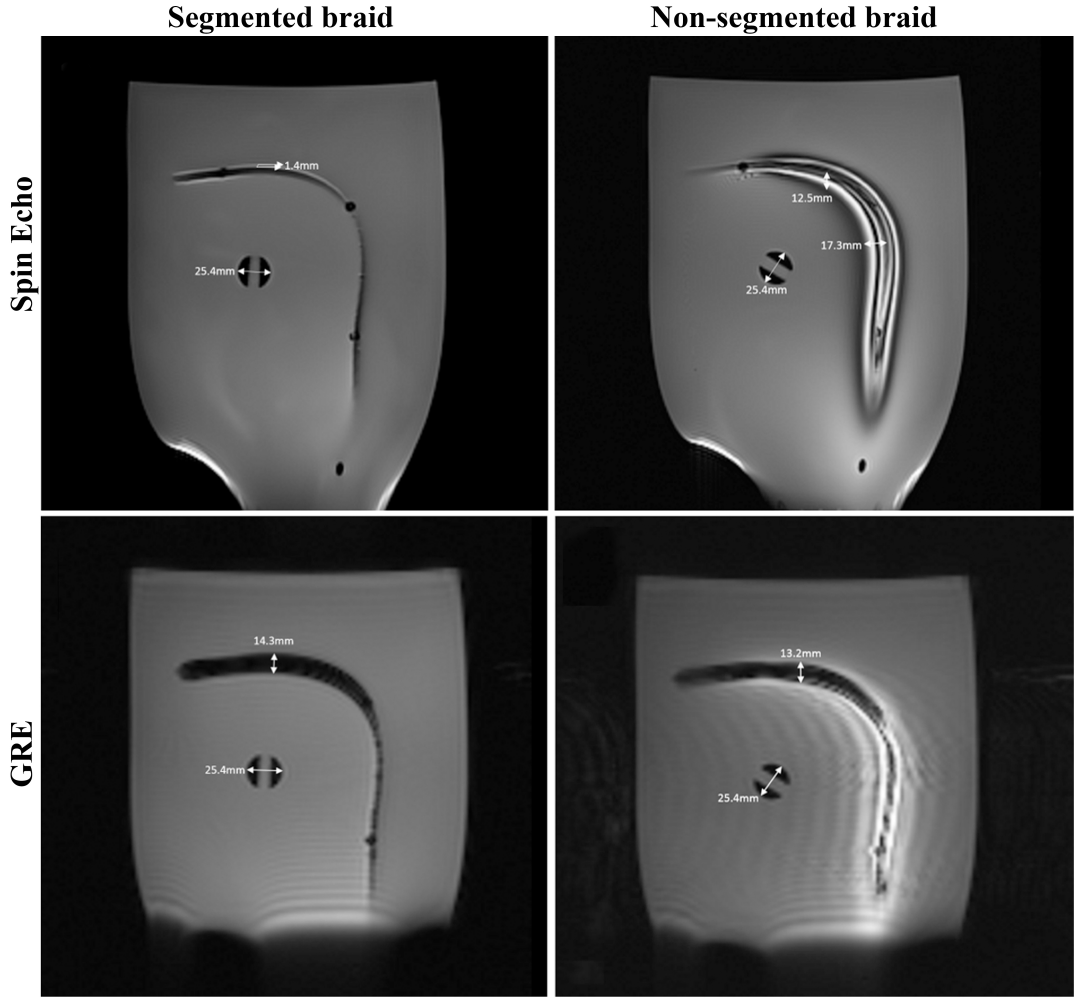


Figure 5.10 In-vitro MR images and susceptibility artifact measurements. Segmentation of metallic braiding wires mitigates the E-field amplification so that the local flip angle amplification using Spin Echo pulse sequences. However, segmentation does not alter the material properties so that the signal void artifact does not change after segmentation.

Segmentation did not significantly alter torque-response. Both segmented and unsegmented catheters transmitted initial applied torque poorly from the proximal end to the distal end until 270-degree rotation, as is typical of commercial clinical devices. However, after the 270-degree rotation, sufficient baseline torque accumulated along the shaft to transmit torque effectively. Figure 5.11 shows the torque transmission test results for segmented and non-segmented braid catheters and the commercial catheter after 3 repetitions. Table 5.2 shows the required torque values for a 360-degree rotation of the distal tip.

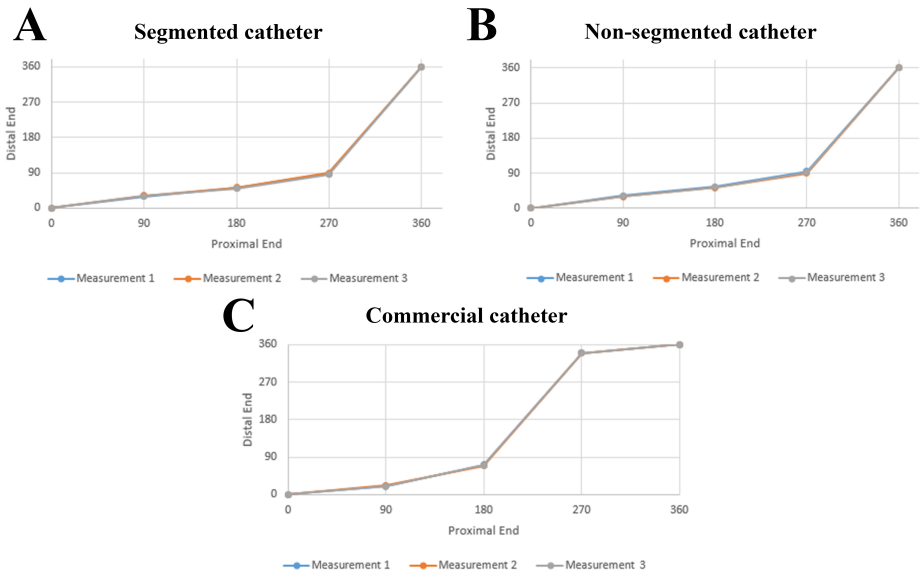


Figure 5.11 Torque transmission test results of (A) segmented, (B) non-segmented braid and (C) commercial catheters.

Table 5.2
Torque requirement for a 360-degree rotation.

Measurement #	Segmented catheter (kgf.cm*)	Non-segmented catheter (kgf.cm*)	Commercial catheter (kgf.cm*)
1	1.03	1.14	1.33
2	1.15	1.09	1.31
3	1.10	0.92	1.34
4	1.01	1.15	1.23
5	0.95	0.86	1.34
Mean	1.05 ± 0.07	1.03 ± 0.12	1.31±0.04

Figure 5.12 shows the bending stiffness of all catheters after the 3-point bending test was performed 3 times for each sample. Kink resistance of segmented catheter shafts are comparable to non-segmented and commercial catheter shafts.

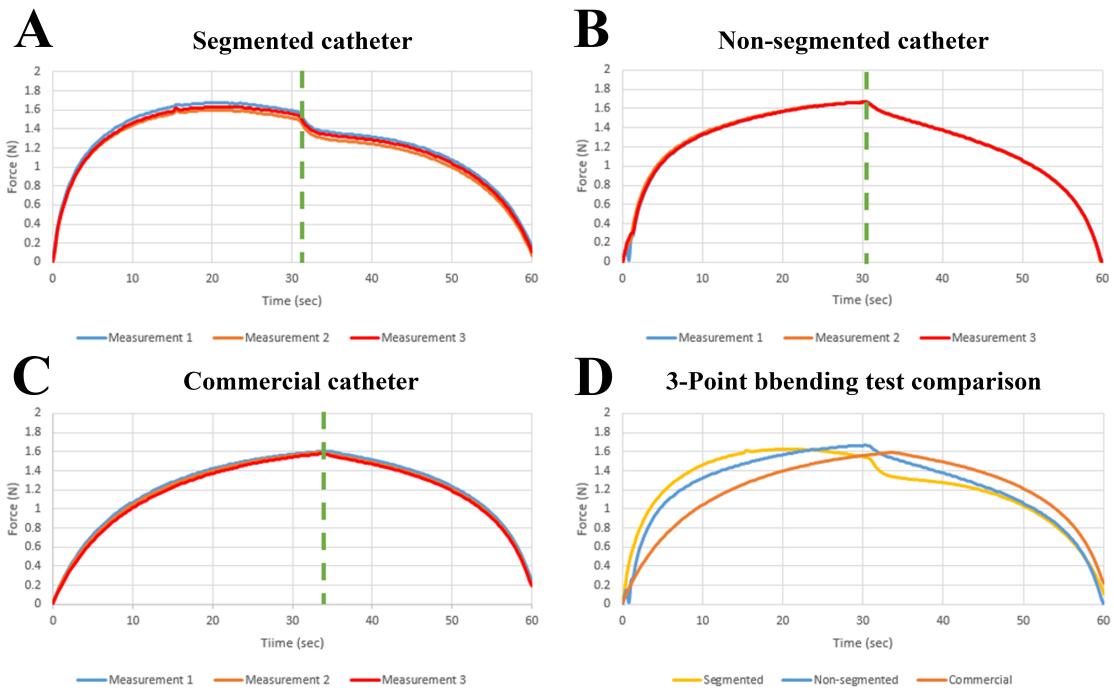


Figure 5.12 Bending stiffness test result of (A) segmented, (B) non-segmented braided and (C) commercial catheters and (D) the test results averages.

Figure 5.13 shows the continuously measured push forces throughout the trajectory after three prior tests per sample. The performance of the segmented samples was comparable to non-segmented samples while that of commercial catheter was better than in-house developed prototypes.

Figure 5.14 shows the flexibility, push-ability and torque response test results before and after the mechanically challenging test. Mechanical performance of the segmented catheter subassembly after the repeating mechanical tests was slightly degraded while electrical insulation remained intact and no short circuit was formed between braiding wires. The required torque for a 360-degree rotation was 1.51 $\pm$ 0.076 kgf.cm.

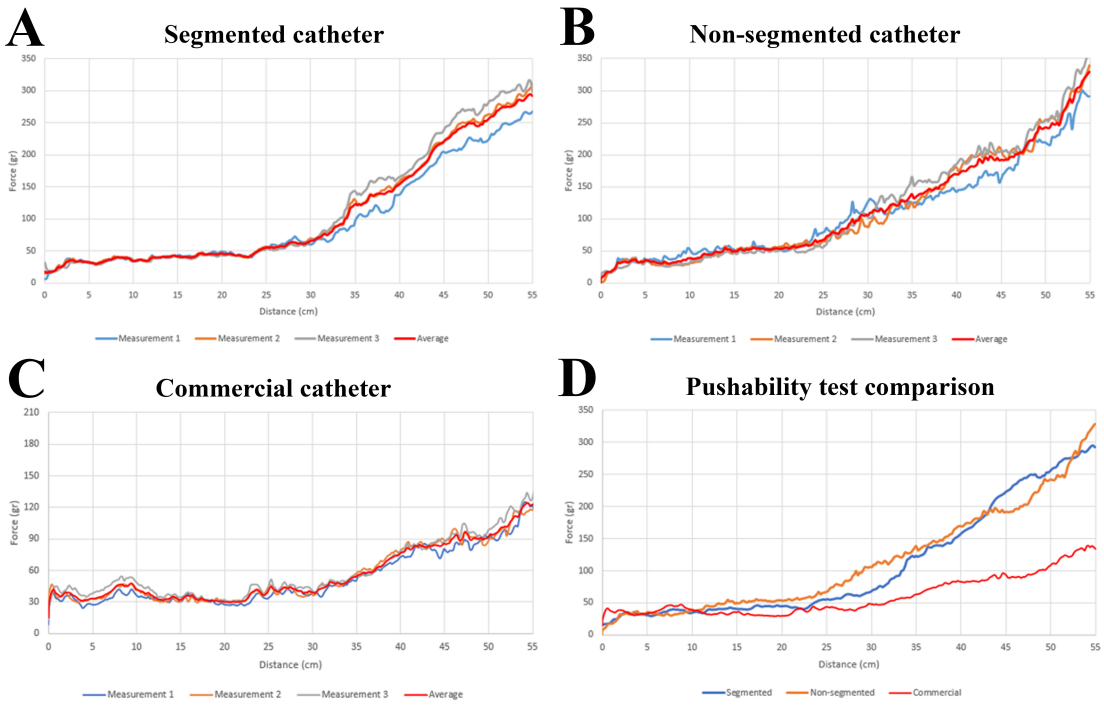


Figure 5.13 Push-ability test results of (A) the segmented catheter sample, (B) the non-segmented catheter sample and (C) the commercial catheter. (D) Comparison of all catheter samples (averaging test results).

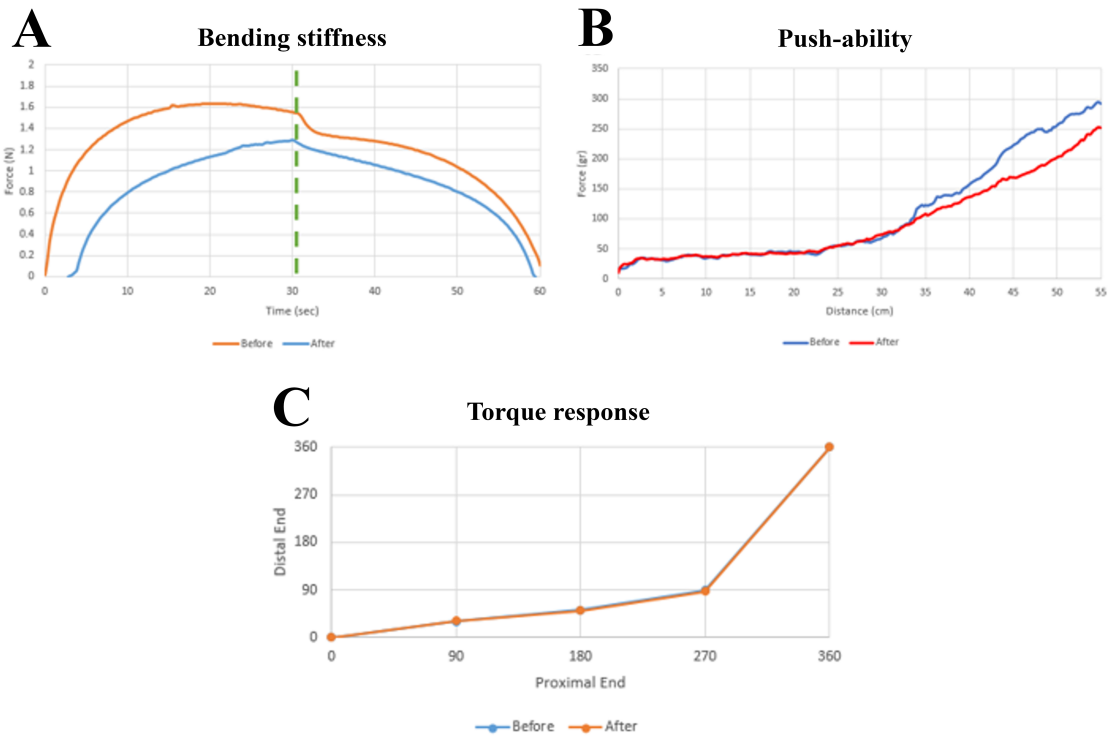


Figure 5.14 (A) Bending stiffness, (B) push-ability and (C) torque response test results of the segmented catheter after the deteriorating mechanical test.

5.3.3 In-vivo characterization tests

Both segmented and non-segmented braided catheter subassemblies were visible in-vivo with a negative contrast during right heart catheterization in the Yorkshire pig, using a real-time bSSFP sequence (Figure 5.15). The physician operator accessed the LV retrograde across the aortic valve in under 10 s from via transfemoral access using both segmented and non-segmented catheters. Both outperformed non-braided catheters and otherwise resembled commercial braided catheters in mechanical behavior.

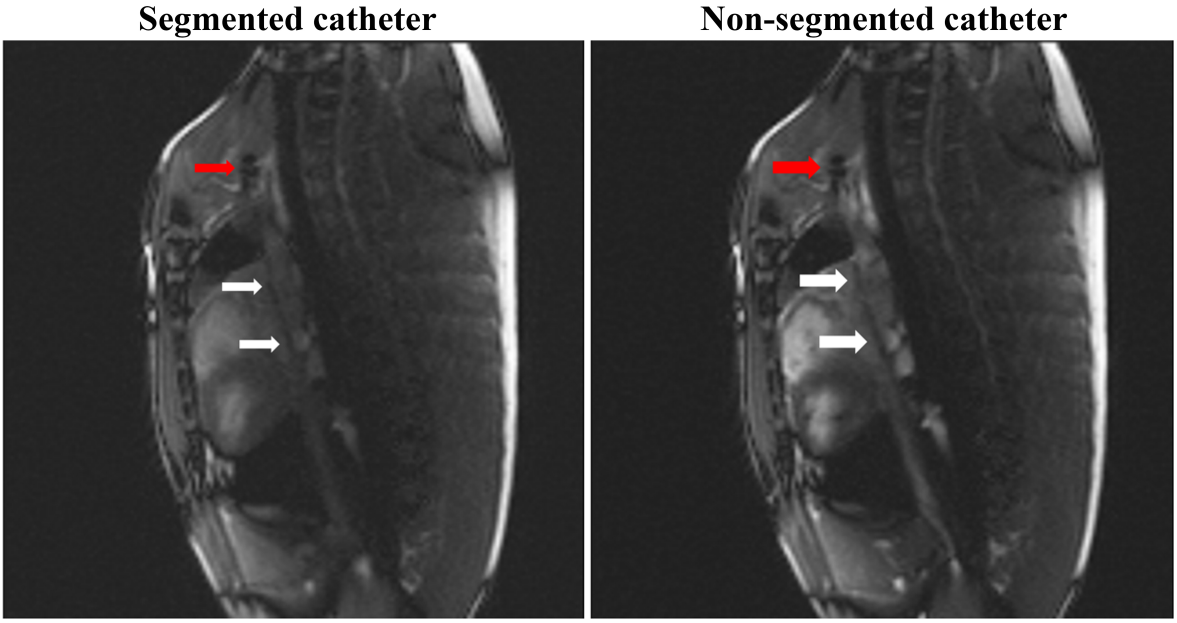


Figure 5.15 In-vivo MR images. Segmented braided and non-segmented braided catheter subassemblies were advanced through the superior vena cava with a custom, iron-oxide coated guidewire in tandem during real-time bSSFP CMR (Red arrows indicate the tip of the custom, iron-oxide coated guidewire prototype, white arrows indicate the segmented and non-segmented catheter subassemblies).

5.4 Discussion

In this study, we show the feasibility of constructing MRI safe catheters that incorporate standard metal braiding into the shaft, a nearly ubiquitous design that imparts push-ability, torque response, and kink-resistance into catheters at low cost.

Electromagnetic simulation results showed that electrically interrupting conductive wires in segments shorter than quarter wavelength enhances RF-safety mitigating the local E-field amplification at braiding ends (Figure 5.7). Maximum local E-field along the segmented braiding was 1000 times lower than non-segmented braiding (0.05 V/m vs 50 V/m) based on the simulation results. Maximum local E-field concentration was observed at the ends of each segment instead of the ends of the whole segmented braiding, as expected. We hypothesize that the same simulation setup can be used to estimate RF-induced heating of the braiding samples using equations Eq 2.1 and Eq 2.2.

A key feature of our design is that component stainless steel wires are individually insulated before braiding. After conventional braiding, the metallic fibers were strategically segmented, in-situ, at quarter-wavelength intervals to disrupt electrical continuity. At the same time, selected interruptions maintained catheter structural integrity and performance. We used transparent outer Pebax, which protected the inner polymer during laser cutting of the insulated wires. The segmentation pattern was selected to limit bidirectional rotation during laser cutting and assured braiding uniformity during manufacture. Benchtop mechanical parameters and catheter tracking in test phantoms were largely unaffected by the segmentation process and were comparable to commercial comparators (Figures 5.11, 5.12 and 5.13).

Non-segmented samples demonstrated a RF-induced temperature increase up to 54.8 ℃ during real-time MRI. After segmenting the embedded braiding wires at quarter-wavelength intervals, the observed temperature increase was reduced to 0.92 ℃ (Figure 55.9, which is clinically insignificant [152].

Thanks to the parametric programmability and repeatability of the process, this fabrication method can be applied to various length and gauge commercially available products using Eq 5.21 and 5.22 and by replacing the bare metal wires with insulated non-magnetic ones during manufacture. The main limitation of our approach is that the braiding layers of conventional commercial braided catheters are typically formed using uninsulated wires. The proposed segmentation process requires compo-

nent wires be insulated before braiding, to prevent wire crossing points from short-circuiting the otherwise electrically-isolated segments. However, the insulation layer thickness is negligible compared to the braiding wire diameter and imparts negligible mechanical change. The use of a polymer insulation layer does require that the process temperatures be kept under the melting temperature of the insulation polymer used. We have demonstrated that wire insulation is not disturbed by thermal reflowing at up to 190 ℃ to embed the braiding between two coaxial Pebax tubes since process temperature remains safely lower than 315 ℃ which is the melting point of the PFA polymer [229].

Both segmented and non-segmented braided catheter subassemblies were conspicuous under MRI in-vivo based on negative contrast (Figure 5.15). Moreover, segmenting the metallic braiding wires shorter than one-quarter wavelength at 1.5T significantly reduced the artifact size caused by local flip angle amplification (Figure 5.10). Even though different steel alloys such as 316LVM would provide satisfactory susceptibility performance, despite segmentation, steel-braided catheters may still cause large magnetic susceptibility artifacts at 1.5T [230], which may require specific materials selection, such as nitinol, titanium [231] or copper, to overcome. Considering the expected mechanical performance and complete MRI compatibility, an insulated nitinol wire would be the strongest candidate to replace stainless steel braiding wire [232].

5.5 Conclusion

RF-induced heating of standard conductive braided catheter designs, to be used in MRI catheterization procedures, was eliminated by laser in-situ segmentation to shorten and electrically isolate braiding wires. It was shown that this process does not alter the essential mechanical properties (push-ability, torque response and kink-resistance) of metal braided catheters. This was achieved by constructing a braid structure using insulated metal wires, and then segmenting it in a strategical pattern in-situ, whereby electrical conduction is disrupted only 2 out of 16 wires at each segmentation location to eliminate RF-induced heating. Therefore, the overall continuity

of the braid structure is preserved to maintain mechanical integrity. This would be an attractive replacement for non-braided and/or non-metallic braided catheters which are inferior to their metallic counterparts.

6. GENERAL CONCLUSION AND FUTURE WORK

In this thesis study, the conductive ink printing method which was introduced by our group earlier was improved by incorporating biocompatible heat shrink polyester hypotubes and implementing closed-loop PID control for the conductive ink injection. PID control enabled fine printing of desired electronic component geometries in addition to the adjustment of component futures during fabrication. This flow control technique can also be easily implemented to micro-fluidic applications. The use of heat shrink hypotubes provides many advantages. RF antenna and transmission line components can be printed on a separate and bigger scale substrate and then the printed components can be transferred onto the actual device geometry. This enables fabrication for complex device geometries which is extremely difficult using conventional fabrication methods. Medical grade device fabrication capabilities of the proposed method were shown with the active iMRI needle prototype. Thanks to the flexible nature of both polyester hypotubes and conductive ink, fabrication for flexible devices are enabled. In-vitro MRI performance of the active iMRI needle during exaggerated deflection tests showed that the MRI visibility of the conductive ink printed RF antenna is not effected by the flexure of the device body. The relatively high intrinsic resistance of the conductive ink itself limits the induced currents on the printed parts and reduces the impedance mismatch between tissues and printed conductors, hence improves the RF safety of iMRI devices. Numerous MRI-safe conventional interventional devices in the market cannot be used for iMRI because of the insufficient device conspicuity under MRI. We hypothesize that active iMRI device parts can be printed on heat shrink hypotubes independently from the actual commercial device geometry and then can be transferred onto virtually any tubular MRI-safe interventional device to provide visibility under MRI enabling the use of MRI these devices for iMRI. Proposed fabrication method can be used for field strength agnostic passive, semi-active or active visualization of the commercially available MRI-safe interventional tools, selecting appropriate print materials.

The importance and use of computational modelling in medicine has been increasing with the developments in the computational technology. Similarly, electromagnetic simulation tools have been heavily used in MRI field to design and characterize RF coils, magnets, gradient coils and implantable devices. Measurement of local in-vivo electromagnetic fields has a great importance to assess RF safety of iMRI devices. However, experimental measurement of such fields is not feasible and electromagnetic simulations are relied on for this purpose. Recently, regulatory standards have mandated the use of such tools for the complete assessment of the RF safety of iMRI devices and implants. We have successfully established accurate electromagnetic simulation setups using most popular FEM (COMSOL) and FDTD (Sim4Life) solvers to optimize the MRI visibility and assess the RF safety of iMRI device designs. Experimental iteration of the RF antenna designs for the optimal MRI visibility is a costly process. We have shown that the optimization of RF receiver antenna parameters can be performed using our simulation approach. It can be anticipated that the transfer function method so that the ISO/TS 10974 standard will be the gold standard for the RF safety assessment of iMRI devices superseding ASTM 2182 standard in the near future. Since our simulation setups are validated with experimental findings, we expect to use our well-established simulation approaches to implement ISO/TS 10974 test methods with confidence.

Needles are used for various purposes as a very fundamental tool in the interventional medicine. In this thesis study we introduced an active needle design with submillimeter outer diameter (0.87 mm) which has not been introduced before. The conductive ink printed RF antenna parts had a modest impact on the needle profile and were undetectable with haptic means. MRI visibility performance of the conductive ink printed antenna was comparable to insulated copper wire antenna as the RF-induced heating performance outperformed the insulated copper wire antenna to a great extent. The mechanical performance of the proposed active needle design was comparable to commonly used, commercially available MRI-conditional needles. As a result, an in-vivo liver intervention was successfully performed using the proposed design.

Guidewires are workhorse tools for the interventional cardiology. They are used to access specific heart chambers by navigating through narrow vasculature, and to deliver and/or exchange other interventional devices (e.g. catheters) for diagnostic or therapeutic purposes. We have successfully introduced an actively visualized, monopole antenna-based metallic guidewire with 0.035" outer diameter and a unique, atraumatic curved tip which has not been introduced before. The unique tip coil configuration provided continuous tip and whole shaft visibility under MRI. The curved tip geometry allowed navigation through cardiovascular system eliminating the perforation risk. Most importantly, the detachable RF connector of the proposed design allowed catheter delivery and exchange over the active guidewire prototype. A clinically acceptable mechanical performance cannot be provided with non-metallic guidewire designs. On the other hand, such a long metallic structure is prone to RF induced heating during real-time MRI. The RF-induced heating performance of the proposed design was clinically acceptable thanks to the active detuning and benefits of the high performance low-field MRI technology. The mechanical performance of the proposed active guidewire design was comparable to the most commonly used commercial, fluoroscopic equivalents. The proposed design is intended to be used for actual human catheterization applications and the human clinical evaluation is expected within a year after regulatory approval tests.

Similar to guidewires, catheters are also fundamental tools for interventional cardiology for diagnosis or therapy delivery. Since, catheters are thin-wall hallow tubes, required mechanical performance cannot be provided using only non-metallic components for guiding catheters. The most common application in the medical device industry is to reinforce the catheter shaft with a metal braiding to provide required mechanical performance. However, the elongated metallic wires used for the braiding is prone to RF-induced heating. We have successfully introduced a MRI-safe metal braided catheter design to address this problem. The strategical segmentation of the individually insulated braiding wires shorter than the quarter wavelength eliminated the RF-induced heating risk without compromising the mechanical performance. The proposed segmentation strategy can be used for the most commonly used braiding patterns (full load and diamond) in the medical device industry.

Interventional cardiology has been targeting increasingly more complex pathologies as the new interventional methods are developed. However, all these innovative methods are pushing the limits of X-Ray guidance requiring additional guiding modalities during procedures. Even though interventional MRI is the strongest candidate as the X-Ray alternative for the guidance of minimally-invasive procedures, human iMRI applications have been very limited due to the lack of dedicated clinical grade, MRI-compatible interventional tools. Despite the limited availability of clinical grade tools, the number of centers performing iMRI procedures have increased over the last decade. Especially with the introduction of the high-performance low-field MRI technology, the variety of iMRI applications and the number of iMRI centers are expected to increase even more in the near future. In this thesis study, we have introduced a modified fabrication method for iMRI device development and established accurate simulation setups to design iMRI devices. We have successfully introduced the most fundamental "safe-by-design" devices for interventional cardiovascular MRI including a 20 G active needle, a 0.035" outer diameter active guidewire and a 6 Fr metal braided guiding catheter using the proposed fabrication method and simulation approaches. We targeted the most fundamental interventional tools to answer to the most urgent need in the iMRI field and to enable a wide range of applications including diagnostic catheterization and therapy delivery for structural, congenital and pediatric interventions under MRI guidance. We hypothesize that the combination of the proposed fabrication method, simulation approaches and iMRI device designs could be used as a secure platform to build novel, application specific safe-by-design iMRI devices on, and the variety of clinical grade iMRI devices can be expanded rapidly in the near future.

7. APPENDIX A: Publications

Journal Publications

First author

1. Yildirim DK, Basar B, Campbell-Washburn AE, Herzka DA, Kocaturk O* and Lederman RJ*, "A cardiovascular magnetic resonance (CMR) safe metal braided catheter design for interventional CMR at 1.5 T: freedom from radiofrequency induced heating and preserved mechanical performance", J Cardiovasc Magn Reason (JCMR) 21, 16, 2019. ***Equal contribution.**

2. Yildirim DK, Bruce CG, Uzun D, Rogers T, O'Brien KJ, Ramasawmy R, Campbell-Washburn AE, Herzka DA, Lederman RJ, Kocaturk O. A 20-gauge active needle design with thin-film printed circuitry for interventional MRI at 0.55 T. Magn Reson Med (MRM), 86: 1786-1801, 2021.

3. Yildirim DK, Uzun D, Bruce, CG, Rogers T, Herzka DA, Lederman RJ, Kocaturk O. A novel active guidewire design with a curved tip geometry for interventional MRI applications under 0.55T. In progress for Magn. Reason. Med. (MRM)

Not first author

1. Baysoy E, Yildirim DK, Ozsoy C, Mutlu S, Kocaturk O, "Thin Film Based Active Resonant Marker Design for Low Profile Interventional Cardiovascular MRI Devices", MAGMA, 2017 Feb;30(1):93-101.

2. Khan JM, Rogers T, Greenbaum AB, Babaliaros VC, Yildirim DK, Bruce CG, Herzka DA, Schenke WH, Ratnayaka K, Lederman RJ. Transcatheter Electrosurgery: JACC State-of-the-Art Review. J Am Coll Cardiol. 2020 Mar 31;75(12):1455-1470.

3. Yaras YS, Yildirim DK, Kocaturk O, Degertekin FL. Sensitivity and phase response of FBG based acousto-optic sensors for real-time MRI applications. OSA Contin. 2020;3(3):447-458.

4. Yaras YS, Yildirim DK, Herzka DA, Rogers T, Campbell-Washburn AE, Lederman RJ, Degertekin FL, Kocaturk O. Real-time device tracking under MRI using an acousto-optic active marker. Magn Reson Med (MRM). 2021; 85: 2904– 2914.

5. Basar B, Sonmez M, Yildirim DK, Paul R, Herzka DA, Kocaturk O, Lederman RJ, Campbell-Washburn AE. Susceptibility artifacts from metallic markers and cardiac catheterization devices on a high-performance 0.55 T MRI system. Magn Reason Imag. 2021; 77: 14-20.

6. Kolandaivelu A, Bruce CG, Ramasawmy R, Yildirim DK, O'Brien KJ, Schenke WH, Rogers T, Campbell-Washburn AE, Lederman RJ, Herzka DA. Native contrast visualization and tissue characterization of myocardial radiofrequency ablation and acetic acid chemoablation lesions at 0.55 T. Journal of Cardiovascular Magnetic Resonance 23 (1), 1-18.

7. Mahcicek ID, Yildirim DK, Kasaci G, Kocaturk O. Preliminary Evaluation of Hydraulic Needle Delivery System for MRI Guided Prostate Biopsy Procedures. ASME. J. Med. Devices. 2021.

International Conference Proceedings

1. Yildirim DK, Baysoy E, Sagiroglu Z, Özsoy C, Kocatürk O, and Mutlu S, "A Novel method for developing clinical grade active devices dedicated to interventional MRI procedures", The International Society for Magnetic Resonance in Medicine (ISMRM) 24th Annual Meeting & Exhibition, Singapore, 07-13 May 2016.

2. Baysoy E, Yildirim DK, Ozsoy C, Campbell-Washburn AE, Faranesh AZ, Mutlu S, Lederman RJ and Kocaturk O, "Lithography based resonant marker design for MRI catheter visualization", 19th Annual Society for Cardiovascular Magnetic Resonance (SCMR) Scientific Sessions, Los Angeles, USA, Jan. 27-30, 2016.

3. Yildirim DK, Sonmez M, Lederman RJ, Kocaturk O, "A Novel Active Device Fabrication Method for Interventional MRI Procedures", International Conference on Medical and Biological Engineering 2017 (CMBEBIH), Sarajevo, Bosnia and Herzigova, 16-18th Mar. 2017. **(Oral Presentation)**

4. Basar B, Yildirim DK, Lederman RJ, Kocaturk O. "An MR-Safe Metal-Braided Catheter Design For Interventional CMR", The International Society for Magnetic Resonance in Medicine (ISMRM) 25th Annual Meeting & Exhibition, Honolulu, Hawaii, USA, 22-27 Apr 2017. **(Oral Presentation)**

5. Yildirim K, Mahcicek ID, Lederman RJ, Kocaturk O, "An Active Biopsy Needle Design for MRI Guided Prostate Biopsy", Joint Annual Meeting the International Society for Magnetic Resonance in Medicine (ISMRM) - European Society For Magnetic Resonance In Medicine And Biology (ESMRMB) Paris, France, 16-21 June 2018 **(Oral presentation)**

6. Mahcicek ID, Yildirim DK, Kocaturk O. "Phantom Study of Novel Biopsy Needle and Assisted Robotic System Designed for Prostate Biopsy Procedure under MRI", The International Society for Magnetic Resonance in Medicine (ISMRM) 27th Annual Meeting & Exhibition. Montreal, Canada, 2019.

7. Yildirim DK, Bruce CG, Ramasawmy R, O'Brien KJ, Campbell-Washburn AE, Herzka DA, Lederman RJ, and Kocaturk O. "A novel active guidewire design with a curved tip geometry for interventional MRI applications under 0.55T", The International Society for Magnetic Resonance in Medicine (ISMRM) 28th Annual Meeting & Exhibition. Sydney, Australia, 2020. **(Oral presentation)**

8. Özen A, Reiss S, Thomas L, Yildirim DK, Kocaturk O, Bock M. "MR Safety Assessments of Active Implantable and Interventional Devices in a Single Measurement Setup." The International Society for Magnetic Resonance in Medicine (ISMRM) 29th Annual Meeting & Exhibition, 2021. **(Oral presentation)**

9. Herzka DA, Bruce CG, Ramasawmy R, Yildirim DK, O'Brien KJ, Schenke WH, Rogers T, Campbell-Washburn AE, Lederman RJ, Kolandaivelu A. "Native Contrast Visualization of Myocardial Radiofrequency Ablation and Acetic Acid Chemoab-

lation Lesions at 0.55 T." The International Society for Magnetic Resonance in Medicine (ISMRM) 29th Annual Meeting & Exhibition, 2021. **(Oral presentation)**

8. APPENDIX B: Scientific awards and invited talks

Scientific Awards

- **Summa Cum Laude Merit Award** for the work entitled "A novel active guidewire design with a curved tip geometry for interventional MRI applications under 0.55T". The International Society for Magnetic Resonance in Medicine (ISMRM) 28th Annual Meeting & Exhibition. Sydney, Australia, 2020.
- **Second-best trainee abstract.** Interventional MR study group. The International Society for Magnetic Resonance in Medicine (ISMRM) 28th Annual Meeting & Exhibition. Sydney, Australia, 2020.

Invited talks

- **"Towards a Clinical Grade Active Gudiewire".** Society for Cardiovascular Magnetic Resonance (SCMR) Annual Meeting Scientific Sessions, 2021.

REFERENCES

1. Lederman, R. J., "Cardiovascular interventional magnetic resonance imaging," *Circulation*, Vol. 112, no. 19, pp. 3009–17, 2005.

2. Nageotte, S. J., R. J. Lederman, and K. Ratnayaka, "Mri catheterization: Ready for broad adoption," *Pediatr Cardiol*, Vol. 41, no. 3, pp. 503–513, 2020.

3. Ratnayaka, K., J. P. Kanter, A. Z. Faranesh, E. K. Grant, L. J. Olivieri, R. R. Cross, I. F. Cronin, K. S. Hamann, A. E. Campbell-Washburn, K. J. O'Brien, T. Rogers, M. S. Hansen, and R. J. Lederman, "Radiation-free cmr diagnostic heart catheterization in children," *J Cardiovasc Magn Reson*, Vol. 19, no. 1, p. 65, 2017.

4. Rogers, T., and R. J. Lederman, "Interventional cmr: Clinical applications and future directions," *Curr Cardiol Rep*, Vol. 17, no. 5, p. 31, 2015.

5. Downing, D. F., "Cardiac catheterization and contrast study of the heart and great vessels in congenital cardiovascular defects," *Med Clin North Am*, Vol. 36, no. 6, pp. 1673–82, 1952.

6. Himmelstein, A., and A. Cournand, "Cardiac catheterization in the study of congenital cardiovascular anomalies; an evaluation," *Am J Med*, Vol. 12, no. 3, pp. 349–56, 1952.

7. Barbato, E., M. Noc, A. Baumbach, D. Dudek, M. Bunc, E. Skalidis, A. Banning, J. Legutko, N. Witt, M. Pan, H. H. Tilsted, H. Nef, G. Tarantini, D. Kazakiewicz, R. Huculeci, S. Cook, A. Magdy, W. Desmet, G. Cayla, D. Vinereanu, M. Voskuil, O. Goktekin, P. Vardas, A. Timmis, and M. Haude, "Mapping interventional cardiology in europe: the european association of percutaneous cardiovascular interventions (eapci) atlas project," *Eur Heart J*, Vol. 41, no. 27, pp. 2579–2588, 2020.

8. Zablah, J. E., and G. J. Morgan, "Innovations in congenital interventional cardiology," *Pediatr Clin North Am*, Vol. 67, no. 5, pp. 973–993, 2020.

9. Nossaman, B. D., B. A. Scruggs, V. E. Nossaman, S. N. Murthy, and P. J. Kadowitz, "History of right heart catheterization: 100 years of experimentation and methodology development," *Cardiol Rev*, Vol. 18, no. 2, pp. 94–101, 2010.

10. Ma, Y., N. Gogin, P. Cathier, R. J. Housden, G. Gijsbers, M. Cooklin, M. O'Neill, J. Gill, C. A. Rinaldi, R. Razavi, and K. S. Rhode, "Real-time x-ray fluoroscopy-based catheter detection and tracking for cardiac electrophysiology interventions," *Med Phys*, Vol. 40, no. 7, p. 071902, 2013.

11. Wu, X., J. Housden, Y. Ma, B. Razavi, K. Rhode, and D. Rueckert, "Fast catheter segmentation from echocardiographic sequences based on segmentation from corresponding x-ray fluoroscopy for cardiac catheterization interventions," *IEEE Trans Med Imaging*, Vol. 34, no. 4, pp. 861–76, 2015.

12. *National Research Council (U.S.). Committee to Assess Health Risks from Exposure to Low Levels of Ionizing Radiation: Health risks from exposure to low levels of ionizing radiation: BEIR VII Phase 2 Washington, D.C.: National Academies Press;*, 2006.

13. Goldstein, J. A., S. Balter, M. Cowley, J. Hodgson, L. W. Klein, and I. Interventional Committee of the Society of Cardiovascular, "Occupational hazards of interventional cardiologists: prevalence of orthopedic health problems in contemporary practice," *Catheter Cardiovasc Interv*, Vol. 63, no. 4, pp. 407–11, 2004.

14. Agner, B. F., J. T. Kuhl, J. J. Linde, K. F. Kofoed, P. Akeson, B. V. Rasmussen, G. B. Jensen, and U. Dixen, "Assessment of left atrial volume and function in patients with permanent atrial fibrillation: comparison of cardiac magnetic resonance imaging, 320-slice multi-detector computed tomography, and transthoracic echocardiography," *Eur Heart J Cardiovasc Imaging*, Vol. 15, no. 5, pp. 532–40, 2014.

15. Kuhl, J. T., J. Lonborg, A. Fuchs, M. J. Andersen, N. Vejlstrup, H. Kelbaek, T. Engstrom, J. E. Moller, and K. F. Kofoed, "Assessment of left atrial volume and function: a comparative study between echocardiography, magnetic resonance imaging and multi slice computed tomography," *Int J Cardiovasc Imaging*, Vol. 28, no. 5, pp. 1061–71, 2012.

16. Daniel, W. G., R. Erbel, W. Kasper, C. A. Visser, R. Engberding, G. R. Sutherland, E. Grube, P. Hanrath, B. Maisch, K. Dennig, and et al., "Safety of transesophageal echocardiography. a multicenter survey of 10,419 examinations," *Circulation*, Vol. 83, no. 3, pp. 817–21, 1991.

17. Ben-Haim, S. A., D. Osadchy, I. Schuster, L. Gepstein, G. Hayam, and M. E. Josephson, "Nonfluoroscopic, in vivo navigation and mapping technology," *Nat Med*, Vol. 2, no. 12, pp. 1393–5, 1996.

18. Bertaglia, E., P. D. Bella, C. Tondo, A. Proclemer, N. Bottoni, R. De Ponti, M. Landolina, M. G. Bongiorni, L. Coro, G. Stabile, A. Dello Russo, R. Verlato, M. Mantica, and F. Zoppo, "Image integration increases efficacy of paroxysmal atrial fibrillation catheter ablation: results from the cartomerge italian registry," *Europace*, Vol. 11, no. 8, pp. 1004–10, 2009.

19. Della Bella, P., G. Fassini, M. Cireddu, S. Riva, C. Carbucicchio, F. Giraldi, G. Maccabelli, N. Trevisi, M. Moltrasio, M. Pepi, C. A. Galli, D. Andreini, G. Ballerini, and G. Pontone, "Image integration-guided catheter ablation of atrial fibrillation: a prospective randomized study," *J Cardiovasc Electrophysiol*, Vol. 20, no. 3, pp. 258–65, 2009.

20. Wittkampf, F. H., E. F. Wever, R. Derksen, A. A. Wilde, H. Ramanna, R. N. Hauer, and E. O. Robles de Medina, "Localisa: new technique for real-time 3-dimensional localization of regular intracardiac electrodes," *Circulation*, Vol. 99, no. 10, pp. 1312–7, 1999.

21. Reddy, V. Y., Z. J. Malchano, G. Holmvang, E. J. Schmidt, A. d'Avila, C. Houghtaling, R. C. Chan, and J. N. Ruskin, "Integration of cardiac magnetic resonance imaging with three-dimensional electroanatomic mapping to guide left ventricular catheter manipulation: feasibility in a porcine model of healed myocardial infarction," *J Am Coll Cardiol*, Vol. 44, no. 11, pp. 2202–13, 2004.

22. Harrison, J. L., H. K. Jensen, S. A. Peel, A. Chiribiri, A. K. Grondal, L. O. Bloch, S. F. Pedersen, J. F. Bentzon, C. Kolbitsch, R. Karim, S. E. Williams, N. W. Linton, K. S. Rhode, J. Gill, M. Cooklin, C. A. Rinaldi, M. Wright, W. Y. Kim, T. Schaeffter, R. S. Razavi, and M. D. O'Neill, "Cardiac magnetic resonance and electroanatomical mapping of acute and chronic atrial ablation injury: a histological validation study," *Eur Heart J*, Vol. 35, no. 22, pp. 1486–95, 2014.

23. Currie, S., N. Hoggard, I. J. Craven, M. Hadjivassiliou, and I. D. Wilkinson, "Understanding mri: basic mr physics for physicians," *Postgrad Med J*, Vol. 89, no. 1050, pp. 209–23, 2013.

24. Gomaa, M. A., M. S. Hammad, A. Abdelmoghny, A. M. Elsherif, and H. M. Tawfik, "Magnetic resonance imaging versus computed tomography and different imaging modalities in evaluation of sinonasal neoplasms diagnosed by histopathology," *Clinical Medicine Insights. Ear, Nose and Throat*, Vol. 6, pp. 9–15, 2013.

25. Ratnayaka, K., A. Z. Faranesh, M. A. Guttman, O. Kocaturk, C. E. Saikus, and R. J. Lederman, "Interventional cardiovascular magnetic resonance: still tantalizing," *J Cardiovasc Magn Reson*, Vol. 10, p. 62, 2008.

26. Geethanath, S., R. Reddy, A. S. Konar, S. Imam, R. Sundaresan, B. D. Ramesh, and R. Venkatesan, "Compressed sensing mri: a review," *Crit Rev Biomed Eng*, Vol. 41, no. 3, pp. 183–204, 2013.

27. Boll, D. T., E. M. Merkle, D. M. Seaman, R. C. Gilkeson, A. P. Larson, O. P. Simonetti, J. L. Duerk, and J. S. Lewin, "Comparison of ecg-gated rectilinear vs. real-time radial k-space sampling schemes in cine true-fisp cardiac mri," *J Cardiovasc Magn Reson*, Vol. 6, no. 4, pp. 793–802, 2004.

28. Nayak, K. S., B. A. Hargreaves, B. S. Hu, D. G. Nishimura, J. M. Pauly, and C. H. Meyer, "Spiral balanced steady-state free precession cardiac imaging," *Magnetic Resonance in Medicine*, Vol. 53, no. 6, pp. 1468–73, 2005.

29. Griswold, M. A., P. M. Jakob, R. M. Heidemann, M. Nittka, V. Jellus, J. Wang, B. Kiefer, and A. Haase, "Generalized autocalibrating partially parallel acquisitions (grappa)," *Magnetic Resonance in Medicine*, Vol. 47, no. 6, pp. 1202–10, 2002.

30. Pruessmann, K. P., M. Weiger, M. B. Scheidegger, and P. Boesiger, "Sense: sensitivity encoding for fast mri," *Magnetic Resonance in Medicine*, Vol. 42, no. 5, pp. 952–62, 1999.

31. Feng, X., M. Salerno, C. M. Kramer, and C. H. Meyer, "Non-cartesian balanced steady-state free precession pulse sequences for real-time cardiac mri," *Magnetic Resonance in Medicine*, Vol. 75, no. 4, pp. 1546–55, 2016.

32. Ozturk, C., M. Guttman, E. R. McVeigh, and R. J. Lederman, "Magnetic resonance imaging-guided vascular interventions," *Top Magn Reson Imaging*, Vol. 16, no. 5, pp. 369–81, 2005.

33. Uecker, M., S. Zhang, D. Voit, A. Karaus, K. D. Merboldt, and J. Frahm, "Real-time mri at a resolution of 20 ms," *NMR Biomed*, Vol. 23, no. 8, pp. 986–94, 2010.

34. Elgort, D. R., and J. L. Duerk, "A review of technical advances in interventional magnetic resonance imaging," *Acad Radiol*, Vol. 12, no. 9, pp. 1089–99, 2005.

35. Hilbert, S., P. Sommer, M. Gutberlet, T. Gaspar, B. Foldyna, C. Piorkowski, S. Weiss, T. Lloyd, B. Schnackenburg, S. Krueger, C. Fleiter, I. Paetsch, C. Jahnke, G. Hindricks, and M. Grothoff, "Real-time magnetic resonance-guided ablation of typical right atrial flutter using a combination of active catheter tracking and passive catheter visualization in man: initial results from a consecutive patient series," *Europace*, Vol. 18, no. 4, pp. 572–7, 2016.

36. Ratnayaka, K., A. Z. Faranesh, M. S. Hansen, A. M. Stine, M. Halabi, I. M. Barbash, W. H. Schenke, V. J. Wright, L. P. Grant, P. Kellman, O. Kocaturk, and R. J. Lederman, "Real-time mri-guided right heart catheterization in adults using passive catheters," *European Heart Journal*, Vol. 34, no. 5, pp. 380–389, 2013.

37. Saikus, C. E., K. Ratnayaka, I. M. Barbash, J. H. Colyer, O. Kocaturk, A. Z. Faranesh, and R. J. Lederman, "Mri-guided vascular access with an active visualization needle," *Journal of Magnetic Resonance Imaging*, Vol. 34, no. 5, pp. 1159–66, 2011.

38. Razavi, R., D. L. Hill, S. F. Keevil, M. E. Miquel, V. Muthurangu, S. Hegde, K. Rhode, M. Barnett, J. van Vaals, D. J. Hawkes, and E. Baker, "Cardiac catheterisation guided by mri in children and adults with congenital heart disease," *Lancet*, Vol. 362, no. 9399, pp. 1877–82, 2003.

39. Hofmann, L. V., R. P. Liddell, J. Eng, B. A. Wasserman, A. Arepally, D. S. Lee, and D. A. Bluemke, "Human peripheral arteries: feasibility of transvenous intravascular mr imaging of the arterial wall," *Radiology*, Vol. 235, no. 2, pp. 617–22, 2005.

40. Rogers, T., K. Ratnayaka, J. M. Khan, A. Stine, W. H. Schenke, L. P. Grant, J. R. Mazal, E. K. Grant, A. Campbell-Washburn, M. S. Hansen, R. Ramasawmy, D. A. Herzka, H. Xue, P. Kellman, A. Z. Faranesh, and R. J. Lederman, "Cmr fluoroscopy right heart catheterization for cardiac output and pulmonary vascular resistance: results in 102 patients," *J Cardiovasc Magn Reson*, Vol. 19, no. 1, p. 54, 2017.

41. Pushparajah, K., A. Tzifa, A. Bell, J. K. Wong, T. Hussain, I. Valverde, H. R. Bellsham-Revell, G. Greil, J. M. Simpson, T. Schaeffter, and R. Razavi, "Cardiovascular magnetic resonance catheterization derived pulmonary vascular resistance and medium-term outcomes in congenital heart disease," *J Cardiovasc Magn Reson*, Vol. 17, p. 28, 2015.

42. White, S. K., D. M. Sado, A. S. Flett, and J. C. Moon, "Characterising the myocardial interstitial space: the clinical relevance of non-invasive imaging," *Heart*, Vol. 98, no. 10, pp. 773–9, 2012.

43. Dickfeld, T., R. Kato, M. Zviman, S. Nazarian, J. Dong, H. Ashikaga, A. C. Lardo, R. D. Berger, H. Calkins, and H. Halperin, "Characterization of acute and subacute radiofrequency ablation lesions with nonenhanced magnetic resonance imaging," *Heart Rhythm*, Vol. 4, no. 2, pp. 208–14, 2007.

44. Chung, A. H., K. Hynynen, V. Colucci, K. Oshio, H. E. Cline, and F. A. Jolesz, "Optimization of spoiled gradient-echo phase imaging for in vivo localization of a focused ultrasound beam," *Magnetic Resonance in Medicine*, Vol. 36, no. 5, pp. 745–52, 1996.

45. McGann, C., N. Akoum, A. Patel, E. Kholmovski, P. Revelo, K. Damal, B. Wilson, J. Cates, A. Harrison, R. Ranjan, N. S. Burgon, T. Greene, D. Kim, E. V. R. DiBella, D. Parker, R. S. MacLeod, and N. F. Marrouche, "Atrial fibrillation ablation outcome is predicted by left atrial remodeling on mri," *Circulation. Arrhythmia and electrophysiology*, Vol. 7, no. 1, pp. 23–30, 2014.

46. Sommer, P., M. Grothoff, C. Eitel, T. Gaspar, C. Piorkowski, M. Gutberlet, and G. Hindricks, "Feasibility of real-time magnetic resonance imaging-guided electrophysiology studies in humans," *Europace*, Vol. 15, no. 1, pp. 101–8, 2013.

47. Rogers, T., S. Mahapatra, S. Kim, M. A. Eckhaus, W. H. Schenke, J. R. Mazal, A. Campbell-Washburn, M. Sonmez, A. Z. Faranesh, K. Ratnayaka, and R. J. Lederman, "Transcatheter myocardial needle chemoablation during real-time magnetic resonance imaging: A new approach to ablation therapy for rhythm disorders," *Circ Arrhythm Electrophysiol*, Vol. 9, no. 4, p. e003926, 2016.

48. Rogers, T., K. Ratnayaka, P. Karmarkar, A. E. Campbell-Washburn, W. H. Schenke, J. R. Mazal, O. Kocaturk, A. Z. Faranesh, and R. J. Lederman, "Real-time magnetic resonance imaging guidance improves the diagnostic yield of endomyocardial biopsy," *JACC Basic Transl Sci*, Vol. 1, no. 5, pp. 376–383, 2016.

49. Ratnayaka, K., C. E. Saikus, A. Z. Faranesh, J. A. Bell, I. M. Barbash, O. Kocaturk, C. A. Reyes, M. Sonmez, W. H. Schenke, V. J. Wright, M. S. Hansen, M. C. Slack, and R. J. Lederman, "Closed-chest transthoracic magnetic resonance imaging-guided ventricular septal defect closure in swine," *JACC Cardiovasc Interv*, Vol. 4, no. 12, pp. 1326–34, 2011.

50. Raval, A. N., J. D. Telep, M. A. Guttman, C. Ozturk, M. Jones, R. B. Thompson, V. J. Wright, W. H. Schenke, R. DeSilva, R. J. Aviles, V. K. Raman, M. C. Slack, and R. J. Lederman, "Real-time magnetic resonance imaging-guided stenting of aortic coarctation with commercially available catheter devices in swine," *Circulation*, Vol. 112, no. 5, pp. 699–706, 2005.

51. Raval, A. N., P. V. Karmarkar, M. A. Guttman, C. Ozturk, S. Sampath, R. DeSilva, R. J. Aviles, M. Xu, V. J. Wright, W. H. Schenke, O. Kocaturk, A. J. Dick, V. K. Raman, E. Atalar, E. R. McVeigh, and R. J. Lederman, "Real-time magnetic resonance imaging-guided endovascular recanalization of chronic total arterial occlusion in a swine model," *Circulation*, Vol. 113, no. 8, pp. 1101–7, 2006.

52. Yang, X., and E. Atalar, "Intravascular mr imaging-guided balloon angioplasty with an mr imaging guide wire: feasibility study in rabbits," *Radiology*, Vol. 217, no. 2, pp. 501–6, 2000.

53. McVeigh, E. R., M. A. Guttman, R. J. Lederman, M. Li, O. Kocaturk, T. Hunt, S. Kozlov, and K. A. Horvath, "Real-time interactive mri-guided cardiac surgery: Aortic valve replacement using a direct apical approach," *Magnetic Resonance in Medicine*, Vol. 56, no. 5, pp. 958–964, 2006.

54. Clogenson, H., and J. Dobbelsteen, "Catheters and guidewires for interventional mri: Are we there yet?," *Journal of Imaging and Interventional Radiology*, Vol. 2, p. 28, 2016.

55. Rubin, D. L., A. V. Ratner, and S. W. Young, "Magnetic susceptibility effects and their application in the development of new ferromagnetic catheters for magnetic resonance imaging," *Invest Radiol*, Vol. 25, no. 12, pp. 1325–32, 1990.

56. Penzkofer, T., N. Peykan, K. Schmidt, G. Krombach, and C. K. Kuhl, "How mri compatible is "mri compatible"? a systematic comparison of artifacts caused by biopsy needles at 3.0 and 1.5 t," *Cardiovasc Intervent Radiol*, Vol. 36, no. 6, pp. 1646–1657, 2013.

57. Atalar, E., "Radiofrequency safety for interventional mri procedures," *Acad Radiol*, Vol. 12, no. 9, pp. 1149–57, 2005.

58. Omary, R. A., O. Unal, D. S. Koscielski, R. Frayne, F. R. Korosec, C. A. Mistretta, C. M. Strother, and T. M. Grist, "Real-time mr imaging-guided passive catheter tracking with use of gadolinium-filled catheters," *Journal of Vascular and Interventional Radiology*, Vol. 11, no. 8, pp. 1079–1085, 2000.

59. Miquel, M. E., S. Hegde, V. Muthurangu, B. J. Corcoran, S. F. Keevil, D. L. Hill, and R. S. Razavi, "Visualization and tracking of an inflatable balloon catheter using ssfp in a flow phantom and in the heart and great vessels of patients," *Magnetic Resonance in Medicine*, Vol. 51, no. 5, pp. 988–95, 2004.

60. Unal, O., F. R. Korosec, R. Frayne, C. M. Strother, and C. A. Mistretta, "A rapid 2d time-resolved variable-rate k-space sampling mr technique for passive catheter tracking during endovascular procedures," *Magnetic Resonance in Medicine*, Vol. 40, no. 3, pp. 356–62, 1998.

61. Kozerke, S., S. Hegde, T. Schaeffter, R. Lamerichs, R. Razavi, and D. L. Hill, "Catheter tracking and visualization using f-19 nuclear magnetic resonance," *Magnetic Resonance in Medicine*, Vol. 52, no. 3, pp. 693–697, 2004.

62. Magnusson, P., E. Johansson, S. Mansson, J. S. Petersson, C. M. Chai, G. Hansson, O. Axelsson, and K. Golman, "Passive catheter tracking during interventional mri using hyperpolarized c-13," *Magnetic Resonance in Medicine*, Vol. 57, no. 6, pp. 1140–1147, 2007.

63. Unal, O., J. Li, W. Cheng, H. Yu, and C. M. Strother, "Mr-visible coatings for endovascular device visualization," *Journal of Magnetic Resonance Imaging*, Vol. 23, no. 5, pp. 763–9, 2006.

64. Edelman, R. R., P. Storey, E. Dunkle, W. Li, A. Carrillo, A. Vu, and T. J. Carroll, "Gadolinium-enhanced off-resonance contrast angiography," *Magnetic Resonance in Medicine*, Vol. 57, no. 3, pp. 475–84, 2007.

65. Saikus, C. E., and R. J. Lederman, "Interventional cardiovascular magnetic resonance imaging: a new opportunity for image-guided interventions," *JACC Cardiovasc Imaging*, Vol. 2, no. 11, pp. 1321–31, 2009.

66. Quick, H. H., H. Kuehl, G. Kaiser, S. Bosk, J. F. Debatin, and M. E. Ladd, "Inductively coupled stent antennas in mri," *Magnetic Resonance in Medicine*, Vol. 48, no. 5, pp. 781–90, 2002.

67. Celik, H., and E. Atalar, "Reverse polarized inductive coupling to transmit and receive radiofrequency coil arrays," *Magnetic Resonance in Medicine*, Vol. 67, no. 2, pp. 446–56, 2012.

68. Celik, H., A. Uluturk, T. Tali, and E. Atalar, "A catheter tracking method using reverse polarization for mr-guided interventions," *Magnetic Resonance in Medicine*, Vol. 58, no. 6, pp. 1224–1231, 2007.

69. Kocaturk, O., A. H. Kim, C. E. Saikus, M. A. Guttman, A. Z. Faranesh, C. Ozturk, and R. J. Lederman, "Active two-channel 0.035" guidewire for interventional cardiovascular mri," *Journal of Magnetic Resonance Imaging*, Vol. 30, no. 2, pp. 461–5, 2009.

70. Sonmez, M., C. E. Saikus, J. A. Bell, D. N. Franson, M. Halabi, A. Z. Faranesh, C. Ozturk, R. J. Lederman, and O. Kocaturk, "Mri active guidewire with an embedded temperature probe and providing a distinct tip signal to enhance clinical safety," *J Cardiovasc Magn Reson*, Vol. 14, p. 38, 2012.

71. Bock, M., S. Müller, S. Zuehlsdorff, P. Speier, C. Fink, P. Hallscheidt, R. Umathum, and W. Semmler, "Active catheter tracking using parallel mri and real-time image reconstruction," *Magnetic Resonance in Medicine*, Vol. 55, no. 6, pp. 1454–1459, 2006.

72. Wang, W., "Mr guided active catheter tracking," *Magnetic resonance imaging clinics of North America*, Vol. 23, no. 4, pp. 579–589, 2015.

73. Guttman, M. A., C. Ozturk, A. N. Raval, V. K. Raman, A. J. Dick, R. DeSilva, P. Karmarkar, R. J. Lederman, and E. R. McVeigh, "Interventional cardiovascular procedures guided by real-time mr imaging: an interactive interface using multiple slices, adaptive projection modes and live 3d renderings," *Journal of Magnetic Resonance Imaging*, Vol. 26, no. 6, pp. 1429–35, 2007.

74. Atalar, E., P. A. Bottomley, O. Ocali, L. C. L. Correia, M. D. Kelemen, J. A. C. Lima, and E. A. Zerhouni, "High resolution intravascular mri and mrs by using a catheter receiver coil," *Magnetic Resonance in Medicine*, Vol. 36, no. 4, pp. 596–605, 1996.

75. Ladd, M. E., P. Erhart, J. F. Debatin, E. Hofmann, P. Boesiger, G. K. von Schulthess, and G. C. McKinnon, "Guidewire antennas for mr fluoroscopy," *Magnetic Resonance in Medicine*, Vol. 37, no. 6, pp. 891–7, 1997.

76. Quick, H. H., M. E. Ladd, G. G. Zimmermann-Paul, P. Erhart, E. Hofmann, G. K. von Schulthess, and J. F. Debatin, "Single-loop coil concepts for intravascular magnetic resonance imaging," *Magnetic Resonance in Medicine*, Vol. 41, no. 4, pp. 751–8, 1999.

77. Bell, J. A., C. E. Saikus, K. Ratnayaka, V. Wu, M. Sonmez, A. Z. Faranesh, J. H. Colyer, R. J. Lederman, and O. Kocaturk, "A deflectable guiding catheter for real-time mri-guided interventions," *Journal of Magnetic Resonance Imaging*, Vol. 35, no. 4, pp. 908–15, 2012.

78. Anderson, K. J., G. Leung, A. J. Dick, and G. A. Wright, "Forward-looking intravascular orthogonal-solenoid coil for imaging and guidance in occlusive arterial disease," *Magnetic Resonance in Medicine*, Vol. 60, no. 2, pp. 489–95, 2008.

79. Ocali, O., and E. Atalar, "Intravascular magnetic resonance imaging using a loopless catheter antenna," *Magnetic Resonance in Medicine*, Vol. 37, no. 1, pp. 112–8, 1997.

80. Qiu, B., P. Karmarkar, C. Brushett, F. Gao, R. Kon, S. Kar, E. Atalar, and X. Yang, "Development of a 0.014-inch magnetic resonance imaging guidewire," *Magnetic Resonance in Medicine*, Vol. 53, no. 4, pp. 986–90, 2005.

81. Susil, R. C., C. J. Yeung, and E. Atalar, "Intravascular extended sensitivity (ives) mri antennas," *Magnetic Resonance in Medicine*, Vol. 50, no. 2, pp. 383–90, 2003.

82. Konings, M. K., L. W. Bartels, H. F. Smits, and C. J. Bakker, "Heating around intravascular guidewires by resonating rf waves," *Journal of Magnetic Resonance Imaging*, Vol. 12, no. 1, pp. 79–85, 2000.

83. Kocaturk, O., C. E. Saikus, M. A. Guttman, A. Z. Faranesh, K. Ratnayaka, C. Ozturk, E. R. McVeigh, and R. J. Lederman, "Whole shaft visibility and mechanical performance for active mr catheters using copper-nitinol braided polymer tubes," *J Cardiovasc Magn Reson*, Vol. 11, p. 29, 2009.

84. Goloshevsky, A. G., J. H. Walton, M. V. Shutov, J. S. de Ropp, S. D. Collins, and M. J. McCarthy, "Development of low field nuclear magnetic resonance microcoils," *Review of Scientific Instruments*, Vol. 76, no. 2, p. 024101, 2005.

85. K, W., S. S, and B. A, "Pre-tuned resonant marker for imri using aerosol deposition on polymer catheters," *Proc SPIE*, 2010.

86. M, D., F. S, D. M, R. G, S. B, and K. M, "Using the hot embossing technology for the realization of microtechnical structures in medical imaging.," *Biomed Tech*, Vol. Sl-1, pp. 599–602, 2012.

87. Ellersiek, D., H. Fassbender, P. Bruners, J. G. Pfeffer, T. Penzkofer, A. H. Mahnken, T. Schmitz-Rode, W. Mokwa, and U. Schnakenberg, "A monolithically fabricated flexible resonant circuit for catheter tracking in magnetic resonance imaging," *Sensors and Actuators B: Chemical*, Vol. 144, no. 2, pp. 432–436, 2010.

88. Malba, V., R. Maxwell, L. B. Evans, A. F. Bernhardt, M. Cosman, and K. Yan, "Laser-lathe lithography—a novel method for manufacturing nuclear magnetic resonance microcoils," *Biomedical Microdevices*, Vol. 5, no. 1, pp. 21–27, 2003.

89. Yildirim, K. D., E. Baysoy, Z. Sagiroglu, O. Kocatürk, and S. Mutlu, "A novel method for developing clinical grade active devices dedicated to interventional mri procedures," in *ISMRM 2016*.

90. Li, W. J., J. D. Mai, and C.-M. Ho, "Sensors and actuators on non-planar substrates," *Sensors and Actuators A: Physical*, Vol. 73, no. 1, pp. 80–88, 1999.

91. Sillerud, L. O., A. F. McDowell, N. L. Adolphi, R. E. Serda, D. P. Adams, M. J. Vasile, and T. M. Alam, "1h nmr detection of superparamagnetic nanoparticles at 1t using a microcoil and novel tuning circuit," *Journal of Magnetic Resonance*, Vol. 181, no. 2, pp. 181–190, 2006.

92. Ilott, A. J., S. Chandrashekar, A. Klockner, H. J. Chang, N. M. Trease, C. P. Grey, L. Greengard, and A. Jerschow, "Visualizing skin effects in conductors with mri: (7)li mri experiments and calculations," *J Magn Reson*, Vol. 245, pp. 143–9, 2014.

93. ASTM F2052-15, "Standard test method for measurement of magnetically induced displacement force on medical devices in the magnetic resonance environment, www.astm.org," West Conshohocken, PA, 2015.

94. ASTM F2213-17, "Standard test method for measurement of magnetically induced torque on medical devices in the magnetic resonance environment, www.astm.org," West Conshohocken, PA, 2017.

95. Levin, M. L., and M. A. Miller, "Maxwell a treatise on electricity and magnetism," *Uspekhi Fizicheskikh Nauk*, Vol. 135, no. 3, pp. 425–440, 1981.

96. Kanal, E., J. P. Borgstede, A. J. Barkovich, C. Bell, W. G. Bradley, S. Etheridge, J. P. Felmlee, J. W. Froelich, J. Hayden, E. M. Kaminski, J. Lester, J. W., E. A. Scoumis, L. A. Zaremba, M. D. Zinninger, and R. American College of, "American college of radiology white paper on mr safety: 2004 update and revisions," *AJR Am J Roentgenol*, Vol. 182, no. 5, pp. 1111–4, 2004.

97. Lenz, E., "Ueber die bestimmung der richtung der durch elektrodynamische vertheilung erregten galvanischen ströme," *Annalen der Physik*, Vol. 107, no. 31, pp. 483–494, 1834.

98. Ham, C. L., J. M. Engels, G. T. van de Wiel, and A. Machielsen, "Peripheral nerve stimulation during mri: effects of high gradient amplitudes and switching rates," *Journal of Magnetic Resonance Imaging*, Vol. 7, no. 5, pp. 933–7, 1997.

99. Bottomley, P. A., R. W. Redington, W. A. Edelstein, and J. F. Schenck, "Estimating radiofrequency power deposition in body nmr imaging," *Magnetic Resonance in Medicine*, Vol. 2, no. 4, pp. 336–49, 1985.

100. Wolf, S., D. Diehl, M. Gebhardt, J. Mallow, and O. Speck, "Sar simulations for high-field mri: how much detail, effort, and accuracy is needed?," *Magnetic Resonance in Medicine*, Vol. 69, no. 4, pp. 1157–68, 2013.

101. Athey, T. W., "Current fda guidance for mr patient exposure and considerations for the future," *Ann N Y Acad Sci*, Vol. 649, pp. 242–57, 1992.

102. Park, S. M., R. Kamondetdacha, and J. A. Nyenhuis, "Calculation of mri-induced heating of an implanted medical lead wire with an electric field transfer function," *Journal of Magnetic Resonance Imaging*, Vol. 26, no. 5, pp. 1278–85, 2007.

103. Yeung, C. J., R. C. Susil, and E. Atalar, "Rf safety of wires in interventional mri: using a safety index," *Magnetic Resonance in Medicine*, Vol. 47, no. 1, pp. 187–93, 2002.

104. Peterson, D. M., B. L. Beck, C. R. Duensing, and J. R. Fitzsimmons, "Common mode signal rejection methods for mri: Reduction of cable shield currents for high static magnetic field systems," *Concepts in Magnetic Resonance Part B-Magnetic Resonance Engineering*, Vol. 19b, no. 1, pp. 1–8, 2003.

105. Gruber, B., M. Froeling, T. Leiner, and D. W. J. Klomp, "Rf coils: A practical guide for nonphysicists," *Journal of Magnetic Resonance Imaging*, 2018.

106. Ladd, M. E., and H. H. Quick, "Reduction of resonant rf heating in intravascular catheters using coaxial chokes," *Magnetic Resonance in Medicine*, Vol. 43, no. 4, pp. 615–619, 2000.

107. Seeber, D. A., I. Jevtic, and A. Menon, "Floating shield current suppression trap," *Concepts in Magnetic Resonance Part B-Magnetic Resonance Engineering*, Vol. 21b, no. 1, pp. 26–31, 2004.

108. Alipour, A., E. S. Meyer, C. L. Dumoulin, R. D. Watkins, H. Elahi, W. Loew, J. Schweitzer, G. Olson, Y. Chen, S. Tao, M. Guttman, A. Kolandaivelu, H. R. Halperin, and E. J. Schmidt, "Mri conditional actively tracked metallic electrophysiology catheters and guidewires with miniature tethered radio-frequency traps: Theory, design, and validation," *IEEE Trans Biomed Eng*, Vol. 67, no. 6, pp. 1616–1627, 2020.

109. Wirtz, D., O. Lips, B. David, S. Krueger, and S. Weiss, "Diagnostic mr-electrophysiology catheter with highly reisistive wires for reduction of rf-heating," *Proceedings of International Society of Magnetic Resonance in Medicine (ISMRM) 15th Annual meeting in Berlin*, 2007.

110. Weiss, S., P. Vernickel, T. Schaeffter, V. Schulz, and B. Gleich, "Transmission line for improved rf safety of interventional devices," *Magnetic Resonance in Medicine*, Vol. 54, no. 1, pp. 182–9, 2005.

111. Basar, B., A. E. Campbell-Washburn, T. Rogers, M. Sonmez, A. Z. Faranesh, K. Ratnayaka, R. J. Lederman, and O. Kocaturk, "Stiffness-matched segmented metallic guidewire for interventional cardiovascular mri," *Journal of Cardiovascular Magnetic Resonance*, Vol. 17, no. 1, p. P414, 2015.

112. Fandrey, S., S. Weiss, and J. Muller, "Development of an active intravascular mr device with an optical transmission system," *IEEE Trans Med Imaging*, Vol. 27, no. 12, pp. 1723–7, 2008.

113. Wong, E. Y., Q. Zhang, J. L. Duerk, J. S. Lewin, and M. Wendt, "An optical system for wireless detuning of parallel resonant circuits," *Journal of Magnetic Resonance Imaging*, Vol. 12, no. 4, pp. 632–8, 2000.

114. Yaras, Y. S., D. K. Yildirim, D. A. Herzka, T. Rogers, A. E. Campbell-Washburn, R. J. Lederman, F. L. Degertekin, and O. Kocaturk, "Real-time device tracking under mri using an acousto-optic active marker," *Magnetic Resonance in Medicine*, 2020.

115. Ozen, A. C., B. Silemek, T. Lottner, E. Atalar, and M. Bock, "Mr safety watchdog for active catheters: Wireless impedance control with real-time feedback," *Magnetic Resonance in Medicine*, Vol. 84, no. 2, pp. 1048–1060, 2020.

116. Acikel, V., B. Silemek, and E. Atalar, "Wireless control of induced radiofrequency currents in active implantable medical devices during mri," *Magnetic Resonance in Medicine*, Vol. 83, no. 6, pp. 2370–2381, 2020.

117. Etezadi-Amoli, M., P. Stang, A. Kerr, J. Pauly, and G. Scott, "Controlling radiofrequency-induced currents in guidewires using parallel transmit," *Magnetic Resonance in Medicine*, Vol. 74, no. 6, pp. 1790–1802, 2015.

118. Eryaman, Y., B. Guerin, C. Akgun, J. L. Herraiz, A. Martin, A. Torrado-Carvajal, N. Malpica, J. A. Hernandez-Tamames, E. Schiavi, E. Adalsteinsson, and L. L. Wald, "Parallel transmit pulse design for patients with deep brain stimulation implants," *Magnetic Resonance in Medicine*, Vol. 73, no. 5, pp. 1896–903, 2015.

119. Gudino, N., M. Sonmez, Z. Yao, T. Baig, S. Nielles-Vallespin, A. Z. Faranesh, R. J. Lederman, M. Martens, R. S. Balaban, M. S. Hansen, and M. A. Griswold, "Parallel transmit excitation at 1.5 t based on the minimization of a driving function for device heating," *Medical Physics*, Vol. 42, no. 1, pp. 359–371, 2015.

120. Campbell-Washburn, A. E., T. Rogers, B. Basar, M. Sonmez, O. Kocaturk, R. J. Lederman, M. S. Hansen, and A. Z. Faranesh, "Positive contrast spiral imaging for visualization of commercial nitinol guidewires with reduced heating," *J Cardiovasc Magn Reson*, Vol. 17, p. 114, 2015.

121. Campbell-Washburn, A. E., R. Ramasawmy, M. C. Restivo, I. Bhattacharya, B. Basar, D. A. Herzka, M. S. Hansen, T. Rogers, W. P. Bandettini, D. R. McGuirt, C. Mancini, D. Grodzki, R. Schneider, W. Majeed, H. Bhat, H. Xue, J. Moss, A. A. Malayeri, E. C. Jones, A. P. Koretsky, P. Kellman, M. Y. Chen, R. J. Lederman, and R. S. Balaban, "Opportunities in interventional and diagnostic imaging by using high-performance low-field-strength mri," *Radiology*, Vol. 293, no. 2, pp. 384–393, 2019.

122. Bottomley, P. A., and W. A. Edelstein, "Power deposition in whole-body nmr imaging," *Med Phys*, Vol. 8, no. 4, pp. 510–2, 1981.

123. Yeung, C. J., and E. Atalar, "Rf transmit power limit for the barewire loopless catheter antenna," *Journal of Magnetic Resonance Imaging*, Vol. 12, no. 1, pp. 86–91, 2000.

124. El-Sharkawy, A. M. M., D. Qian, and P. A. Bottomley, "The performance of interventional loopless mri antennae at higher magnetic field strengths," *Medical Physics*, Vol. 35, no. 5, pp. 1995–2006, 2008.

125. ASTM F2182-19e2, "Standard test method for measurement of radio frequency induced heating on or near passive implants during magnetic resonance imaging, www.astm.org," West Conshohocken, PA, 2019.

126. ISO/TS 10974:2018, "Assessment of the safety of magnetic resonance imaging for patients with an active implantable medical device. https://www.iso.org/standard/59752.html," Geneva, Switzerland, 2018.

127. Yeung, C. J., P. Karmarkar, and E. R. McVeigh, "Minimizing rf heating of conducting wires in mri," *Magnetic Resonance in Medicine*, Vol. 58, no. 5, pp. 1028–34, 2007.

128. Yeung, C. J., R. C. Susil, and E. Atalar, "Rf heating due to conductive wires during mri depends on the phase distribution of the transmit field," *Magnetic Resonance in Medicine*, Vol. 48, no. 6, pp. 1096–8, 2002.

129. Lottner, T., S. Reiss, A. Bitzer, M. Bock, and A. C. Özen, "A transfer function measurement setup with an electro-optic sensor for mr safety assessment in cascaded media," *IEEE Transactions on Electromagnetic Compatibility*, pp. 1–11, 2020.

130. Zeng, Q., J. Liu, L. M. Angelone, T. Lloyd, S. Wedan, J. Chen, and W. Kainz, "Investigation of rf-induced heating near interventional catheters at 1.5 t mri: A combined modeling and experimental study," *IEEE Transactions on Electromagnetic Compatibility*, Vol. 61, no. 5, pp. 1423–1431, 2019.

131. Missoffe, A., and S. Aissani, "Experimental setup for transfer function measurement to assess rf heating of medical leads in mri: Validation in the case of a single wire," *Magnetic Resonance in Medicine*, Vol. 79, no. 3, pp. 1766–1772, 2018.

132. Gosselin, M. C., E. Neufeld, H. Moser, E. Huber, S. Farcito, L. Gerber, M. Jedensjo, I. Hilber, F. Di Gennaro, B. Lloyd, E. Cherubini, D. Szczerba, W. Kainz, and N. Kuster, "Development of a new generation of high-resolution anatomical models for medical device evaluation: the virtual population 3.0," *Physics in Medicine and Biology*, Vol. 59, no. 18, pp. 5287–5303, 2014.

133. Tokaya, J. P., A. J. E. Raaijmakers, P. R. Luijten, J. F. Bakker, and C. A. T. van den Berg, "Mri-based transfer function determination for the assessment of implant safety," *Magnetic Resonance in Medicine*, Vol. 78, no. 6, pp. 2449–2459, 2017.

134. Tokaya, J. P., A. J. E. Raaijmakers, P. R. Luijten, and C. A. T. van den Berg, "Mri-based, wireless determination of the transfer function of a linear implant: Introduction of the transfer matrix," *Magnetic Resonance in Medicine*, Vol. 80, no. 6, pp. 2771–2784, 2018.

135. Chen, X., and M. Steckner, "Electromagnetic computation and modeling in mri," *Med Phys*, Vol. 44, no. 3, pp. 1186–1203, 2017.

136. Kalafala, A. K., "A design approach for actively shielded magnetic resonance imaging magnets," *IEEE Transactions on Magnetics*, Vol. 26, no. 3, pp. 1181–1188, 1990.

137. Liu, W., X. Tang, and D. Zu, "A novel target-field approach to design bi-planar shim coils for permanent-magnet mri," *Concepts in Magnetic Resonance Part B: Magnetic Resonance Engineering*, Vol. 37B, no. 1, pp. 29–38, 2010.

138. Wang, H., A. Trakic, F. Liu, and S. Crozier, "Numerical field evaluation of health-care workers when bending towards high-field mri magnets," *Magnetic Resonance in Medicine*, Vol. 59, no. 2, pp. 410–422, 2008.

139. Shvartsman, S., M. Morich, G. Demeester, and Z. Zhai, "Ultrashort shielded gradient coil design with 3d geometry," *Concepts in Magnetic Resonance Part B: Magnetic Resonance Engineering*, Vol. 26B, no. 1, pp. 1–15, 2005.

140. Forbes, L. K., and S. Crozier, "On a possible mechanism for peripheral nerve stimulation during magnetic resonance imaging scans," *Phys Med Biol*, Vol. 46, no. 2, pp. 591–608, 2001.

141. Wang, C., and G. X. Shen, "B1 field, sar, and snr comparisons for birdcage, tem, and microstrip coils at 7t," *Journal of Magnetic Resonance Imaging*, Vol. 24, no. 2, pp. 439–443, 2006.

142. Guerin, B., M. Gebhardt, P. Serano, E. Adalsteinsson, M. Hamm, J. Pfeuffer, J. Nistler, and L. L. Wald, "Comparison of simulated parallel transmit body arrays at 3 t using excitation uniformity, global sar, local sar, and power efficiency metrics," *Magnetic Resonance in Medicine*, Vol. 73, no. 3, pp. 1137–50, 2015.

143. Bulumulla, S., L. Marinelli, and C. J. Hardy, "Mri-phased array evaluation using a human body model," *Concepts in Magnetic Resonance Part B: Magnetic Resonance Engineering*, Vol. 37B, no. 1, pp. 20–28, 2010.

144. Murbach, M., E. Neufeld, W. Kainz, K. P. Pruessmann, and N. Kuster, "Whole-body and local rf absorption in human models as a function of anatomy and position within 1.5t mr body coil," *Magnetic Resonance in Medicine*, Vol. 71, no. 2, pp. 839–845, 2014.

145. Food and Drug Administration (FDA), "Reporting of computational modeling studies in medical device submissions - guidance for industry and food and drug administration staff, www.fda.gov," Maryland, USA. 2016.

146. Polimeridis, A. G., J. F. Villena, L. Daniel, and J. K. White, "Stable fft-jvie solvers for fast analysis of highly inhomogeneous dielectric objects," *Journal of Computational Physics*, Vol. 269, pp. 280–296, 2014.

147. Villena, J. F., A. G. Polimeridis, Y. Eryaman, E. Adalsteinsson, L. L. Wald, J. K. White, and L. Daniel, "Fast electromagnetic analysis of mri transmit rf coils based on accelerated integral equation methods," *IEEE Transactions on Biomedical Engineering*, Vol. 63, no. 11, pp. 2250–2261, 2016.

148. Guerin, B., M. I. Iacono, M. Davids, D. Dougherty, L. M. Angelone, and L. L. Wald, "The 'virtual dbs population': five realistic computational models of deep brain stimulation patients for electromagnetic mr safety studies," *Phys Med Biol*, Vol. 64, no. 3, p. 035021, 2019.

149. Ibrahim, T. S., and L. Tang, "Insight into rf power requirements and b1 field homogeneity for human mri via rigorous fdtd approach," *Journal of Magnetic Resonance Imaging*, Vol. 25, no. 6, pp. 1235–1247, 2007.

150. Guérin, B., M. Gebhardt, P. Serano, E. Adalsteinsson, M. Hamm, J. Pfeuffer, J. Nistler, and L. L. Wald, "Comparison of simulated parallel transmit body arrays at 3 t using excitation uniformity, global sar, local sar, and power efficiency metrics," *Magnetic Resonance in Medicine*, Vol. 73, no. 3, pp. 1137–1150, 2015.

151. Nour, S. G., and J. S. Lewin, "Percutaneous biopsy from blinded to mr guided: an update on current techniques and applications," *Magn Reson Imaging Clin N Am*, Vol. 13, no. 3, pp. 441–64, 2005.

152. Diracoglu, D., K. Alptekin, F. Dikici, H. I. Balci, L. Ozcakar, and C. Aksoy, "Evaluation of needle positioning during blind intra-articular hip injections for osteoarthritis: fluoroscopy versus arthrography," *Arch Phys Med Rehabil*, Vol. 90, no. 12, pp. 2112–5, 2009.

153. Amedee, R. G., and N. R. Dhurandhar, "Fine-needle aspiration biopsy," *Laryngoscope*, Vol. 111, no. 9, pp. 1551–7, 2001.

154. Stein, H. L., and J. A. Evans, "Percutaneous transthoracic lung biopsy utilizing image amplification," *Radiology*, Vol. 87, no. 2, p. 350, 1966.

155. Lal, H., Z. Neyaz, A. Nath, and S. Borah, "Ct-guided percutaneous biopsy of intrathoracic lesions," *Korean J Radiol*, Vol. 13, no. 2, pp. 210–26, 2012.

156. Kim, J. W., and S. S. Shin, "Ultrasound-guided percutaneous core needle biopsy of abdominal viscera: Tips to ensure safe and effective biopsy," *Korean J Radiol*, Vol. 18, no. 2, pp. 309–322, 2017.

157. Bergero, M. A., P. F. Martinez, J. P. Radtke, and B. A. Hadaschik, "Multiparametric-mri-guided biopsy in the era of precision medicine," *Arch Esp Urol*, Vol. 70, no. 10, pp. 833–844, 2017.

158. DeAngelis, G. A., R. E. Moran, L. L. Fajardo, J. P. Mugler, J. M. Christopher, and J. A. Harvey, "Mri-guided needle localization: technique," *Semin Ultrasound CT MR*, Vol. 21, no. 5, pp. 337–50, 2000.

159. Meeuwis, C., N. H. Peters, W. P. Mali, A. M. Gallardo, R. van Hillegersberg, M. E. Schipper, and M. A. van den Bosch, "Targeting difficult accessible breast lesions: Mri-guided needle localization using a freehand technique in a 3.0 t closed bore magnet," *Eur J Radiol*, Vol. 62, no. 2, pp. 283–8, 2007.

160. Weiss, C. R., S. G. Nour, and J. S. Lewin, "Mr-guided biopsy: a review of current techniques and applications," *Journal of Magnetic Resonance Imaging*, Vol. 27, no. 2, pp. 311–25, 2008.

161. Campbell-Washburn, A. E., M. A. Tavallaei, M. Pop, E. K. Grant, H. Chubb, K. Rhode, and G. A. Wright, "Real-time mri guidance of cardiac interventions," *Journal of Magnetic Resonance Imaging*, Vol. 46, no. 4, pp. 935–950, 2017.

162. Guttman, M. A., R. J. Lederman, J. M. Sorger, and E. R. McVeigh, "Real-time volume rendered mri for interventional guidance," *J Cardiovasc Magn Reson*, Vol. 4, no. 4, pp. 431–42, 2002.

163. Settecase, F., A. J. Martin, P. Lillaney, A. Losey, and S. W. Hetts, "Magnetic resonance-guided passive catheter tracking for endovascular therapy," *Magn Reson Imaging Clin N Am*, Vol. 23, no. 4, pp. 591–605, 2015.

164. Miquel, M. E., S. Hegde, V. Muthurangu, B. J. Corcoran, S. F. Keevil, D. L. G. Hill, and R. S. Razavi, "Visualization and tracking of an inflatable balloon catheter using ssfp in a flow phantom and in the heart and great vessels of patients," *Magnetic Resonance in Medicine*, Vol. 51, no. 5, pp. 988–995, 2004.

165. Basar, B., M. Sonmez, D. K. Yildirim, R. Paul, D. A. Herzka, O. Kocaturk, R. J. Lederman, and A. E. Campbell-Washburn, "Susceptibility artifacts of metallic markers and cardiac catheterization devices on a high-performance 0.55t mri system," *Magn Reson Imaging*, 2020.

166. Frahm, C., H. B. Gehl, U. H. Melchert, and H. D. Weiss, "Visualization of magnetic resonance-compatible needles at 1.5 and 0.2 tesla," *Cardiovasc Intervent Radiol*, Vol. 19, no. 5, pp. 335–40, 1996.

167. Kuhn, J. P., S. Langner, K. Hegenscheid, M. Evert, A. Kickhefel, N. Hosten, and R. Puls, "Magnetic resonance-guided upper abdominal biopsies in a high-field wide-bore 3-t mri system: feasibility, handling, and needle artefacts," *Eur Radiol*, Vol. 20, no. 10, pp. 2414–21, 2010.

168. Stadler, A., W. Schima, A. Ba-Ssalamah, J. Kettenbach, and E. Eisenhuber, "Artifacts in body mr imaging: their appearance and how to eliminate them," *European Radiology*, Vol. 17, no. 5, pp. 1242–1255, 2007.

169. Baysoy, E., D. K. Yildirim, C. Ozsoy, S. Mutlu, and O. Kocaturk, "Thin film based semi-active resonant marker design for low profile interventional cardiovascular mri devices," *MAGMA*, Vol. 30, no. 1, pp. 93–101, 2017.

170. Quick, H. H., M. O. Zenge, H. Kuehl, G. Kaiser, S. Aker, S. Massing, S. Bosk, and M. E. Ladd, "Interventional magnetic resonance angiography with no strings attached: wireless active catheter visualization," *Magnetic Resonance in Medicine*, Vol. 53, no. 2, pp. 446–55, 2005.

171. Wang, W., "Magnetic resonance-guided active catheter tracking," *Magn Reson Imaging Clin N Am*, Vol. 23, no. 4, pp. 579–89, 2015.

172. Ladd, M. E., and J. F. Debatin, "Interventional and intravascular mr angiography," *Herz*, Vol. 25, no. 4, pp. 440–51, 2000.

173. Dumoulin, C. L., S. P. Souza, and R. D. Darrow, "Real-time position monitoring of invasive devices using magnetic resonance," *Magnetic Resonance in Medicine*, Vol. 29, no. 3, pp. 411–5, 1993.

174. Weiss, S., D. Wirtz, B. David, S. Krueger, O. Lips, D. Caulfield, S. F. Pedersen, J. Bostock, R. Razavi, and T. Schaeffter, "In vivo evaluation and proof of radiofrequency safety of a novel diagnostic mr-electrophysiology catheter," *Magnetic Resonance in Medicine*, Vol. 65, no. 3, pp. 770–7, 2011.

175. Yaras, Y. S., D. K. Yildirim, O. Kocaturk, and F. L. Degertekin, "Sensitivity and phase response of fbg based acousto-optic sensors for real-time mri applications," *OSA Contin*, Vol. 3, no. 3, pp. 447–458, 2020.

176. El-Sharkawy, A. M., D. Qian, and P. A. Bottomley, "The performance of interventional loopless mri antennae at higher magnetic field strengths," *Med Phys*, Vol. 35, no. 5, pp. 1995–2006, 2008.

177. Ahmad, M. M., R. R. A. Syms, I. R. Young, B. Mathew, W. Casperz, S. D. Taylor-Robinson, C. A. Wadsworth, and W. M. W. Gedroyc, "Catheter-based flexible microcoil rf detectors for internal magnetic resonance imaging," *Journal of Micromechanics and Microengineering*, Vol. 19, no. 7, 2009.

178. Moftakhar, P., P. Lillaney, A. D. Losey, D. L. Cooke, A. J. Martin, B. R. Thorne, R. L. Arenson, M. Saeed, M. W. Wilson, and S. W. Hetts, "New-generation laser-lithographed dual-axis magnetically assisted remote-controlled endovascular catheter for interventional mr imaging: In vitro multiplanar navigation at 1.5 t and 3 t versus x-ray fluoroscopy," *Radiology*, Vol. 277, no. 3, pp. 842–52, 2015.

179. Jordan, C. D., B. R. H. Thorne, A. Wadhwa, A. D. Losey, E. Ozhinsky, S. Kondapavulur, V. Fratello, T. Moore, C. Stillson, C. Yee, R. D. Watkins, G. C. Scott, A. J. Martin, X. Zhang, M. W. Wilson, and S. W. Hetts, "Wireless resonant circuits printed

using aerosol jet deposition for mri catheter tracking," *IEEE Transactions on Biomedical Engineering*, Vol. 67, no. 3, pp. 876–882, 2020.

180. Will, K., S. Schimpf, A. Brose, F. Fischbach, J. Ricke, B. Schmidt, and G. Rose, *Pre-tuned resonant marker for iMRI using aerosol deposition on polymer catheters*, Vol. 7625 of *SPIE Medical Imaging*, SPIE, 2010.

181. Detert, M., S. Friesecke, M. Deckert, G. Rose, B. Schmidt, and M. Kaiser, "Using the hot embossing technology for the realization of microtechnical structures in medical imaging," *Biomedical Engineering / Biomedizinische Technik*, Vol. 57, no. SI-1-Track-E, p. 599, 2012.

182. Li, W. J., J. D. Mai, and C. M. Ho, "Sensors and actuators on non-planar substrates," *Sensors and Actuators a-Physical*, Vol. 73, no. 1-2, pp. 80–88, 1999.

183. Sillerud, L. O., A. F. McDowell, N. L. Adolphi, R. E. Serda, D. P. Adams, M. J. Vasile, and T. M. Alam, "H-1 nmr detection of superparamagnetic nanoparticles at 1 t using a microcoil and novel tuning circuit," *Journal of Magnetic Resonance*, Vol. 181, no. 2, pp. 181–190, 2006.

184. Li, X., Z. T. Yu, D. Geraldo, S. Weng, N. Alve, W. Dun, A. Kini, K. Patel, R. Shu, F. Zhang, G. Li, Q. Jin, and J. Fu, "Desktop aligner for fabrication of multilayer microfluidic devices," *Rev Sci Instrum*, Vol. 86, no. 7, p. 075008, 2015.

185. "International organization for standardization (2015). iec 62366-1:2015 medical devices - part 1: Application of usability engineering to medical devices. geneva, switzerland,"

186. ISO 13485:2016, "International organization for standardization (2016). medical devices - quality management systems - requirements for regulatory purposes, https://www.iso.org/standard/59752.html," Geneva, Switzerland, 2016.

187. Tamaki, E., A. Hibara, H. B. Kim, M. Tokeshi, and T. Kitamori, "Pressure-driven flow control system for nanofluidic chemical process," *Journal of Chromatography A*, Vol. 1137, no. 2, pp. 256–262, 2006.

188. Lake, J. R., K. C. Heyde, and W. C. Ruder, "Low-cost feedback-controlled syringe pressure pumps for microfluidics applications," *Plos One*, Vol. 12, no. 4, 2017.

189. Hoult, D. I., and R. E. Richards, "The signal-to-noise ratio of the nuclear magnetic resonance experiment. 1976," *J Magn Reson*, Vol. 213, no. 2, pp. 329–43, 2011.

190. "Yildirim dk, mahcicek id, lederman rj, kocaturk o. an active biopsy needle design for mri guided prostate biopsy," *In Proceedings of the Joint Annual Meeting The International Society for Magnetic Resonance in Medicine (ISMRM) - European Society for Magnetic Resonance in Medicine And Biology (ESMRMB), Paris, France.*, 2018; 651.

191. "Standard handbook for electrical engineers, 8th edition," *Library Journal*, Vol. 73, no. 22, pp. 1824–1824, 1948.

192. "Astm f1874-98(2011), standard test method for bend testing of needles used in surgical sutures, astm international, west conshohocken, pa, 2011, www.astm.org,"

193. "Astm f2132-01(2008)e1, standard specification for puncture resistance of materials used in containers for discarded medical needles and other sharps, astm international, west conshohocken, pa, 2008, www.astm.org,"

194. Bieri, O., and K. Scheffler, "Fundamentals of balanced steady state free precession mri," *Journal of Magnetic Resonance Imaging*, Vol. 38, no. 1, pp. 2–11, 2013.

195. Yildirim, K. D., B. Basar, A. E. Campbell-Washburn, D. A. Herzka, O. Kocaturk, and R. J. Lederman, "A cardiovascular magnetic resonance (cmr) safe metal braided catheter design for interventional cmr at 1.5 t: freedom from radiofrequency induced heating and preserved mechanical performance," *J Cardiovasc Magn Reson*, Vol. 21, no. 1, p. 16, 2019.

196. Constantinides, C. D., E. Atalar, and E. R. McVeigh, "Signal-to-noise measurements in magnitude images from nmr phased arrays," *Magnetic Resonance in Medicine*, Vol. 38, no. 5, pp. 852–7, 1997.

197. Kaiser, M., M. Detert, M. A. Rube, A. El-Tahir, O. J. Elle, A. Melzer, B. Schmidt, and G. H. Rose, "Resonant marker design and fabrication techniques for device visualization during interventional magnetic resonance imaging," *Biomed Tech (Berl)*, Vol. 60, no. 2, pp. 89–103, 2015.

198. Duerig, T., A. Pelton, and D. Stöckel, "An overview of nitinol medical applications," *Materials Science and Engineering: A*, Vol. 273-275, pp. 149–160, 1999.

199. Borsboom, H. M., T. Claasen-Vujčić, H. J. G. Gaykema, and T. Mehlkopf, "Low-frequency quadrature mode birdcage resonator," *Magnetic Resonance Materials in Physics, Biology and Medicine*, Vol. 5, no. 1, pp. 33–37, 1997.

200. Giovannetti, G., V. Hartwig, L. Landini, and M. F. Santarelli, "Low-field mr coils: Comparison between strip and wire conductors," *Applied Magnetic Resonance*, Vol. 39, no. 4, pp. 391–399, 2010.

201. Kipling, M., A. Mohammed, and R. N. Medding, "Guidewires in clinical practice: applications and troubleshooting," *Expert Rev Med Devices*, Vol. 6, no. 2, pp. 187–95, 2009.

202. Kleinerman, R. A., "Cancer risks following diagnostic and therapeutic radiation exposure in children," *Pediatr Radiol*, Vol. 36 Suppl 2, pp. 121–5, 2006.

203. Kolandaivelu, A., C. G. Bruce, R. Ramasawmy, D. K. Yildirim, K. J. O'Brien, W. H. Schenke, T. Rogers, A. E. Campbell-Washburn, R. J. Lederman, and D. A. Herzka, "Native contrast visualization and tissue characterization of myocardial radiofrequency ablation and acetic acid chemoablation lesions at 0.55 t," *J Cardiovasc Magn Reson*, Vol. 23, no. 1, p. 50, 2021.

204. Yildirim, D. K., C. Bruce, D. Uzun, T. Rogers, K. O'Brien, R. Ramasawmy, A. Campbell-Washburn, D. A. Herzka, R. J. Lederman, and O. Kocaturk, "A 20-gauge active needle design with thin-film printed circuitry for interventional mri at 0.55t," *Magnetic Resonance in Medicine*, 2021.

205. Atalar, E., P. A. Bottomley, O. Ocali, L. C. Correia, M. D. Kelemen, J. A. Lima, and E. A. Zerhouni, "High resolution intravascular mri and mrs by using a catheter receiver coil," *Magnetic Resonance in Medicine*, Vol. 36, no. 4, pp. 596–605, 1996.

206. Knight, D. S., T. Kotecha, A. Martinez-Naharro, J. T. Brown, M. Bertelli, M. Fontana, V. Muthurangu, and J. G. Coghlan, "Cardiovascular magnetic resonance-guided right heart catheterization in a conventional cmr environment - predictors of procedure success and duration in pulmonary artery hypertension," *J Cardiovasc Magn Reson*, Vol. 21, no. 1, p. 57, 2019.

207. Erturk, M. A., A. M. M. El-Sharkawy, and P. A. Bottomley, "Interventional loopless antenna at 7 t," *Magnetic Resonance in Medicine*, Vol. 68, no. 3, pp. 980–988, 2012.

208. Serfaty, J. M., X. Yang, P. Aksit, H. H. Quick, M. Solaiyappan, and E. Atalar, "Toward mri-guided coronary catheterization: visualization of guiding catheters, guidewires, and anatomy in real time," *Journal of Magnetic Resonance Imaging*, Vol. 12, no. 4, pp. 590–4, 2000.

209. Qian, D., A. M. El-Sharkawy, E. Atalar, and P. A. Bottomley, "Interventional mri: tapering improves the distal sensitivity of the loopless antenna," *Magnetic Resonance in Medicine*, Vol. 63, no. 3, pp. 797–802, 2010.

210. Karmarkar, P. V., D. L. Kraitchman, I. Izbudak, L. V. Hofmann, L. C. Amado, D. Fritzges, R. Young, M. Pittenger, J. W. Bulte, and E. Atalar, "Mr-trackable intramyocardial injection catheter," *Magnetic Resonance in Medicine*, Vol. 51, no. 6, pp. 1163–72, 2004.

211. Etezadi-Amoli, M., P. Stang, A. Kerr, J. Pauly, and G. Scott, "Interventional device visualization with toroidal transceiver and optically coupled current sensor for radiofrequency safety monitoring," *Magnetic Resonance in Medicine*, Vol. 73, no. 3, pp. 1315–27, 2015.

212. Monies-Chass, I., A. Vilensky, B. Mordechowitz, and J. Birkhahn, "Hidden risk in operating room. micro-shock," *Acta Anaesthesiol Belg*, Vol. 37, no. 1, pp. 39–44, 1986.

213. Starmer, C. F., H. D. McIntosh, and R. E. Whalen, "Electrical hazards and cardiovascular function," *N Engl J Med*, Vol. 284, no. 4, pp. 181–6, 1971.

214. Yildirim, D., C. Bruce, R. Ramasawmy, K. O'Brien, A. Campbell-Washburn, D. Herzka, R. Lederman, and O. Kocaturk, "A novel active guidewire design with a curved tip geometry for interventional mri applications under 0.55t.," *The International Society for Magnetic Resonance in Medicine (ISMRM) Virtual Conference Exhibition*, 2020. p.109.

215. Robson, P. M., A. K. Grant, A. J. Madhuranthakam, R. Lattanzi, D. K. Sodickson, and C. A. McKenzie, "Comprehensive quantification of signal-to-noise ratio and g-factor for image-based and k-space-based parallel imaging reconstructions," *Magnetic Resonance in Medicine*, Vol. 60, no. 4, pp. 895–907, 2008.

216. Vazquez, R., and D. F. Larson, "Plasma protein denaturation with graded heat exposure," *Perfusion*, Vol. 28, no. 6, pp. 557–9, 2013.

217. Bakker, C. J., R. M. Hoogeveen, J. Weber, J. J. van Vaals, M. A. Viergever, and W. P. Mali, "Visualization of dedicated catheters using fast scanning techniques with potential for mr-guided vascular interventions," *Magnetic Resonance in Medicine*, Vol. 36, no. 6, pp. 816–20, 1996.

218. Zhang, S., A. A. Joseph, D. Voit, S. Schaetz, K. D. Merboldt, C. Unterberg-Buchwald, A. Hennemuth, J. Lotz, and J. Frahm, "Real-time magnetic resonance imaging of cardiac function and flow-recent progress," *Quant Imaging Med Surg*, Vol. 4, no. 5, pp. 313–29, 2014.

219. Rogers, T., K. Ratnayaka, and R. J. Lederman, "Mri catheterization in cardiopulmonary disease," *Chest*, Vol. 145, no. 1, pp. 30–36, 2014.

220. Grothoff, M., C. Piorkowski, C. Eitel, T. Gaspar, L. Lehmkuhl, C. Lucke, J. Hoffmann, L. Hildebrand, S. Wedan, T. Lloyd, D. Sunnarborg, B. Schnackenburg, G. Hindricks, P. Sommer, and M. Gutberlet, "Mr imaging-guided electrophysiological ablation studies in humans with passive catheter tracking: initial results," *Radiology*, Vol. 271, no. 3, pp. 695–702, 2014.

221. Ratnayaka, K., A. Z. Faranesh, M. S. Hansen, A. M. Stine, M. Halabi, I. M. Barbash, W. H. Schenke, V. J. Wright, L. P. Grant, P. Kellman, O. Kocaturk, and R. J. Lederman, "Real-time mri-guided right heart catheterization in adults using passive catheters," *Eur Heart J*, Vol. 34, no. 5, pp. 380–9, 2013.

222. Carey, J., A. Fahim, and M. Munro, "Design of braided composite cardiovascular catheters based on required axial, flexural, and torsional rigidities," *J Biomed Mater Res B Appl Biomater*, Vol. 70, no. 1, pp. 73–81, 2004.

223. Kalb, B., J. H. Indik, P. Ott, and D. R. Martin, "Mri of patients with implanted cardiac devices," *Journal of Magnetic Resonance Imaging*, 2017.

224. Armenean, C., E. Perrin, M. Armenean, O. Beuf, F. Pilleul, and H. Saint-Jalmes, "Rf-induced temperature elevation along metallic wires in clinical magnetic resonance imaging: influence of diameter and length," *Magnetic Resonance in Medicine*, Vol. 52, no. 5, pp. 1200–6, 2004.

225. Pictet, J., R. Meuli, S. Wicky, and J. J. van der Klink, "Radiofrequency heating effects around resonant lengths of wire in mri," *Phys Med Biol*, Vol. 47, no. 16, pp. 2973–85, 2002.

226. Basar, B., T. Rogers, K. Ratnayaka, A. E. Campbell-Washburn, J. R. Mazal, W. H. Schenke, M. Sonmez, A. Z. Faranesh, R. J. Lederman, and O. Kocaturk, "Segmented nitinol guidewires with stiffness-matched connectors for cardiovascular magnetic resonance catheterization: preserved mechanical performance and freedom from heating," *J Cardiovasc Magn Reson*, Vol. 17, p. 105, 2015.

227. Alpyildiz, T., "3d geometrical modelling of tubular braids," *Textile Research Journal*, Vol. 82, no. 5, pp. 443–453, 2012.

228. Scheffler, K., and S. Lehnhardt, "Principles and applications of balanced ssfp techniques," *Eur Radiol*, Vol. 13, no. 11, pp. 2409–18, 2003.

229. Siegemund, G., W. Schwertfeger, A. Feiring, B. Smart, F. Behr, H. Vogel, B. McKusick, and P. Kirsch, *Fluorine Compounds, Organic*, book section 3. Wiley-VCH Verlag GmbH Co. KGaA, 2000.

230. Wacker, F. K., C. M. Hillenbrand, J. L. Duerk, and J. S. Lewin, "Mr-guided endovascular interventions: device visualization, tracking, navigation, clinical applications, and safety aspects," *Magn Reson Imaging Clin N Am*, Vol. 13, no. 3, pp. 431–9, 2005.

231. Koch, K. M., B. A. Hargreaves, K. B. Pauly, W. Chen, G. E. Gold, and K. F. King, "Magnetic resonance imaging near metal implants," *Journal of Magnetic Resonance Imaging*, Vol. 32, no. 4, pp. 773–87, 2010.

232. Dyet, J. F., W. G. Watts, D. F. Ettles, and A. A. Nicholson, "Mechanical properties of metallic stents: how do these properties influence the choice of stent for specific lesions?," *Cardiovasc Intervent Radiol*, Vol. 23, no. 1, pp. 47–54, 2000.